INTRASEASONAL VARIABILITY IN NORTHERN GULF OF MEXICO HYPOXIA: IMPACTS OF BAROCLINIC INSTABILITY, ROUGH TOPOGRAPHY, AND EXPOSURE DURATION

A Dissertation

by

VERONICA ISABEL RUIZ XOMCHUK

Submitted to the Office of Graduate and Professional Studies of
Texas A&M University
in partial fulfillment of the requirements for the degree of

DOCTOR OF PHILOSOPHY

Chair of Committee,	Robert Hetland
Committee Members,	Steven DiMarco
	Piers Chapman
	James Kaihatu
Head of Department,	Shari Yvon-Lewis

August 2020

Major Subject: Oceanography

ABSTRACT

While the occurrence of seasonal bottom hypoxia in the Northern Gulf of Mexico is an extensively studied subject, most research effort has been put on understanding and quantifying hypoxic extent, and little is known about internal variability and short-term shifts. The general objective of this work is to gain a better understanding of the different scales of temporal and spatial variability found in the bottom hypoxia that develops every summer over the Texas-Louisiana shelf. Abun-dant submesoscale fronts over the shelf shape the main variability in oceanographic patterns at the surface, but evidence suggests they also interact with the bottom boundary layer. After setting up the problem, the first analytic part of this study show that hypoxia development in the far-field of the Mississippi plume is subject to physical processes with spatial scales ranging from $\mathcal{O}$(10km) to $\mathcal{O}$(100km), and temporal scales from the near-inertial period to seasonality. It is shown that variability in oxygen advection increases with decreasing temporal and spatial scales, consistently with a field rich in instabilities introducing small-scale, strong anomalies in the shelf. Through a Reynolds decomposition of the budget, we separate anomalies from the main flow and identify the vertical turbulent flux $\langle w'o' \rangle_T$ as the primary counterbalance to sediment oxygen demand during periods when the hypoxic extent is maintained or destroyed. Next, the spatial structure of hypoxia is explored analyzing time of exposure and variability utilizing 24 years of simulations. Several generalizations are made about of the distribution of hypoxia over the far field of the shelf, and its relationship to the intrusion low oxygen water form the bottom into the interior. Finally, a set of idealized simulations is used to further prove the modulation effect of instabilities in the oxygena-tion of bottom waters, linking apparent oxygen utilization to intrusions and ventilation induced by the instabilities.

DEDICATION

To those who have loved me at all times.

ACKNOWLEDGMENTS

I would like to acknowledge Professor Robert Hetland for his invaluable guidance in research but also in several matters of thought, for pushing me the hard way to escape the "Brain Crack". I would like to thank the members of my committee, Professors Steven DiMarco, Piers Chapman and James Kaihatu, for being supportive to my work and career and for many valuable suggestions. I would like to thank my colleagues, Dr. Lixin Qu, Dr. Kristen Thyng and Dr. Daijiro Kobashi for their help and support, and many productive discussions and feedback. I would like to also acknowledge all my professors at Texas A&M for their dedication to teaching. It wouldn't be fair if I also didn't acknowledge those who gave emotional support when times were hard. Without them, whose names I carry close to my heart, this wouldn't have been possible.

Chapter 2 is based on an article submitted to the Journal of Geophysical Research - Oceans, co-authored by Professor Robert Hetland.

Chapter 3 is based on a manuscript in preparation, co-authored by Professor Robert Hetland.

CONTRIBUTORS AND FUNDING SOURCES

Contributors

This work was supported by a dissertation committee consisting of Professors Robert Hetland (advisor), Steven DiMarco and Piers Chapman of the Department of Oceanography, and Professor James Kaihatu of the Department of Civil Engineering.

The realistic model used in Chapters 2 and 3 was developed in the Physical Oceanography Numerical Group, lead by Professor Robert Hetland, and is currently maitained by Dr. DJ. Kobashi. The hydrographic data used in Chapter 2 was provided by Professor Steven DiMarco. The numerical simulation framework used in Chapter 4 is based on previous work developed by Professor Robert Hetland.

All other work conducted for the dissertation was completed by the student independently.

Funding Sources

Graduate study was supported in part by a grant from the Gulf of Mexico Research Initiative, and in part by NOAA through the Coastal Ocean Modeling Testbed (COMT) project, as well as several scholarships/fellowships from the Department of Oceanography at Texas A&M.

NOMENCLATURE

α	Bottom Slope
M^2	Horizontal Buoyancy Gradient
N^2	Vertical Buoyancy Gradient
f	Coriolis Parameter / Inertial Frequency
ADCP	Acoustic Doppler Current Profiler
AOU	Apparent Oxygen Utilization
BBL	Bottom boundary layer
COAWST	Coupled-Ocean-Atmosphere-Wave-Sediment Transport
CTD	Conductivity-Temperature-Depth
DO	Dissolved Oxygen
EKE	Eddy kinetic energy
GCM	General Circulation Model
HYCOM	Hybrid Coordinate Ocean Model
LUMCON	Louisiana Universities Marine Consortium
MCH	Mechanisms Controlling Hypoxia
MKE	Mean kinetic energy
NDBC	National Data Buoy Center
NGOM	Northern Gulf of Mexico
$\mathcal{O}()$	Order of magnitude
PDS	Power Density Spectra
ROMS	Regional Ocean Modeling System
SEAMAP	Southeast Area Monitoring and Assessment Program

STD	Standard Deviation
TABS	Texas Automated Buoy System
TOMS	Terrain-following Ocean Modeling System
TX-LA	Texas-Louisiana
TXLA	ROMS implementation for Texas-Louisiana
UCLA-ROMS	Version of ROMS developed at the University of California, Los Angeles

TABLE OF CONTENTS

Page

LIST OF FIGURES

FIGURE Page

LIST OF TABLES

TABLE Page

1. INTRODUCTION

1.1 Background and motivation

Coastal hypoxia is a well known process that develops where oxygen consumption exceeds the supply to the bottom water layer. In the water column, oxygen is consumed through respiration and oxidation, and it is injected through physical processes like advection and diffusion from the adjacent water layers, the atmosphere, or by local production from photosynthesis. The imbalance causing oxygen depletion can be of natural or anthropogenic origin, and the driving mechanisms are a combination of physical and biochemical processes.

Some technical conventions have been established to address oxygen depletion in the water column. Environments with DO concentration levels good enough to support local biological community respiration are considered to be normoxic. Reduced DO levels with consequent impacts on the biota are regarded as hypoxia. Environments where oxygen has been totally consumed are experiencing anoxia. A typical threshold level used in literature to define hypoxic waters is 2 mg L^{-1} or 62.5 μM (Rabalais and Turner, 2001) However, this value is taken from the fishery collapse estimates reported by Renaud (1986), and is used for practical reasons mainly as a tool to quantify the extension of the hypoxic influence. In reality, studies on the effects of hypoxia on biodiversity point towards a more complex vulnerability response, recommending the use of stress gradients instead of fixed thresholds (Villnäs et al., 2012).

In the Northern Gulf of Mexico (NGOM), localized hypoxia has been observed and studied since the early 1970's (e.g. May, 1973; Harper et al., 1981). Nowadays, the NGOM is one of the largest regions experiencing increasing hypoxic episodes in temporal and spatial scales worldwide (Diaz and Rosenberg, 2008; Zhang et al., 2010; Hofmann et al., 2011). In this region, the occurrence of hypoxia is seasonal (Rabalais et al., 2001b; Bianchi et al., 2010b), usually lasting from late spring through summer; and whereas some of the triggers are of natural origin, anthropogenic eutrophication exacerbates the condition, expanding temporal and spatial scales. The process ini-

tiates with the late spring increase in the water column stratification and the nutrient load over the shelf, both consequences of the seasonal intensification of the Mississippi-Atchafalaya River system discharge (Quiñones Rivera et al., 2007; Bianchi et al., 2010b; Obenour et al., 2013, 2015; Yu et al., 2015b). Stratification inhibits mixing, and thus the oxygen supply to the bottom, while eutrophication heightens respiration, and hence the oxygen sink. The anthropogenically magnified nutrient load exacerbates the condition, expanding temporal and spatial scales. An additional factor to consider, which has been suggested to contribute in the spread of hypoxic regions on a global scale, is the global warming trend, as it intensifies temperature induced stratification, decreases oxygen solubility in water, and enhances metabolic rates (Steckbauer et al., 2011; Meire et al., 2013).

Because hypoxia is a bottom process, observation is often difficult. Friedrich et al. (2014) give a thorough summary of methodologies used to observe hypoxia, ranging from micro- (O_2 micro profilers) to large-scale studies (cruise tracks). Given that dynamic processes in the coastal ocean range from micro- to meso- scales, the study of hypoxia should include different approaches. To monitor DO concentrations, stationary platforms may yield measurements with hourly or lower frequency for extended periods of time, but are usually limited to a couple of stations giving point observations. Conversely, non-stationary instruments (gliders, towed equipment, CTD casts) provide different kinds of time/space composites that allow observing length scales of $\mathcal{O}(10^2$ m) to $\mathcal{O}(10^6$ m) , but lose a true temporal scale while moving.

NGOM's hypoxia is a process occurring annually over a time scale of several months, covering a spatial domain of thousands of km, and mostly within a few meters of the bottom. Given the wide variability in scales, all observational strategies can supply only partial information to understand the inherent processes. Moreover, current efforts in understanding hypoxia are mainly centered on establishing a relationship between the aerial extent and the effects of nutrient load and stratification. This approach is fueled by the region's main monitoring effort (a summer cruise), that has attempted to map the midsummer extent for more than 20 years. The obtained estimates are simultaneously based on the assumption, and promote the paradigm, of a slow moving, almost stagnant

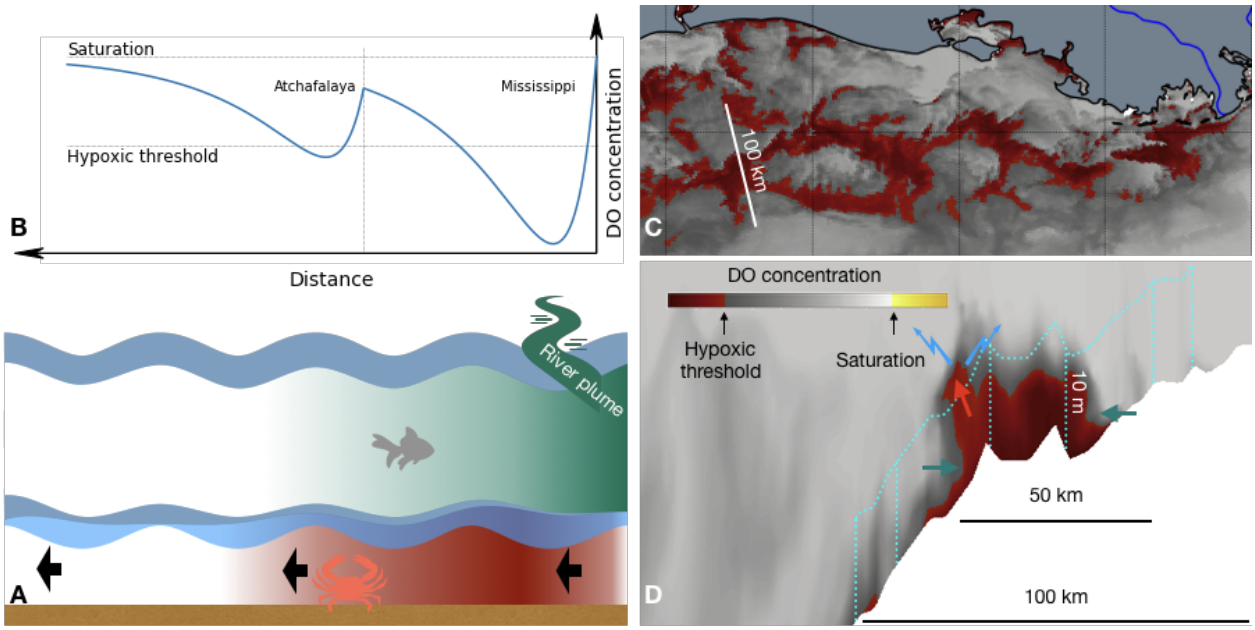

Figure 1.1: Common paradigm of a slow moving hypoxic bottom (left), with controlling mechanisms changing from east (nutrients) to west (stratification) vs the proposed dynamic view (right) driven by submesoscale convergence-divergence processes. A) A simplified cartoon of the mechanisms controlling hypoxia. B) DO model proposed by Scavia et al. (2013), with a modified Streeter-Phelps equation which divides the nutrient load between the Mississippi and Atchafalaya plumes. C) Complex features in the bottom DO simulated by the TXLA model with a scale indication. D) Schematic of a simulated cross-shore section, indicating a convergence process inducing low DO intrusions in to the mid-water column, and also influences vertical diffusivity. The dotted lines represent control volumes used in Chapter 2 to determine changes in the DO budget balance.

BBL propagating westwards (Fig.1.1, A and B). In contrast, knowledge on the inner dynamics of the hypoxic region is scarce, while past (see references in Bianchi et al., 2010b) and recent (DiMarco and Zimmerle, 2017) evidence suggests that the BBL has a complex morphology and is very dynamic. A concept of these distinct frameworks can be seen in Fig.1.1, and this small-scale variability, developing and moving in the larger scale hypoxic extent, will be referred herein as patchiness.

A patchy hypoxic region, moving and changing faster than commonly addressed, presents a need to consider this variability while evaluating the induced ecological stress. Strong temporal variations of DO concentrations have a direct effect in the behavior and abundance of living organisms of all types. For instance, different functional groups of organisms in the water column,

e.g. species and life stages, develop distinct horizontal and vertical avoidance strategies (Bell and Eggleston, 2005). In the NGOM, Zhang et al. (2009) studied changes in the behavior and distribution of pelagic fish and mesozooplankton around hypoxic patches. They found different patterns of avoidance and spatial overlap between types of biomass around hypoxic enclosures. Similarly, Hazen et al. (2009) found that bottom hypoxia induced vertical and horizontal displacement of fish biomass on the Louisiana shelf. On the other hand, benthic organisms (especially sessile, and burrowing) have to develop resistance strategies. Consequently, extended periods of exposure to low DO (weeks to months), induce different stress levels than fluctuating conditions, from a normoxia to hypoxia, subject to some oscillatory frequency of hours or days (e.g. Villnäs et al., 2012). Furthermore, the periodicity of exposure to hypoxia is known to affect recovery timescales (Steckbauer et al., 2011). These findings point to the importance of capturing variability realistically in the development of hypoxia in the NGOM.

1.1.1 Bottom oxygen structure in the Texas-Louisiana shelf

The bottom hypoxic area covering the TX-LA shelf has been estimated to span from 5 to 22 thousand km^2 during the last couple of decades, although restricted to depths between approximately 5 and 60 m (Rabalais et al., 2007; Turner et al., 2008). On the vertical dimension, the hypoxic layer thickness above the bottom rarely exceeds 10 m (Rabalais et al., 2007; Hazen et al., 2009). These regional-scale estimations have been made from annual cruise mapping efforts, undertaken every summer since 1985, following a standart grid of stations over a time-span of about a week. The estimation of bottom water hypoxia is made through interpolation of measurements between sampling locations along transects separated by about 50 km. Thus, the observation of the features of the surveyed area is limited to the resolution of the sampling distribution, and is independent of the real features of the movements and extension of the hypoxic water mass. Furthermore, the instruments used during the cruise campaign cannot be lowered to the very bottom of the shelf, so the deepest measurement is made some meters above the sediment.

In contrast, continuous records of near bottom DO concentration at stations close the Mississippi Delta, reveal a fast moving system (e.g. Rabalais and Turner, 2006; Bianchi et al., 2010b).

Rabalais et al. (1994) reported finding strong diurnal oscillations of near bottom DO at two stations located close to the Delta. One of the stations reached hypoxia 50% of the time, while the other (only 77 km apart) remained anoxic most of the time. A correlation found with a local tidal gauge record made the authors hypothesize that these oscillations might be caused by tidal advection. However, later investigations on the TX-LA shelf dynamics point to the existence of wind-induced near-inertial oscillations of the same frequency (Chen et al., 1996; Chen and Xie, 1997), which intensify during summer months (DiMarco et al., 2000), and could be responsible for the variability observed in the oxygen record. In other regions, high temporal variability in DO is known to be indicative of complex three-dimensional structures formed by complex hydrodynamic processes including baroclinic and barotropic inflows, internal waves, upwelling, and boundary mixing (Reissmann et al., 2009).

In an early study, Wiseman et al. (1997) suggested that while the strong near surface pycnocline is a necessary condition for the development of hypoxia over the Louisiana shelf, the weaker near-bottom pycnocline determines the morphology. Later, DiMarco et al. (2010) reported observations of packets of low oxygen concentrations under halocline intrusions from meanders of the Mississippi river plume, while sampling a transect following the 20 m isobath. The horizontal length scale of those pockets (50 km) was found to be the same as that of the local bathymetry. Subsequently, high-resolution observations following cross-shore transects along the TX-LA shelf revealed some complex structure in the bottom hypoxia (DiMarco and Zimmerle, 2017), but no further efforts have been made to investigate the inner length scales on the shelf far from the Delta. Recent modeling studies suggest to bottom convergence as responsible for low oxygen mid water intrusions observed by DiMarco and Zimmerle (2017); Zhang et al. (2015); Zhang and Hetland (2018). When considering the observed and simulated complexity, the shipboard annual estimates of hypoxic extent in the TX-LA are most likely inaccurate, and overly simplistic. Moreover, near-inertial periods and weather-band timescales are completely lost.

Regarding temporal scales, models suggest that the initial transition from normoxic to hypoxic conditions can last about 3 weeks, while episodic events (cold fronts and tropical storms) can

partially break well established hypoxic areas in days (Justić and Wang, 2014). After oxygenation events, permanent hypoxic conditions can be re-established within 1 to 2 weeks (Rabalais et al., 2007; DiMarco et al., 2010; Justić and Wang, 2014). Additionally, modeled hypoxic extent has been shown to correlate with the duration of upwelling-favorable winds (Feng et al., 2012, 2014), which appearance and span vary from year to year in the NGOM on scales of 1 to 2 months.

Several attempts have been made to explain inter-annual variability in hipoxic extent using simple models, but leveraging on the slow moving BBL paradigm. Using a physical-biological two-box model, Justić et al. (1996) predicted a decrease in summertime bottom oxygen content, as a response to atmospheric CO_2 increase, linking it to changes in precipitation, as larger hypoxic regions form during flood years. To understand the effects of nitrogen load reduction on the NGOM hypoxic area, Scavia et al. (2003) fitted a water quality model to a time series of extent estimates (1985-2002), and reported to account for 88% of the variability found in the data-set. However, the model assumed a correspondence between the measured extent of midsummer hypoxia and that which would be achieved at a steady state. Later, the estimated mapped extents where contended, as major trends were found to be artifacts of sampling design and interpolation limitations (Obenour et al., 2013), implying that the variability explained by all previous models was also an effect of those artifacts. Scavia et al. (2013) re-calibrated the model to the revised area estimates, and adapted it to use weather categories to modify decay and re-aeration rates as well as the bottom "downstream velocity". This new implementation was reported to account for 69% of the variability in the estimates. However, given previous evidence, all these estimates are overly simplistic, and do not consider the complex hydrodynamics of the region. Endorsing this point, Kemp et al. (2009) analyzed over 24 hypoxic systems in the world, seeking to identify different recovery responses to nutrient load reduction remediation efforts. They found that half of the systems displayed a direct linear response, but the rest responded with non-linear complex regimes. The latter was true, especially where climatic influences were found to be strong, which was the case for the NGOM. This supports the idea that to understand the long-term evolution of seasonal hypoxia in the NGOM, including the consequences of global warming, it is relevant to understand

the non-linear submesoscale drivers.

To reproduce hydrodynamic variability realistically in the TX-LA hypoxic region, models need to resolve sub-mesoscale (100 m to 10 km) and mesoscale (10 to 100 km) processes, which are abundant on the shelf due to the baroclinic instabilities generated by the Mississippi-Atchafalaya freshwater plume. Wang and Justić (2009) provide an example of the impact of spatial scales on the simulations of hydrodynamic features. Their high-resolution, finite-volume model for the Louisiana shelf is able to represent the seasonal cycle of stratification accurately; however, the simulated cross-shore current velocities correlate poorly to ADCP observations. They attributed the poor correlation to unresolved mesoscale eddies, which were not provided in the boundary. Nonetheless, due to the fine resolution used, the model is able to reproduce realistic submesoscale features. Similar features were also observed in the bottom DO simulations.

Yet, due to the lack of comparable observations, models are often evaluated by their ability to reproduce hypoxic extent and not variability. In a study comparing three different circulation models, Fennel et al. (2016) attempted to identify the main physical aspects impacting hypoxic extent simulations. The models differed in their numerical schemes, resolution, forcing and initial conditions. It was demonstrated that the ability of the model to resolve bottom water temperature strongly impacts the simulated extent. This effect occurs because sediment respiration increases with increasing temperature, due to metabolic acceleration. In their comparison, lower resolution models simulated smaller hypoxic extent and volume, but no attempt was made to investigate the internal structure.

1.1.2 Oxygen representation in models

Since models can be used to investigate different scales of variability in hypoxia, it is also important to address how to simulate oxygen dynamics. Several efforts have been made to model DO. Proposed models can be of different nature and range from simple regression models based on observations (e.g. Justić et al., 1996; Scavia et al., 2003, 2013), to more complex models of biogeochemical processes in idealized physical settings (e.g. Soetaert and Middelburg, 2009), to complex hydrodynamic models using simplified parameterizations of the biogeochemical processes, to fully

coupled hydrodynamic-biogeochemical models. The latter two are discussed below.

Hetland and DiMarco (2008) tested the effects of various simple oxygen respiration models (viz. river induced, water column and bottom) implemented on a realistic hydrodynamic model of the TX-LA shelf, and determined that benthic respiration is responsible for most of the variation in the region far from the river influence, while water column respiration is only important close to river mouths. The empirical parameterization for bottom respiration derived in this study has been used by several other model implementations in the NGOM, including Yu et al. (2015a); Ko et al. (2016) and particularly Fennel et al. (2016), who relied on the benefits of using a parameterization dependent only on physical drivers, to isolate natural variability from possible effects of anthropogenic load reduction.

Complex biogeochemical models have also been coupled to hydrodynamic models in order to understand nitrogen and phosphorus limitation effects. However, those implementations seem to work better near the origin of the freshwater plume while not improving the simulations over the far shelf (Fennel et al., 2011, 2013; Justić and Wang, 2014; Laurent et al., 2012; Laurent and Fennel, 2013), and thus the hypoxic extent estimates (Yu et al., 2015b,a). The biogeochemical coupled representation in the high-resolution hydrodynamic model used by Justić and Wang (2014) was able to identify the origin of hypoxia from small isolated pockets in the mid-shelf, near the Mississippi Delta. However, the variability found by the model was mostly studied in relation to physical modulations (water column stratification, bathymetric features, frequency and intensity of fronts, etc). Hence, although the importance of biogeochemical interactions is recognized in the current literature, most authors concur that the physical environment is responsible for most of the variability in the hypoxic region over the TX-LA shelf, and should be understood separately in order to make better assessments of the impacts of changing nutrient loads.

Finally, it is worth noticing that, although model implementations for the TX-LA shelf have been improving over the years, even the highest-resolution biogeochemically coupled models currently in use are not able to represent high frequency variability of DO concurrently in space and time when contrasted to point observations (Yu et al., 2015b; Justić and Wang, 2014). In any case,

this is not surprising considering the underlying chaotic nature of the shelf. Moreover, it has been argued that models are able to reproduce the hydrodynamic field in terms of mean and variance fairly well, signaling that the simulated spatial and temporal structure is indeed similar to that observed (Hetland and DiMarco, 2012). Thus, borrowing from hydrodynamic validations, the future of bottom hypoxia simulations should focus on representing variability in a statistically relevant way, both spatially and temporally, in order to quantify it and determine driving processes.

1.2 Tools and Organization

This dissertation will approach a discussion of the different scales of variability found in the bottom hypoxia that develops over the TX-LA shelf. Special attention is given to relating the variability in the bottom DO to the abundant submesoscale processes that are know to shape the main variability in oceanographic patterns at the surface over the shelf.

The main tool utilized in this investigation is the TXLA model, a realistic hydrodynamic implementation of the Regional Ocean Modeling system (Shchepetkin and McWilliams, 2005; Haidvogel et al., 2008, ROMS). The configuration of the model is discussed more in depth in Chapter 2. The TXLA domain is shown in Fig. presenting snapshots of surface salinity and bottom dissolved oxygen. Visualizations of the TXLA model can be found at the Texas Automated Buoy System website for the years 1993-2017, and simulations of the bottom dissolved oxygen are at http://pong.tamu.edu/tabswebsite/subpages/gallery.php?gallery=oxygen.

In Fig.1.2, annual observation estimates from the LUMCON survey are shown in contrast to the hypoxic extent simulated by the TXLA model (area where DO <60 μM). The 23 years long time series, estimated by the ship-based survey, is a static observation of a very dynamic system. The model allows us to identify different relevant temporal scales that are missing in the annual survey. Moreover, the simulations suggest that the hypoxic area may reach a maximum later than mid-summer. Some years can be seen having hypoxic breakage and regrowth episodes (i.e. 2003, 2010, 2012). This phenomenon has been commented by Rowe and Chapman (2002) relating secondary peaks in the river flow to the strength of hypoxia.

High-resolution observations collected during the MCH project (DiMarco and Zimmerle, 2017)

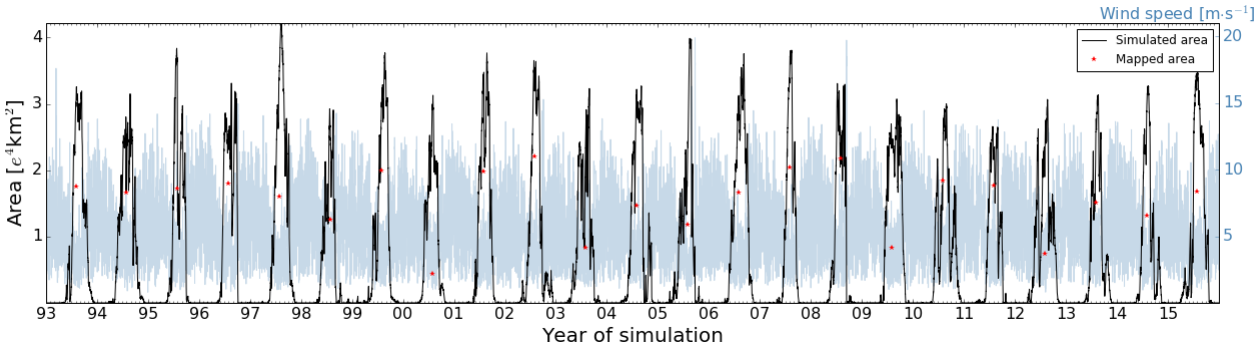

Figure 1.2: Simulated hypoxic area (solid black line) against annual cruise observations in late summer (red stars). Shelf-averaged wind speed is shown in the background.

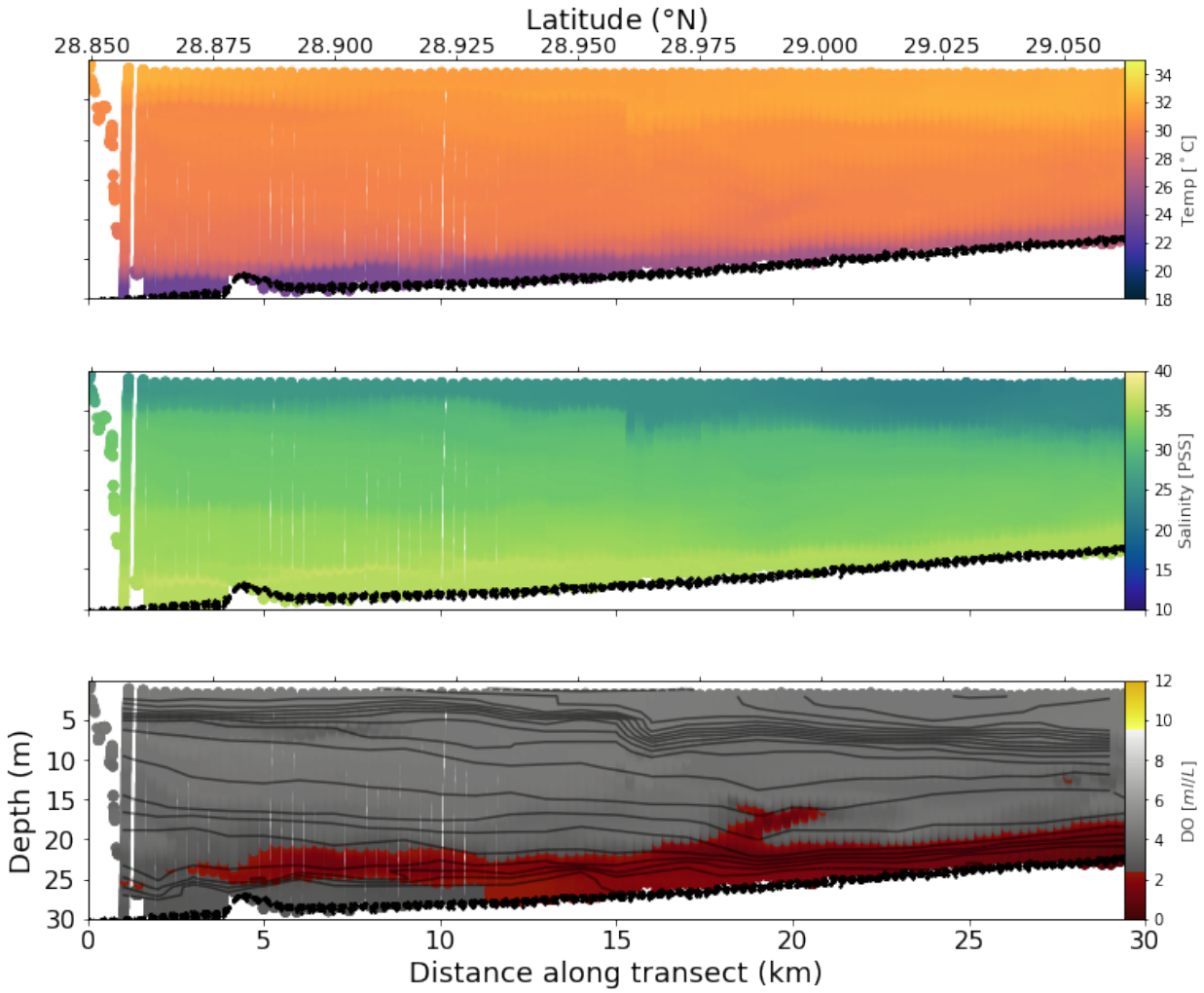

Figure 1.3: Acrobat transect $MSO2 - L8$, captured on Aug-04-2010, showing temperature (top), salinity (middle) and dissolved oxygen (bottom). Data is displayed raw through a scatter plot, with no interpolation, to emphasize the resolution.

are used to complement the analysis and help explain mechanisms in the DO patchiness, to contrast the simulations (see example in Fig. 1.3). Observations were made using a SeaSciences Acrobat towfish, equipped with a SeaBird SBE43 dissolved oxygen sensor. The Acrobat is operated to undulate between 1-2 m from bottom and 1-2 m below surface, at a tow velocity of the vessel of about 5 knots (2.5 $\mathrm{m{\cdot}s^{-1}}$) .

Finally, a set of idealized model setups are implemented to explore physical mechanisms in a simplified manner.

The overarching hypothesis addressed in this document is that the hypoxia occurring on the bottom of the TX-LA shelf is subject to variability ranging from interannual changes in the areal extent to very dynamic patchiness due to the abundance of the energetic submesoscale baroclinic instabilities characteristic of the region, which has an impact on the ecological vulnerability of the shelf. To test this hypothesis, this dissertation is organized as follows.

Chapter 2 will focus on characterizing the variability in bottom oxygen concentrations of the TX-LA shelf at different temporal and spatial scales. Using a set of sub-domains of the TXLA model in the far-field of the Mississippi plume, this chapter relates hypoxia development to physical processes with spatial scales ranging from $\mathcal{O}$(10km) to $\mathcal{O}$(100km), and temporal scales from the near-inertial period to seasonality. A budget decomposition of the oxygen equation is utilized to explore the patterns in relation to submesoscale processes, near-inertial motions, and the weather band. The effect on the structure of the hypoxic volume is related to budget changes across temporal and spatial scales.

Chapter 3 explores the spatial structure of exposure to hypoxia from 23 years of the TXLA model simulation. The relationship to shelf topography and the generation of bottom water intrusions from eddy induced bottom convergence is discussed. It is argued that metrics that consider spatial and temporal structure would have a more meaningful impact than the use of mid-summer hypoxic extent as a measure of severity

Chapter 4 presents an idealized study to establish the modulation of barolinic instabilities over the bottom oxygen distribution, and evaluates forcing and topographic effects.

Chapter 5 draws general conclusions and points to several new directions of research.

2. SMALL-SCALE VARIABILITY OF BOTTOM OXYGEN IN THE NORTHERN GULF OF MEXICO

2.1 Introduction

The seasonal occurrence of hypoxia in the bottom waters of the northern Gulf of Mexico has been monitored for over 30 years (Rabalais et al., 2001c, 2007). In general, the processes regulating the spatial and temporal variability of the hypoxic area in the region are attributed to variations in the nutrient load and the extension of the freshwater envelope generated by the Mississippi-Atchafalaya River system (Rowe and Chapman, 2002; Scavia et al., 2003; Bianchi et al., 2010b). However, most mechanistic studies in the regional literature are concerned with the relationship between these two drivers and the full extent of hypoxia, while the internal variability and short-term shifts have been insufficiently investigated.

Furthermore, the severity of hypoxia has often been equated to its aerial extent, such that most modeling efforts are directed to estimate this quantity with accuracy. Official estimates of extent for managerial purposes are obtained from the annual LUMCON mid-summer cruise measurements (Dale et al., 2008, https://gulfhypoxia.net), and current mitigation plans include nutrient flux reduction goals based on projections derived from correlations of the nutrient load with the mid-summer estimate (Scavia et al., 2003, 2013; Turner et al., 2006).

The limitations of this nutrient-centric view have been discussed by Bianchi et al. (2008, 2010a). Arguments against this simplification include the expected non-linearity of the system (owing to the chaotic nature of a shelf environment), which hinders the predictive capability of historical survey data, the questionability of a metric based on a week-long annual survey to represent a dynamic multi-scale process, and the insufficient knowledge on the ecosystem response to the hypoxic effect and the nutrient load reduction.

In previous studies, bottom hypoxia has been assumed to be a slowly evolving (in scales of weeks to months) and spatially continuous process along the Texas-Louisiana shelf, originating

from riverine eutrophication and stratification (Turner and Rabalais, 2019), and spreading westwards with the river plume. Later studies debunk this idea; Hetland and DiMarco (2008), using a realistic hydrodynamic model of the Texas-Louisiana shelf, conclude that the development of hypoxia in the far-field is primarily a vertical process, and there is not a significant lateral advective component in the growth of the extent.

High-resolution observations support a conceptual model where dissolved oxygen concentration (DO) is modified by the local hydrodynamic field. For instance, measurements captured by a towed undulating vehicle along cross-shore transects West of the Mississippi, reveal irregular morphology in the near bottom structure of the DO (DiMarco and Zimmerle, 2017). It is common to observe high-frequency DO fluctuations in long-term time series collected at near bottom stations (Wiseman et al., 1997; Rabalais et al., 1994, 2001a, 2007; Bianchi et al., 2010b), and such high temporal variability in other regions has been attributed to lateral movement of water masses caused by front and eddy dynamics, internal waves and upwelling (Friedrich et al., 2014).

Because high-frequency multi-scale bottom events are difficult to observe, the application of high-resolution numerical models is useful to investigate processes leading to high temporal and spatial variability. Several implementations of realistic simulations of hypoxia have been developed for the northern Gulf of Mexico (e.g. Fennel et al., 2011; Justić and Wang, 2014). Such models are used to evaluate the effect of different processes on hypoxia, including climate change (Laurent et al., 2018), atmospheric and oceanic patterns (Wang and Justić, 2009; Feng et al., 2014; Yu et al., 2015b,a), biogeochemical pathways (Laurent et al., 2012; Laurent and Fennel, 2013; Fennel and Laurent, 2018), and model settings and parameterizations (Hetland and DiMarco, 2008; Fennel et al., 2013, 2016). Although most of these studies primarily discuss the relationship of the processes with the ability to simulate areal extent or hypoxic volume, in cases when snapshots are reported, the distribution of the bottom DO is shown to be patchy and complex (e.g., Justić and Wang, 2014; Fennel and Laurent, 2018).

The relevance of the finer spatial structures and the periodicity of DO fluctuations to ecological responses have been discussed in several studies (see Levin et al., 2009, and references therein).

It is insufficient to only establish the presence of hypoxia, as other factors - including time and frequency of exposure, and the proximity to oxygenated pockets - are relevant to mortality, loss of diversity, behavioral and physiological changes in organisms (Zhang et al., 2009), and changes in biogeochemical pathways (Eldridge and Morse, 2008; Middelburg and Levin, 2009). However, little is known about realistic submesoscale spatial and temporal shifts of low oxygen in the region, and the effects at an ecosystemic level.

To promote research in this direction, the primary goal of this chapter is to explore the relevance of different spatial and temporal scales in the structure of hypoxia in the far-field of the Mississippi plume. To do so, we decompose the DO budget and quantify the separate effects of advection, diffusion, and bottom respiration. By using a realistic hydrodynamic model of the Texas-Louisiana shelf, we challenge the conceptual model of a slow westward-moving hypoxic volume, against a more locally controlled system subject to the passage of dynamic instabilities, the local near-inertial period, and the weather band.

2.2 Methodology

2.2.1 Realistic numerical model of the Texas-Louisiana shelf

We use the TXLA model, which is an implementation of the Regional Ocean Modeling System (ROMS, Shchepetkin and McWilliams, 2005; Haidvogel et al., 2008) for the Texas-Louisiana shelf. This implementation has been previously validated and has shown to resolve local submesoscale processes and fronts reasonably well (Hetland and DiMarco, 2012; Zhang and Hetland, 2012; Zhang et al., 2014). Here we examine the development of hypoxia during 2010, in a small region of the TXLA domain in the far-field of the Mississippi plume (Fig.2.1).

The model grid has 30 terrain-following vertical levels, and more layers are concentrated near the surface and bottom to ensure adequate resolution in the boundary layers. While the horizontal resolution of TXLA ranges from 0.65 km near the coast to about 3.7 km on the outer slope area, the mean resolution over the region of interest is about 2 km. The TXLA implementation uses a 3^{rd}-order upwind horizontal scheme and a 4^{th}-order centered vertical scheme (4^{th}) for momentum

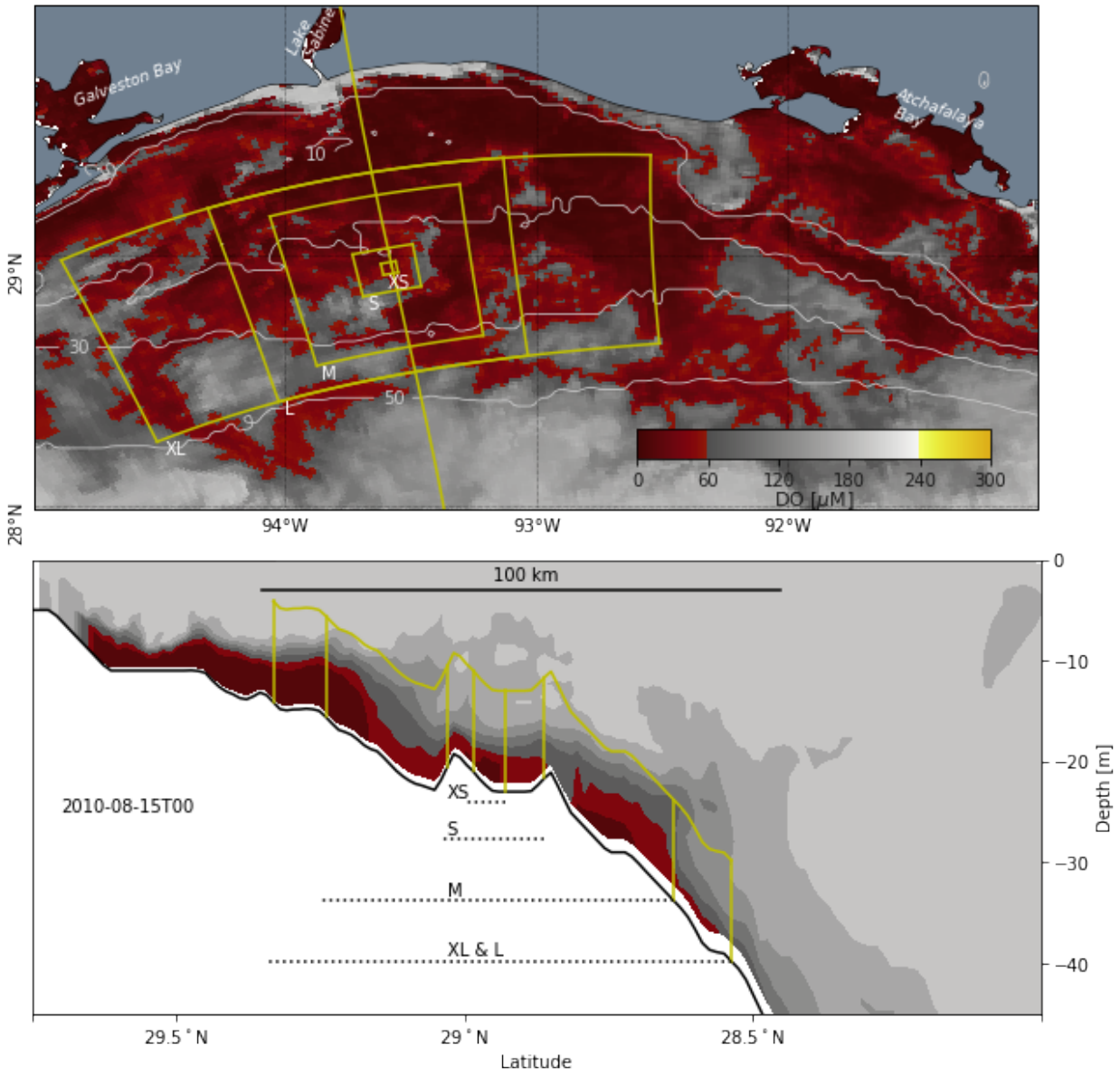

Figure 2.1: Snapshot of modeled dissolved oxygen concentration showing the bottom layer (top) and a cross-shore section in the center of the domains (bottom). Five domains (yellow lines) were selected for statistical comparison in the DO budget analysis. The domains and approximate areas are defined in Table 2.1, with spatial scales that can capture mesoscale (XL, L, M), and submesoscale (S, XS) processes. Volume in all domains was closed at 10 m above the bottom.

advection, and MPDATA (Multidimensional Positive Definite Advection Transport Algorithm) for tracer advection (Smolarkiewicz and Margolin, 1998). The k-ω turbulence closure module is used in the vertical (Warner et al., 2005) and horizontal mixing is set to a constant value of 5.0 m^2 s^{-1} for momentum and 1.0 m^2 s^{-1} for tracers, both of which are scaled with the grid size.

Surface forcing and fluxes are obtained from the ERA-interim reanalysis (Dee et al., 2011). A bulk flux parameterization, adapted from the COARE algorithm described in Fairall et al. (1996), is used to calculate surface flux. The main freshwater flux is specified from the Tarbert Landing station of the US Army Corps of Engineers. The transport is divided such that 30% sources from the Atchafalaya and the remainder is split in 50% each to the East and the West of the Mississippi Delta. Freshwater fluxes from the seven western rivers (Nueces, San Antonio, Lavaca, Brazos, Trinity, Sabine, and Calcasieu) are specified from the daily measurements provided by the US Geological Survey. River salinity at all source points is set to zero, and the streamflow temperature is estimated following Sinokrot and Stefan (1993). Tides are not included as they are weak over the shelf region (DiMarco and Reid, 1998).

2.2.2 Oxygen dynamics

Oxygen is treated in the model as a non-conservative tracer; the rate of change in oxygen concentration should account for conservative (advection) and non conservative (diffusion) physical processes, and biogeochemical sources and sinks. The equation for the local time rate of change in oxygen is:

$$\frac{\partial Ox}{\partial t} = -\left(u\frac{\partial Ox}{\partial x} + v\frac{\partial Ox}{\partial y} + w\frac{\partial Ox}{\partial z} \right) + \frac{\partial}{\partial z} Ak_v \frac{\partial Ox}{\partial z} , \tag{2.1}$$

subject to the boundary conditions described below (e.q. sediment oxygen demand). The first term on the right-hand side is the tri-dimensional advection, and the second is the vertical diffusion. The only parametrization implemented in the diffusion term is the vertical tracer diffusivity constant Ak_v. While horizontal diffusivity is typically small compared with horizontal advection or vertical mixing, we are aware of an unquantified amount of numerical mixing due to the tracer

advection scheme of the model (Burchard and Rennau, 2008), and the integrated effects of this error may be non-negligible.

In our study, water column non-conservative terms (photosynthesis and respiration) are neglected for a number of reasons. First, photosynthesis and respiration are known to be dominant only near to the freshwater inflow. Nutrients are diluted in the far-field, causing water column oxygen production and removal fluxes by phytoplankton to be small compared to benthic respiration (Hetland and DiMarco, 2008; Bianchi et al., 2010b). Second, the simplest oxygen model is preferred because our primary goal is to isolate the physical drivers. This allows us to gain a better comprehension of the role of the shelf hydrodynamics in the development of hypoxia. Finally, models using only benthic respiration based on the Hetland and DiMarco (2008) bottom oxygen flux parameterization, described below, have shown excellent skill at reproducing observed hypoxic extent (Fennel et al., 2016).

Sources and sinks are only defined as boundary conditions. A saturation state of DO is imposed at the surface layer and in the freshwater inflow for every time step. Oxygen saturation in the model is calculated using an algorithm based on Weiss (1970).

For a bottom boundary condition, the DO flux is induced by sediment oxygen demand (SOD) following the parametrization proposed by Hetland and DiMarco (2008), where:

$$SOD \; = \; -6 \times \left[\mu MO_2 \quad m^{-2}d^{-1}\right] \times 2^{T[^oC]/10} \times \left(1 - exp\left(-\frac{Ox}{30\,[\mu MO_2]}\right)\right) \tag{2.2}$$

In the text, SOD and bottom respiration are used interchangeably.

2.2.3 Domains and oxygen budget

To analyze the DO budget, we chose a region on the shelf between 95 and 91°W, constrained to depths between 12 and 50m. To understand if average processes occurring at large scales are similar to those occurring at small scales, we define a set of progressively smaller sub-domains to analyze the balance statistics for different spatial scales. For ease and accuracy of computation,

Table 2.1: Domains defined for the budget analysis. The control volume (V_C) is obtained by integrating to domain from the bottom up to 10 m above. Areas are presented for each domain with the approximate identifiers used in plots. The length is the along-shore direction (ξ). Scale order of magnitude is used throughout the text, as well as the domains categorization of mesoscale or submesoscale.

Domain ID	Grid size $\eta \times \xi$	V_C $[km^3]$	Area $[km^2]$	Length $[km]$	Scale $\mathcal{O}(km^2)$	
TXLA	191×671					
XL	70×113	2×10^3	$19728 \rightarrow 20 \times 10^3$	234	10^4	Mesoscale
L	70×56	1×10^3	$9962 \rightarrow 10 \times 10^3$	119	10^4	"
M	54×37	5×10^2	$5032 \rightarrow 5 \times 10^3$	77	10^3	"
S	16×13	50	$462 \rightarrow 500$	26	10^2	Submesoscale
XS	5×4	5	$50 \rightarrow 50$	8	10	"

the edges of the sub-domains follow the grid cells in the native η and ξ directions of the grid. The subdomains are overlaid in Fig.2.1, and the specifications are presented in Table 2.1.

2.2.3.1 Local budget

The local budget is calculated for every grid cell in the region of interest, between h and z_{10}, where h is the water depth and z_{10} is the depth 10 m above the bottom. z_{10} is chosen somewhat arbitrarily as a reasonable and practical upper bound on the domain, because observed hypoxic thickness rarely surpasses that value (Bianchi et al., 2010b). The local budget is then defined as:

$$\begin{aligned}\left(\int_{-h}^{-z_{10}} \frac{\partial Ox}{\partial t}\, dz\right)\, dx\, dy\Big|_{x_i,y_j} = & \int_{-h}^{z_{10}} (u\, Ox)\; dA_{yz}\Big|_{x_{i+1/2},y_j}^{x_{i-1/2},y_j} + \int_{-h}^{z_{10}} (v\, Ox)\; dA_{xz}\Big|_{x_i,y_{j+1/2}}^{x_i,y_{j-1/2}} \\ & - (w\, Ox)\; dx\, dy\Big|_{x_i,y_j,z_{10}} + \left(Ak_v \frac{\partial Ox}{\partial z}\right)\, dx\, dy\Big|_{x_i,y_j,z_{10}} \\ & + (SOD)\; dx\, dy\Big|_{x_i,y_j,h} \end{aligned} \tag{2.3}$$

All flux terms of Eq.2.3 are solved numerically at the velocity points over the Arakawa C-grid (Arakawa and Lamb, 1977), except for the vertical advection component – the $w\, Ox$ term – which

is set as the reminder of the balance. We found that it was difficult to interpolate the fluxes normal to the upper bound with acceptable accuracy.

The spatial mean rate of change of DO in a domain, and the temporal average, are defined respectively as follows

$$\left\langle \frac{\partial Ox}{\partial t} \right\rangle_{DOM} = \frac{\iint_{A_{xy}} \left(\int_{-h}^{-z_{10}} \frac{\partial Ox}{\partial t}\, dz \right) dx\, dy}{\iint_{A_{xy}} dx\, dy} \tag{2.4}$$

$$\overline{\left\langle \frac{\partial Ox}{\partial t} \right\rangle}_{DOM} = \frac{\int_{period} \left\langle \frac{\partial Ox}{\partial t} \right\rangle_{DOM} dt}{\int_{period} dt}, \tag{2.5}$$

where the brackets represent a spatial mean and the overline a temporal average. Mean fluxes are calculated using this definitions for each term of the budget, providing statistics for spatial scales ranging from $\mathcal{O}(10^1$ km$^2)$ to $\mathcal{O}(10^4$ km$^2)$. Temporal averages and standard deviations are calculated for periods defined to identify stages in the development of hypoxia.

2.2.3.2 Domain total budget

The total DO budget of a domain volume (V_{DOM}) is the result of the fluxes through all faces of the volume at the East, West, South and North sides of the domain, and the top and bottom surfaces. Given a cross-face DO flux, such as along-shore advection or $\iint_{A_{yz}} (u\, Ox)\ dy\, dz$, the spatial Reynolds average is defined as

$$\langle u\, Ox \rangle = \frac{\iint_{A_{yz}} (u\, Ox)\ dy\, dz}{\iint_{A_{yz}} dy\, dz} \tag{2.6}$$

Substituting the area-weighted spatial average in the domain volume integrated DO equation (i.e., eq.2.3 for a domain) allows to separate the effects of the mean flow from the perturbations applying a spatial Reynolds decomposition such that

$$\langle u\, Ox \rangle = \langle u \rangle \langle Ox \rangle + \langle u' Ox' \rangle\,. \tag{2.7}$$

The total volume domain budget equation then becomes:

$$V_{DOM}\frac{\partial \langle Ox\rangle}{\partial t} = A_{yz}\langle u\rangle\langle Ox\rangle\Big|_E^W + A_{yz}\langle u'Ox'\rangle\Big|_E^W + A_{xz}\langle v\rangle\langle Ox\rangle\Big|_N^S + A_{xz}\langle v'Ox'\rangle\Big|_N^S$$
$$-A_{xy}\langle w\rangle\langle Ox\rangle\Big|_{z_{10}} - A_{xy}\langle w'Ox'\rangle_T\Big|_{z_{10}} + A_{xy}\langle SOD\rangle\Big|_h \quad (2.8)$$

The spatial mean vertical flow $\langle w\rangle$ is defined as the flow perpendicular to the z_{10} surface and calculated diagnostically from the continuity equation where

$$A_{xy}\ \langle w\rangle = -\left(A_{yz}\ \langle u\rangle + A_{xz}\ \langle v\rangle\right). \quad (2.9)$$

For practical reasons we define the total vertical turbulent flux as the combination all perturbations crossing the top surface, and the mean vertical diffusive flux, such that

$$\langle w'Ox'\rangle_T = \langle w'Ox'\rangle - \langle Ak_v\rangle\left\langle\frac{\partial Ox}{\partial z}\right\rangle - \left\langle Ak_v'\frac{\partial Ox'}{\partial z}\right\rangle, \quad (2.10)$$

which is quantified as the remainder of the balance. Thus, this incorporates vertical mixing, vertical advection anomaly, and normal mixing.

2.3 Results

2.3.1 Modeled DO and observations

DO concentration changes rapidly in the simulations, and often displays a complex spatial structure. In the snapshot shown in Fig.2.1, although the area affected by hypoxia stretches nearly 400 km along the shelf, variability is also evident at much smaller scales, down to a few kilometers. The appearance of eddy-like oxygenation cores enclosed by low DO is a common occurrence (Fig.2.1A). These features appear as disruptions of low DO water along cross-shore sections (Fig.2.1B).

Water masses with simulated DO concentrations under the hypoxic threshold are generally contained within 10 m above the bottom (99% of the time for August 2010). The hypoxic layer

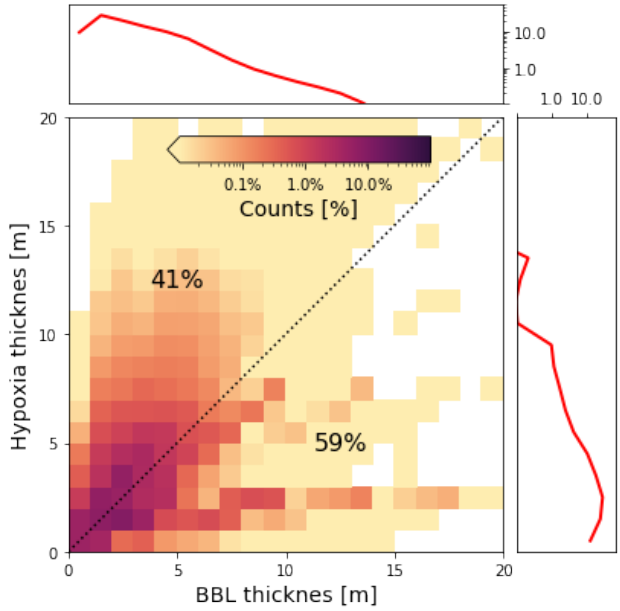

Figure 2.2: Two-dimensional histogram of hypoxia and BBL thickness, for all single simulated occurrences in August in the region of interest. Counts are expressed as percentage of occurrence, and thickness for both parameters is calculated operationally (see text). Occurrences above the diagonal correspond to hypoxic intrusions above the BBL.

is often contained under the bottom pycnocline, which acts as a cap on the bottom boundary layer (BBL), but disruptions of the BBL occur in the form of intrusions of low bottom DO waters into the mid water column (e.g., cross-section in Fig.2.1). Fig.2.2 shows this relationship in our simulation. Here, the thickness of the BBL is calculated operationally as the minimum distance above the bottom where the vertical density gradient is larger than 0.1 kg m^{-4}, and the hypoxic thickness as the maximum distance above the bottom where DO $\leq$60 μM. Intrusion events are quantified by the counts occurring above the 1:1 line, that is, hypoxic water present above the bottom pycnocline, and add up to 40.6% of the points where hypoxia was found. These intrusions play an important roll in the exchange of DO and ventilation of the low oxygen bottom waters.

For comparison, Fig.2.3 presents examples of observed along- and cross-shore disruptions of bottom hypoxia (transects MS01_A13, MS02_L06), as well as intrusions of lower DO concentration, into the mid water column (MS01_A10, MS02_L08), that were captured during surveys in 2010, and are similar to our simulations. The development of these features seems to be related

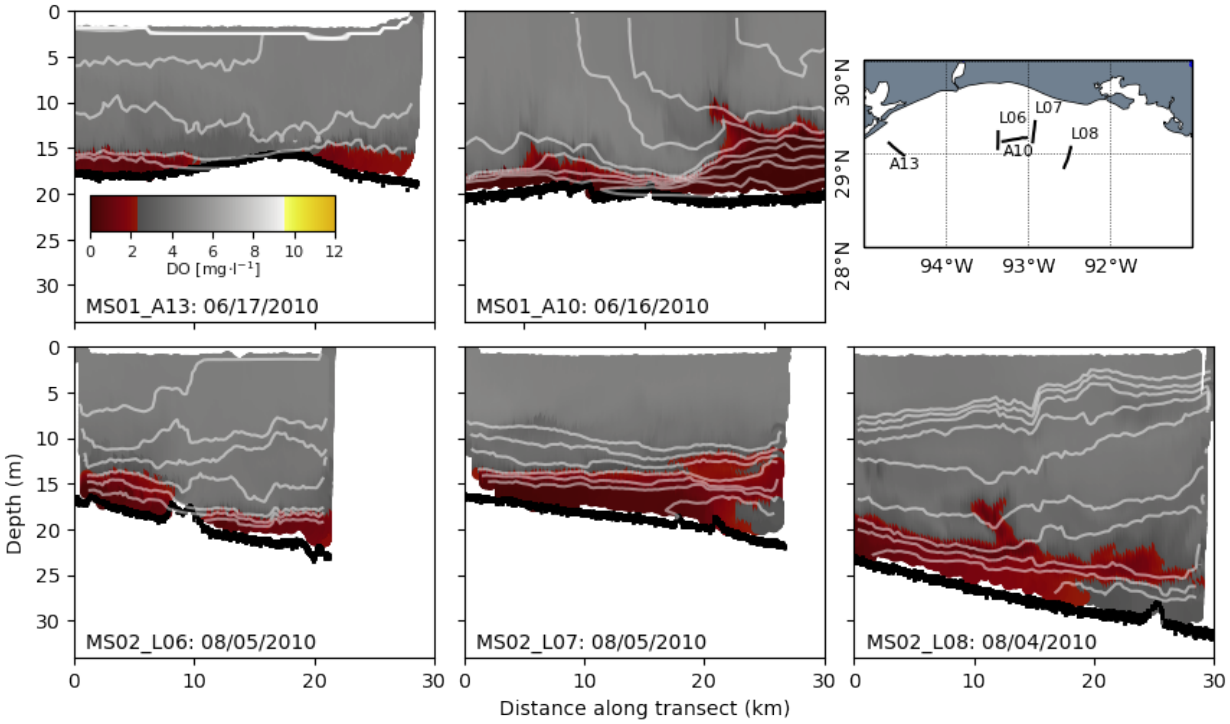

Figure 2.3: Observed dissolved oxygen concentration and isopycnal contours in the region of study, following the along- (top) and across- (bottom) shelf transects shown in the top right panel. Features captured during surveys in summer 2010 include hypoxic water mass disruptions (left) and intrusions in the mid water column (center and bottom right).

to the interaction of fronts (seen in the isopycnals) and bathymetry. Due to sampling limitations, the 2-dimensional horizontal variability of the bottom oxygen distribution, such as that simulated by our model (Fig.2.1), has not been observed up to this date. But we find the cross-sections of simulated and observed DO to be qualitatively comparable; both the observations and the model show similar morphological complexity of bottom hypoxic waters with regions of no hypoxia and regions with intrusions of low DO water. More cross-sections of high-resolution observations of several parameters and other years can be consulted in the MCH Atlas (DiMarco and Zimmerle, 2017, https://sites.google.com/a/tamu.edu/mchatlas/).

2.3.2 Development of hypoxia

Fig.2.4A shows the evolution of the simulated areal extent of hypoxia during 2010. Although a seasonal trend is the dominant pattern, it is not continuous. The duration of the entire hypoxic period is about six months (end of May to end of November). However, after hypoxia fully develops, two large oxygenation events nearly destroy it. The first oxygenation event occurs rapidly, on a scale of days, while the second takes a few weeks. Hypoxia reforms over weeks to reach a size similar to that before the first oxygenation event in about a month, and continues growing until it peaks at about $1.5 \times 10^4 \mathrm{km}^2$ by the end of August. The second oxygenation event responds to two closely timed mixing events – weaker than that associated with the first oxygenation event – on the scale of a week each. When hypoxia develops for the third time, the maximum areal extent reached is about half of the previous two peaks. This type of oxygenation event, followed by a rapid re-formation of hypoxia, is not uncommon and has been simulated for other years (e.g., see simulations for years 2012, 2013, and 2017 at the Texas Automated Buy system website, http://pong.tamu.edu/tabswebsite/subpages/gallery.php?gallery=oxygen).

The areal distribution of bottom DO concentrations (namely, the area exposed to a certain DO concentration) matches the hypoxic extent change in time. A slow reduction of DO starts as early as February, but a much sharper decline appears in mid-May (Fig. 2.4B). Extensive regions with anoxia (near zero concentrations) – $\mathcal{O}(10^3 \mathrm{km}^2)$ – are associated with peaks in the extent while the spreading of regions with saturation levels above 200 μM matches sharp declines in the extent.

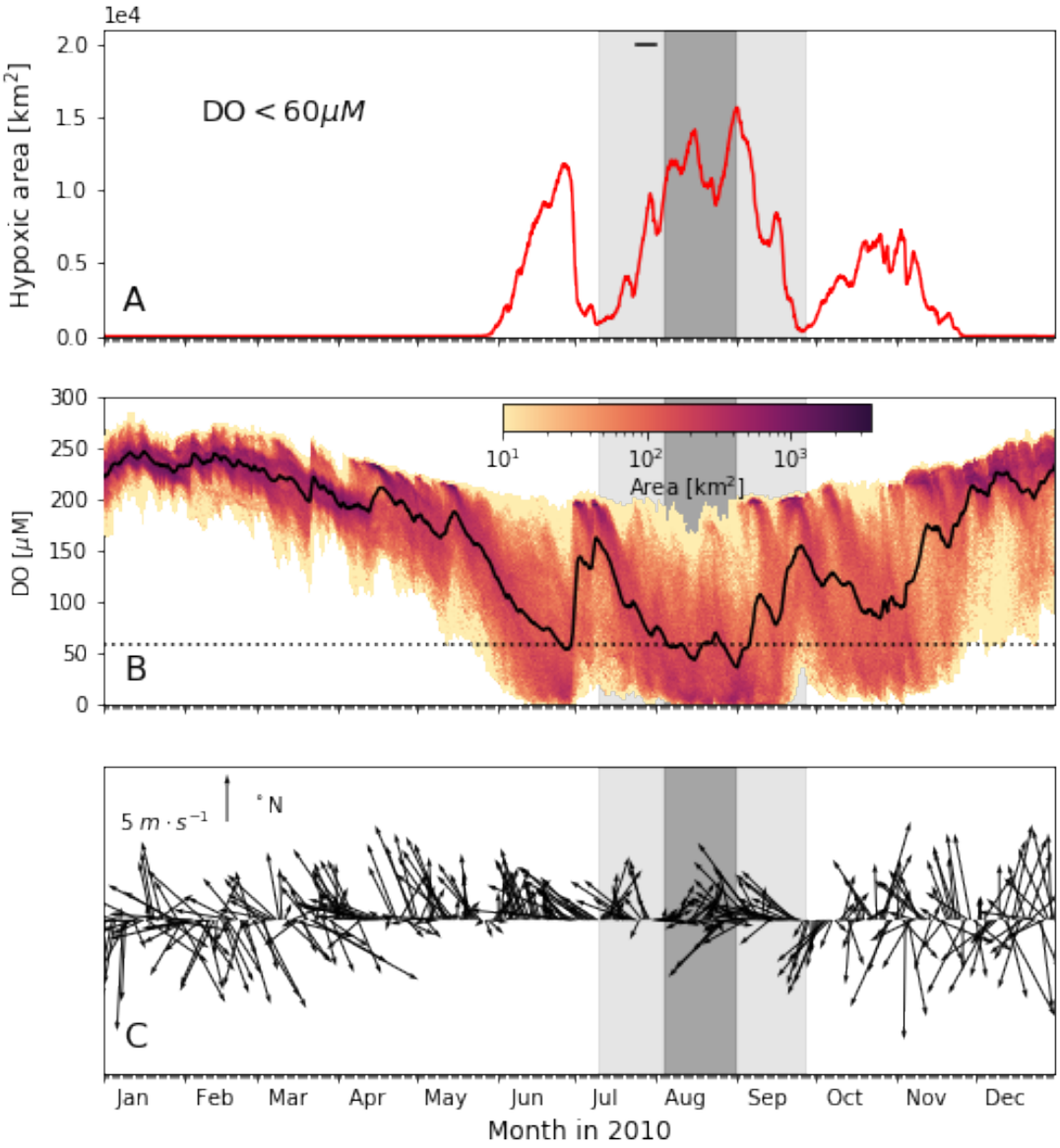

Figure 2.4: Time evolution of hypoxia in the largest domain during 2010: A). Modeled bottom hypoxic extent, using a DO threshold of $60\mu M$. The small line at the top indicates the LUMCON estimate for the year and the duration of the survey. B). Weighted property histogram showing the areal distribution of bottom DO concentration. The solid line is the mean bottom DO. The dashed line marks the hypoxic threshold. C). Domain averaged wind vectors. Shadowed regions mark the onset, maintenance, and destruction period defined in Table 2.1.

Sudden increases in the extent of saturated waters (seen as darker spots in the top edge of the property histogram) are a response to the advection and turbulent mixing of oxygenated water in the control volume. In contrast, a slow dissipation of oxygen-rich waters is accompanied by a relatively constant reduction in DO concentration (~25μM per week), which is most likely a combined effect of bottom respiration and dilution.

The initial onset and final destruction of hypoxia is timed with the seasonal change in the wind pattern. Offshore winds are weak or absent between mid-May and October, with short appearances that coincide with the oxygenation periods and sudden drops in extent (Fig. 2.4C). Hypoxia is more extensive when winds are weak and downwelling favorable, e.g., during most of August. Here we define the onset stage when the hypoxic region is growing rapidly, the destruction stage during fast decline, and a maintenance stage in between, and we focus on the second hypoxic peak.

2.3.3 Persistence of hypoxia

To challenge the notion that hypoxia is a relatively continuous and slowly evolving event, we choose to analyze the month of most severe hypoxia closely, covering most of the maintenance stage. The top left panel on Fig.2.5 presents the time of exposure during August 2010, when the modeled DO concentration at the bottom is below $60\mu M$. Although there are some regions where hypoxia is long-lasting, the affected area is not continuous, but rather disrupted by several cores that are weakly exposed. The length scale of these regions ranges from 10 to 100 km^2.

This spatial distribution of exposure appears to be modified by relatively rapid changes in the bottom slope (i.e., ridges or channels seen in top right panel off Fig.2.5). It is also evident that exposure is generally weaker in regions where stratification is weaker and the BBL is thicker (bottom panels in Fig.2.5). These observations hint towards some topographic control over the boundaries of the prevalence of hypoxia on the shelf. However, the mechanism of this boundary formation escapes the scope pursued herein and will be explored in a later study.

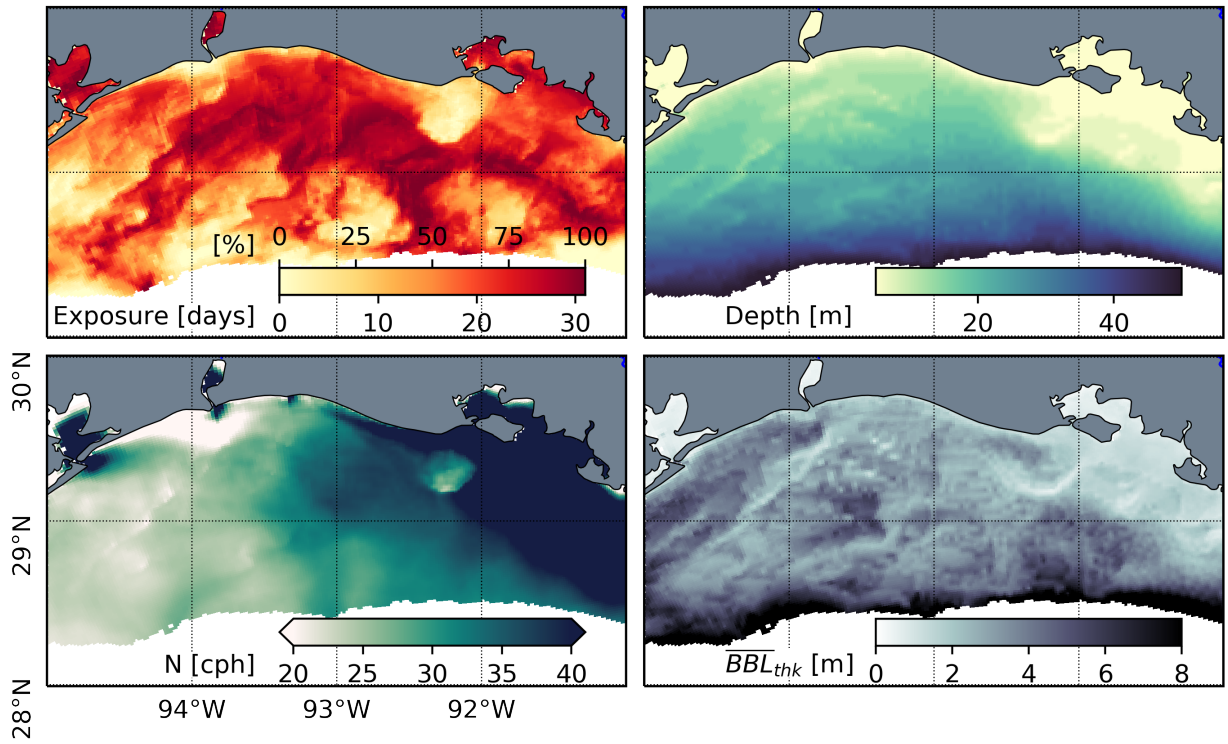

Figure 2.5: Top: Exposure to hypoxia in August 2010, counted as the total amount of time with a bottom DO concentration below 60μM (left); bathymetry (right). Bottom: Mean state of the column mean buoyancy frequency (N) (left) and the thickness of the bottom boundary layer (right).

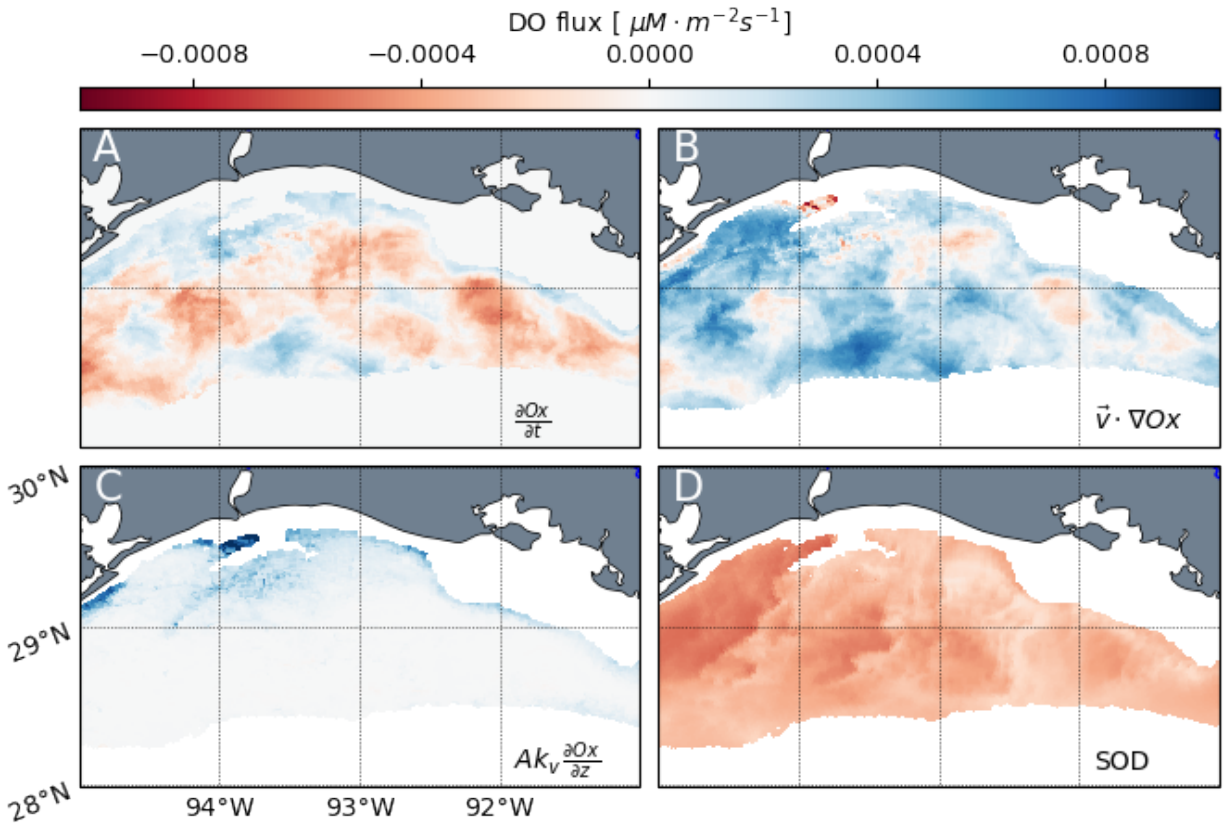

Figure 2.6: Monthly average (August) of the DO budget balance in the bottom water column (up to 10 m above the bottom). Rate is mostly balanced by net advection and the sediment oxygen demand. Vertical diffusion is visible in shallow regions with bathymetric quirks.

2.3.4 Dissolved Oxygen budget

2.3.4.1 Average spatial distribution

The determine the main physical drivers of small scale shifts in hypoxia, we decomposed the DO budget balance for every grid cell of the region of interest for depths between 12 and 50 m. Fig.2.6 presents the August average of the main budget terms, where positive and negative fluxes indicate volume integrated gains or losses of DO of the bottom water column up to 10 m.

The average rate of change of oxygen concentration in time is shown in the top-left panel. East of about 93°W, where the shelf is narrow, the water column has a net loss of DO, with oxygenation occurring only inshore. To the West, two ring-like structures are observable, with a net loss region

enclosing oxygenation cores. This spatial structure is primarily controlled by the balance between the net advection and bottom respiration terms. The location of the strongest DO gain through net advection coincides with the oxygenation cores and regions seen in the mean rate. Conversely, regions where DO is advected out of the water column, coincide with regions of large negative rate. Where the mean advection is positive but weak, bottom respiration overcomes it, resulting in a net DO loss.

Although mean bottom respiration is relatively constant in space, a few fronts are visible: a weakened flux on the West side limits these enhanced respiration fronts. These fronts appear as a somewhat regular feature for other months (not shown) and are also consistent with fronts found in exposure time (Fig.2.5).

The features found in the spatial structure of the rate of change have similar length scales to those of baroclinic instabilities generated at the surface, although direct correlation between surface and bottom features was not found. However, surface instabilities can generate ventilation through eddy induced bottom convergence (Zhang and Hetland, 2018).

2.3.4.2 Budget statistics

To compare the budget balance across different spatial scales, we calculated mean fluxes for every domain shown in Fig.2.1, and defined in Table 2.1. We chose to analyze the second hypoxic peak, separating stages of onset, maintenance, and destruction, approximately covering the months of July, August, and September, respectively. Stage statistics across domains are shown in Fig.2.7. Net advection is responsible for the main variability in rate, for all domains and months. This variability is much smaller in the net term than in its components. There is a strong shift in the scale of variability between mesoscale containing domains (5×10^3km^2 and larger), and submesoscale containing domains (500 and 50 km^2), with advection variability increasing in almost one order of magnitude in the submesoscale. This change across scales indicates the presence of dynamical features that modulate bottom oxygen with sizes on the order of $\mathcal{O}(10^3$km$^2)$ or less.

During onset (July), when the hypoxic areal extent starts to grow, the bottom is slightly oxygenated by advection (small positive median), but this flux is not strong enough to overcome bot-

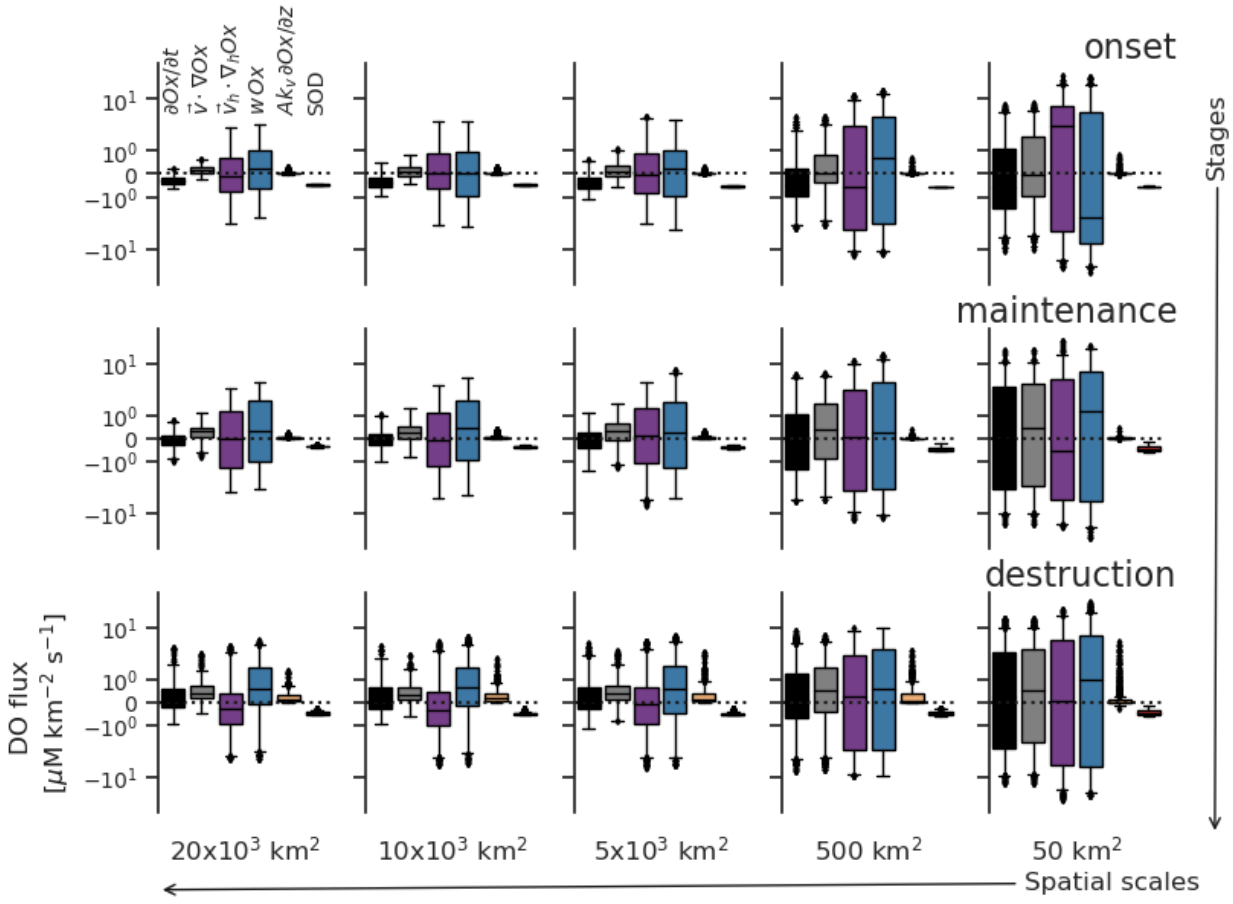

Figure 2.7: Boxplots of period averaged local budget terms across domains, during the onset (~June), maintenance (~August), and destruction (~September) of the second peak of hypoxic extent in 2010. Boxes enclose lower to upper quartile values, and whiskers extend to the interquartile range, with the line showing the median. Fluxes shown are DO rate of change, net advection (total, and horizontal and vertical), vertical diffusion and sediment oxygen demand.

tom respiration, which is stable. This balance generates a net oxygen loss across all domains. In maintenance (August), the hypoxic extent is relatively stable, with the median rate close to zero. This balance results from an increase in the advective flux, which equals the bottom respiration. Finally, advection is dominant during the destruction stage (September), mostly from its vertical component, reducing stratification and allowing vertical diffusion to contribute to a net gain of oxygen. The spurious nature of enhanced mixing is seen in the increased presence of values outside the 95% confidence interval in the diffusion term, which increases at smaller spatial scales.

Fig. 2.8 shows time series of the mean balance terms for four sub-domains (except $10 \times 10^2 km^2$). For all cases, DO rate is seen oscillating in a quasi-diurnal pattern, with the frequency of the near-inertial period of the region. Despite fluctuations, the rate of change is mostly negative during the onset (except for a couple of episodic events), oscillates around zero in August, and has positive episodic bursts in September.

Advection drives the primary oscillation of the DO rate. Although the horizontal and vertical components are out of phase, in a convergence-divergence pattern, the oxygen transport does not cancel out completely, resulting in a net flux. This net flux is an order of magnitude or more smaller than the individual components (see the range of net advection vs. components in Fig 2.7). Correlation coefficients for the horizontal and vertical advection mean terms in all domains range from 0.86 to 0.9 ($p \ll 10^{-3}$).

Vertical diffusion through the 10 m above the bottom surface is the smallest term of the balance but becomes relevant during the spurts in September (as well as the beginning of July, which corresponds to the decline of the first areal peak). During these events, bottom divergence is maintained for several days (negative horizontal advection), producing a downward flux of oxygenated waters strong enough to break stratification and allow the enhancement of diffusion. In contrast to periodic oscillations and episodic bursts, sediment oxygen demand is seen to be relatively constant in time and of similar magnitude across all spatial scales, with a mean value close to 0.4×10^{-3} kg m^{-2} s^{-1}.

When comparing the time series across spatial scales, we found that the two domains with

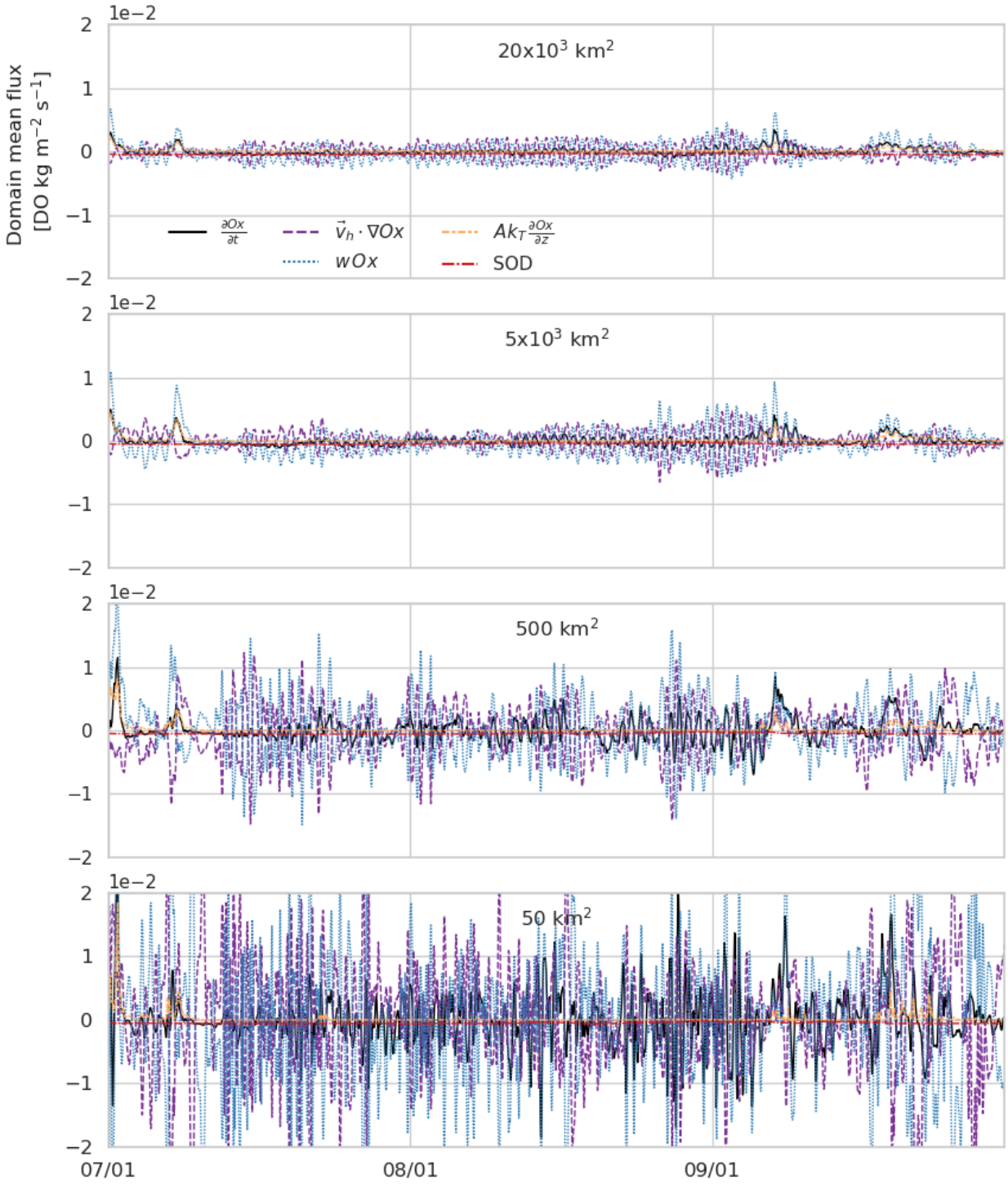

Figure 2.8: Time series of budget fluxes averaged over the volume control for different domains. The $10 \times 10^3 km^2$ domain is not included as it behaves similarly to the $20 \times 10^3 km^2$ domain. $\mathcal{O}(10^3 \text{km}^2)$ domains can contain mesoscale features, but smaller domains are sensitive to submesoscale features.

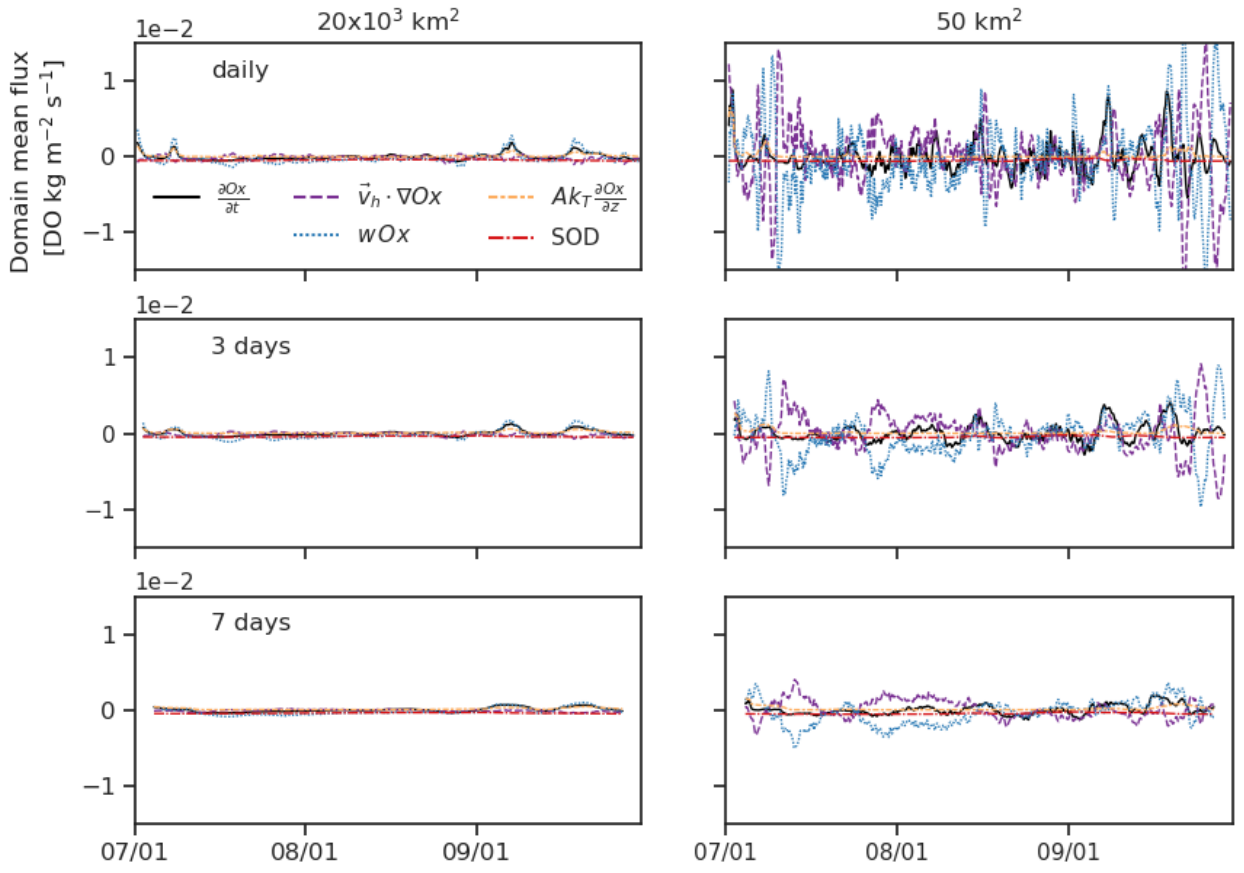

Figure 2.9: Running mean of budget fluxes over one mesoscale (20×10 km^2, left) and one submesoscale (50 km^2, right) domain. The frequencies applied for the running mean were: daily (top), 3 days (middle), and 7 days (bottom).

areas of the order of $\mathcal{O}(10^4\text{km}^2)$ had similar patterns, with oscillation bounds under $\pm5 \times 10^{-3}$ kg m^{-2} s^{-1} for both components of advection. The amplitude of the bounds slightly increase when averaged over the $\mathcal{O}(10^3\text{km}^2)$ domain, but increased fivefold in the $\mathcal{O}(10^2\text{km}^2)$ domain, and has about one order of magnitude increment in the $\mathcal{O}(10\text{km}^2)$ domain.

As noted, most of the variability within the balance is related to the quasi-diurnal period, so we applied a running mean to filter out this signal. For comparison, filtered time series of a domain representing mesoscale ($\mathcal{O}(10^3\text{km}^2)$, left) and another for submesoscale ($\mathcal{O}(50$ km$^2)$, right) are shown in Fig.2.9. A daily filter applied over the time-series leaves only the synoptic time scale variability (5-7 days) in the domains enclosing mesoscale processes. Four positive peaks in rate

remain, two at the beginning of July, corresponding to the time of rapid destruction of the first hypoxic peak, and two across September, corresponding to the decline of the second hypoxic peak. These peaks are driven by oxygenation from the top by advection, reflecting maintained downwelling episodes and increased mixing lasting from 3 days to a week. Conversely, negative rate periods are associated with upwelling (negative vertical advection). Lower frequency filters, up to a week, preserve the same pattern, and the dominance of bottom respiration becomes evident excepting during the four oxygenation periods, and three upwelling periods (two in late July, one in August).

We found much more variability in the submesoscale domains. In addition to the four synoptic peaks found in the mesoscale, DO rate changes from positive to negative every 3 to 5 days in the $\mathcal{O}(10^2 \text{km}^2)$ domain, and advective subinertial fluxes continue to be dominant over the entire time series. Furthermore, the dominance of the convergence-divergence pattern remains after applying 3 and 7 days time filters in the submesoscale mean balance time series. These oscillations are a clear signal of submesoscale features enclosing DO anomalies, crossing the domain over a period lasting from a few days to a week, and causing local rate anomalies of the order of 10 kg $\text{m}^{-2}\text{day}^{-1}$.

2.3.4.3 Mean flow and perturbations

A Reynolds decomposition applied to a total volume budget allows us to separate the effect of the mean flow from the perturbations caused by dynamic instabilities crossing domain boundaries. Table 2.2 shows stage (onset, maintenance, destruction) averaged fluxes normalized by the magnitude of the bottom respiration for all subdomains. The oxygen loss rate is about 60 to 74% of the sediment demand flux during hypoxia onset across all domains. This ratio reduces to 15 to 24% during the maintenance stage and transforms into gain during the destruction period.

The largest term across all domains and during maintenance and destruction stages by far is the vertical turbulent flux, which is the primary oxygenation source. Mean horizontal fluxes are smaller but still an important component of the budget across all domains, and dominant in the submesoscale domains (S and XS). In general, the cross-shore component accounts for an oxygen loss, while the along-shore component is variable. The effect of horizontal perturbations is small

Table 2.2: Time averages of total volume DO fluxes normalized by bottom respiration, decomposed in mean flow and perturbations (i.e. $\langle u \rangle \langle o \rangle$ and $\langle u'o' \rangle$).

Domain	Stage	$V \langle o \rangle_t$	$A_{yz} \langle u \rangle \langle o \rangle$	$A_{xz} \langle v \rangle \langle o \rangle$	$A_{yz} \langle u'o' \rangle$	$A_{xz} \langle v'o' \rangle$	$A_{xy} \langle w \rangle \langle o \rangle$	$A_{xy} \langle w'o' \rangle_T$	$A_{xy} \langle sod \rangle$
XL - $20 \times 10^3 km^2$	onset	-0.60	0.26	-0.19	0.05	-0.04	-0.01	0.32	-1.0
	maintenance	-0.24	-0.26	-0.30	-0.14	-0.03	0.06	1.43	-1.0
	destruction	0.70	-0.05	-0.16	-0.04	-0.08	0.03	1.99	-1.0
L - $10 \times 10^3 km^2$	onset	-0.72	0.61	0.08	0.15	0.00	-0.03	-0.53	-1.0
	maintenance	-0.13	-0.33	-0.32	-0.13	-0.03	0.03	1.65	-1.0
	destruction	0.64	-0.59	-0.35	0.02	-0.04	0.03	2.57	-1.0
M - $5 \times 10^3 km^2$	onset	-0.71	0.79	-0.18	0.07	-0.06	-0.01	-0.32	-1.0
	maintenance	-0.21	0.40	-0.47	-0.13	-0.07	0.01	1.05	-1.0
	destruction	0.69	-0.20	-0.17	0.17	-0.04	0.00	1.91	-1.0
S - 500 km^2	onset	-0.63	0.86	-2.20	0.11	0.05	0.00	1.55	-1.0
	maintenance	-0.21	2.38	-3.38	0.50	-0.43	0.00	1.73	-1.0
	destruction	0.75	-0.81	-0.09	0.50	0.51	0.00	1.65	-1.0
XS - 50 km^2	onset	-0.74	1.60	0.96	0.29	-0.02	-0.00	-2.56	-1.0
	maintenance	-0.15	3.82	-2.29	0.58	-1.17	-0.00	-0.09	-1.0
	destruction	0.88	-1.50	-1.48	1.56	-0.85	0.00	4.16	-1.0

at the mesoscale (i.e., <15%), but can account for around 50% of the respiration in the submesoscale. At very small scales(50 km^2), the character of the balance is chaotic and responds to local events, which may be induced by interactions among bathymetry and fronts induced by dynamic instabilities.

2.4 Discussion

2.4.1 Evidence for a non-continuous dynamic hypoxic region

In semi-enclosed regions experimenting hypoxia, like the Chesapeake Bay, the main variability in horizontal scales presents along the main axis of the bay (Scully, 2016). In such conditions, water column respiration has been found to be the main driving mechanism for interannual variability (Li et al., 2015, 2016), and thus management and action plans can benefit strongly from direct relations, like those among the nutrient load and hypoxic volume (Testa et al., 2017). In contrast, the Texas-Louisiana shelf is exposed to a complex hydrodynamic field where the Mississipi-Atchafalaya originated buoyant plume is populated by baroclinic instabilities that are abundant in summer, with relevant length scales in both cross- and long-shore directions. Our simulations suggest that the complexity introduced by fronts and instabilities affects the distribution of bottom hypoxia (Fig.2.1). High-resolution observations (Fig.2.3) provide supporting evidence.

High-resolution simulations also provide a glimpse into the vertical structure of hypoxia. The thickness of the simulated hypoxic layer is generally contained within 10 m of the bottom, which agrees with literature (Bianchi et al., 2010b; Wiseman et al., 1997), and recent observations (Fig.2.3, DiMarco and Zimmerle, 2017)). In a comparative modeling study, Fennel et al. (2016) determined that a proper resolution of the BBL is a key factor for a more realistic simulation of the hypoxic extent. In this study, while most of the simulated hypoxia was bound to the BBL, the model reproduced localized uplifting of the BBL, and low DO intrusions into the mid water column similar to those seen in observations (see Fig.2.3). This is consistent with idealized model simulations from Zhang and Hetland (2018), demonstrating that eddy transport induced convergence is responsible for the formation of bottom tracer intrusions. In our realistic simulation, this type of intrusion also

occurs on the shelf as a result of interactions between stratification and bathymetry (see Figs. 2.2 and 2.3).

The Texas-Louisiana shelf contains circulation features that span many temporal and spatial scales (Nowlin et al., 2005). However, the internal variability of hypoxia in this region is poorly understood, and the only attempt to investigate sub-mesoscale patterns in hypoxia from observations West of the Mississippi is that of DiMarco et al. (2010). In their study, a mechanism of bathymetric control over the buoyant flow is proposed to explain the isolation of low DO pockets, with an associated wavelength of 50 km or less, found along the 20m isobath in front of Atchafalaya Bay (seen on our study region, Fig.2.1, but East of the larger domain). Given the length scale of their observations, they argued that, while the yearly monitoring cruise measurements could be used to asses the relative change of hypoxia with respect to the long-term mean, higher resolution sampling in both space and time was required to understand the impact of managerial implementations in the development of hypoxia.

While bathymetry may play some roll in the shaping of hypoxia, the structure of the stratification on the shelf is another relevant process to be considered. Hetland and DiMarco (2012), in a validation study of a model for the region, discussed the abundance of small-scale energetic features. The model in their study had a coarser spatial resolution than the one used here but reproduced the statistical variability of the region well. Their findings made them suggest that the small-scale features shown by DiMarco et al. (2010), would be found not only related to the three shallow banks linked to their study but ubiquitously spread in the shelf. They hypothesized that high-resolution sampling techniques would be able to capture features in this spatial scale everywhere on the shelf.

The observations published in the MCT Atlas (DiMarco and Zimmerle, 2017) endorse their hypothesis, and that both stratification and bathymetry affect the distribution of bottom DO. The effect of bathymetry on shaping hypoxic patches has been captured further down-coast from Atchafalaya Bay (Fig.2.3). Our simulations suggest bathymetric trapping occurs not only along coastal shoals but across the shelf, where the presence of ridges can impact the time of exposure to

hypoxia (Fig.2.5).

The existence of some semi-permanent structure to the spatial distribution of hypoxia is worth exploring through observations. Defining some sort of natural boundaries for focal areas of monitoring can be very beneficial to investigate the effect of nutrient limitation policies, and the ecological impacts of hypoxia (Bianchi et al., 2010a).

The elucidation of the dynamical mechanism of such trapping exceeds the scope of this study and will be investigated independently. However, a long term relationship (i.e., monthly averaged values) between exposure and BBL thickness is apparent from our results. Locally, the presence of ridges in the bathymetry is associated with filaments of an extremely thin BBL and weak stratification (Fig.2.5). More broadly across the shelf, the relationship is not as strong but still significant. Fig.2.10 summarizes the mean relationship: longer time of exposure to hypoxia is associated with a thinner (and therefore more stagnant) BBL and stronger stratification. SOD is the dominant sink of the DO budget in the long term and is largely controlled by the mean stratification distribution. These results allow us to hypothesize that bathymetry and stratification impact the development of the bottom boundary layer and, in the long term, can be responsible for some of the structure of the more persistent exposure to hypoxia.

In contrast to these findings, literature often addresses hypoxia as a continuous and relatively persistent process (Rabalais et al., 2001c, 2010; Turner and Rabalais, 2019) moving slowly westwards. Our study doesn't provide evidence for a consistent along shore influx of low DO waters into the far-field. On the contrary, during the period of rapid growth of the hypoxic extent (onset) the mean horizontal flux $\langle u \rangle \langle o \rangle$ is positive across all spatial scales (see Table 2.2).

Moreover, the development of the hypoxic region is not only complex in space but also in time. When integrating spatially, and approaching the problem from a seasonal perspective, we found high variability in the extent even during the most stable month of the season (Fig.2.4). This should be considered carefully because the extent of hypoxia measured in late July is used not only as a yearly assessment, but also to calibrate multiple statistical regression models (Turner et al., 2006; Greene et al., 2009; Forrest et al., 2011; Feng et al., 2012; Scavia et al., 2013; Obenour et al.,

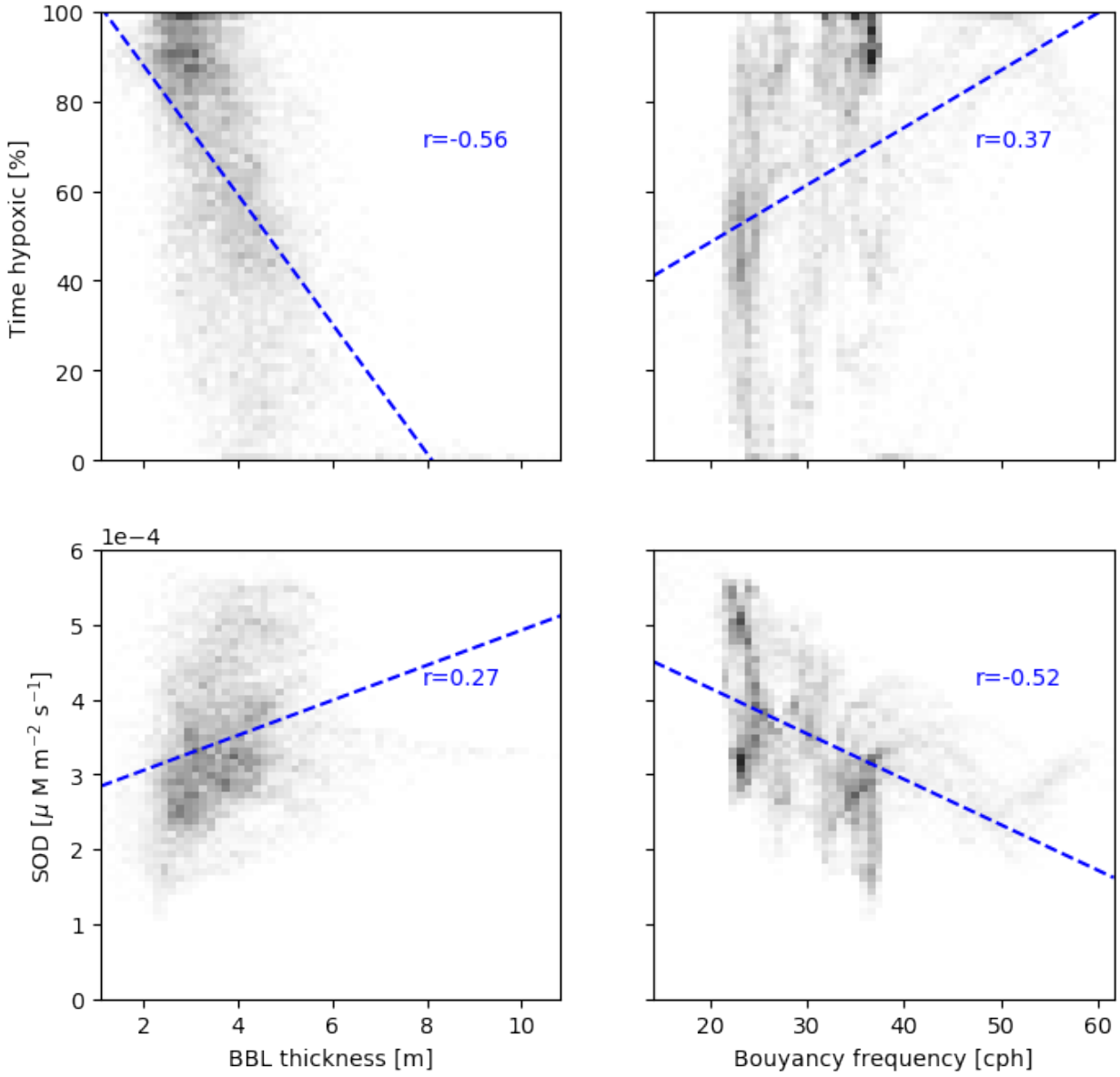

Figure 2.10: Relationship between stratification and hypoxia for August 2010. Top panels show the correlation between local time of exposure and the mean local BBL thickness and mean local buoyancy frequency (N). Bottom panels show the same relationships for the mean local sediment oxygen demand. All correlations (p-value $\ll$ 0,001) were calculated for every grid point in the region of interest (Fig.2.1), constrained between 12 and 50 m.

2015) and to validate coupled and uncoupled hydrodynamic models Fennel et al. (2013); Feng et al. (2014); Yu et al. (2015b); Fennel et al. (2016).

As a consequence, managerial responses can be inaccurate or skewed because there is no statistical evidence linking this space-time composite to the actual maximum, duration, or impact of shelf-wide hypoxia (see discussion in Bianchi et al., 2010b). For example, the peak areal extent is not always simulated during the end of July - beginning of August by our model (see Fig.2.4). For the year presented here, the extent peaked three times, reaching the largest area by the end of August (for simulations of other years, see supplementary information). Additionally, drastic changes can happen in a matter of days, like the areal increase from less than $10^3 km^2$ to more than $15 \times 10^3 km^2$ over a week seen in late August. Hence, we argue that dynamic aspects like the actual duration of the hypoxic season, the rapid variation in the areal extent, added to the complex patchiness previously discussed, should be represented in an assessment of the severity of seasonal hypoxia.

2.4.2 Implications of changes in the budget balance and differences across scales

Decomposing the DO dynamics in the budget components has revealed the dominance of the different terms across spatial and temporal scales. Spatially, some mean structure is apparent, where bathymetry and stratification act as molding mechanisms to control the effect of net advection of DO and bottom respiration (see Figs. 2.5 and 2.6). In time, it has revealed a strong convergence-divergence component at an inertial frequency across all scales, and a subinertial signal at the mesoscale spatial resolution (see Figs. 2.7 and 2.9).

From a temporal perspective, the idea that inertial motions can be relevant in bottom oxygen dynamics in the northern Gulf of Mexico hasn't been explored, even though this signal has been previously captured by continuous measurements at near bottom stations (e.g., Wiseman et al., 1997; Rabalais et al., 1994, 2001a, 2007; Bianchi et al., 2010b). While DiMarco et al. (2010) approached the question of the possible effect of inertial oscillations on the formation of the low oxygen wave-like features found in the study, it was discussed from the perspective of ventilation and deemed not significant. Here, we suggest that the main effect of the near-inertial waves is that

of an oscillatory advection (Fig.2.7), and not mixing. This effect could not be observed by DiMarco et al. (2010) as it would have required continuous sampling for at least two inertial periods.

At sub-inertial temporal scales, the effect of advection is drastically reduced (Fig. 2.9). In all mesoscale budgets, only the weather band remains, shown as spurious episodic events with sudden increases in rate and advection. It is generally accepted that the seasonal development of hypoxia is largely dependent on upwelling favorable winds (Feng et al., 2012, 2014). Feng et al. (2014) proposed a conceptual model with 3 possible stages to explain how wind influences the evolution of the hypoxic area by changing the distribution of stratification and chlorophyll. In this simplified concept, downwelling favorable winds transition to upwelling favorable winds over the summer. However, short inversions of upwelling favorable towards downwelling favorable winds can occur, and these occurrences modify the DO balance, creating sudden decreases in the hypoxic extent (see Fig. 2.4).

Sub-inertial oscillatory motions remain relevant in the sub-mesoscale domains, although reduced in magnitude. The presence of instabilities modulates the local bottom DO dynamics, inducing upwelling and downwelling motions through bottom convergence and divergence respectively (Zhang and Hetland, 2018). In our model results, submesoscale convergence and divergence constantly appear during the 3 months of hypoxia explored, and in the time filtered budget of all submesoscale domains.

The large increase in variability at smaller spatial and temporal scales, seen in the increase of the magnitude of the oscillations in all fluxes but SOD, points towards the importance of submesoscale features (i.e., eddies) in shaping the distribution of DO near the bottom. Fig. 2.11 summarizes this, by showing that variability in the rate of change can increase by more than one order of magnitude from long term averaged (i.e., 15 days) mesoscale to instant (hourly) submesoscale. Most of this variability is driven by advection, even when removing the dominant near-inertial motions (i.e., daily filters and longer).

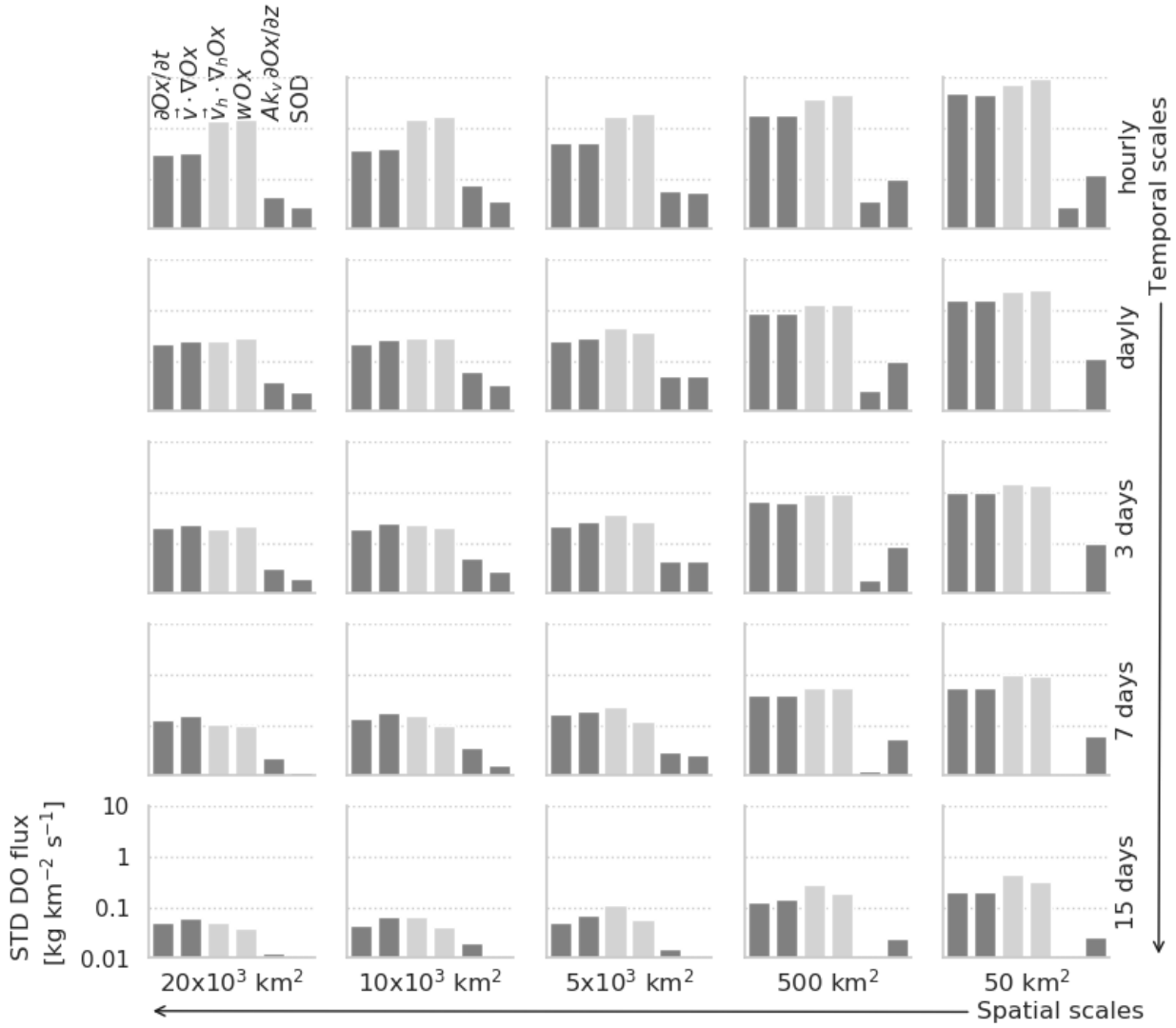

Figure 2.11: Standard deviation of budget fluxes averaged across all combinations of temporal and spatial scales. Magnitudes are plotted in a log scale for DO rate of change, total net advection, separated components of horizontal and vertical net advection (in lighter color), top diffusion, and sediment oxygen demand.

2.4.3 Eddy perturbations

The Mississippi river plume generates a field rich in instabilities due to the relaxation of wind forcing in summer (Hetland, 2017). While we haven't established a direct correlation between surface and bottom features (e.g., direct correlations between surface salinity and bottom oxygen), an indirect relationship is apparent in the large contribution of sub-inertial advection to the DO budget balance.

This assessment is supported by the perturbation component when decomposing the advective flux, as shown in Table 2.2. Horizontal perturbations are negligible at mesoscale, as instabilities are expected to cancel out inside the domains, but are large in the submesoscale. However, these horizontal motions generate vertical perturbations that add up across all spatial scales. Through this cumulative effect, the vertical perturbation flux is the dominant component of the DO balance, especially at large scales. At very small scales, vertical and lateral fluxes are both strong, and local bathymetry affects the character of the balance.

The vertical perturbation component manifests itself in the form of low DO intrusions in the mid water column, and the compensating downward flow of oxygenated waters generating large anomalies. This ventilation effect accounted for more that 100% of the respiration during the maintenance stage at both mesoscale and sub-mesoscale (except in the 50 km^2), and could be in the order of 200% during the destruction stage and up to ~400%.

An important reflection on the processes discussed in this study is that the distribution of other tracers (e.g., nutrients, CO_2, trace metals) at the bottom water column in the shelf, at least at depths shallower than 50 m, would also be subject to modulation by the submesoscale instability field. A natural connection is to expect an ecological response to the distribution of said bottom tracers, including oxygen, and particularly to the intrusions into the mid water column generated by these processes.

2.5 Conclusions

The development of hypoxia in the far-field of the Mississippi plume is subject to processes with spatial scales ranging from $\mathcal{O}$(10km) to $\mathcal{O}$(100km), and temporal scales ranging from the near-inertial period to seasonality. The spatial distribution of low DO waters takes the form of eddy-like features enclosing oxygenated cores. In cross-sections, this can appear as isolated low DO pockets, suggesting that the features observed by DiMarco et al. (2010) are ubiquitous on the far-field shelf. High-resolution observations in the region support this hypothesis.

Decomposing the DO budget allows us to quantify the effect of the individual driving mechanisms. Long term (monthly) effects can be observed in the time of exposure to hypoxia and the mean rate of change. The distribution of both fields reveals more permanent oxygenation-core features. The monthly mean budget shows the main balance to be between bottom respiration and net advection.

Variability in advection increases with decreasing temporal and spatial scales by more than an order of magnitude. The large variability associated with the submesoscale is consistent with a field rich in instabilities introducing small scale but strong advection anomalies. Separating the perturbation component from the main flow allowed to identify the vertical turbulent flux ($\langle w'o' \rangle_T$) as the main contributor to counter the effect of the bottom respiration during the maintenance and destruction stages of hypoxia. This is consistent with the presence of bottom water intrusions, such as those seen in high-resolution observations and features simulated in idealized models (Zhang and Hetland, 2018).

2.6 Acknowledgments

This chapter is based on an article submited to the Journal of Geophysical Research - Oceans, co-authored by Professor Robert Hetland. This research was made possible in part by a grant from The Gulf of Mexico Research Initiative, and in part by NOAA through the Coastal Ocean Modeling Testbed (COMT) project. Model data are publicly available through the Gulf of Mexico Research Initiative Information & Data Cooperative (GRIIDC) at https://data.gulfresearchinitiative.org (doi:

[10.7266/N7VH5KSK, 10.7266/N70000JK]), and animations of the simulations can be found at the Texas Automated Buoy System website (http://pong.tamu.edu/tabswebsite/subpages/gallery.php?gallery=oxygen). Observational data was obtained from the Mechanisms Controlling Hypoxia (MCH) program (http://hypoxia.tamu.edu/) funded by the NOAA CSCOR grant NA06N0S4780198.

3. THE STRUCTURE AND CHARACTER OF EXPOSURE TO HYPOXIA IN THE TEXAS-LOUISIANA SHELF

3.1 Introduction

The severity of the seasonal bottom hypoxia that develops in the Texas-Louisiana (TX-LA) shelf is mainly quantified by the mid-summer estimate of hipoxic area from shipboard observation mapping efforts (Dale et al., 2008; Rabalais and Turner, 2001; Bianchi et al., 2010b). This metric is used to assess the inter-annual trend and draw correlations for managerial purposes (Scavia et al., 2003, 2013, e.g.). However, the TX-LA shelf is a highly variable environment. The seasonal pattern in the physical properties of the shelf (e.g., circulation and stratification) is modulated inter-annually by changes in both the prevailing winds and in the freshwater discharge from the Mississippi-Atchafalaya River system (Cochrane and Kelly, 1986; Li et al., 1996; Nowlin et al., 2005). At small scales, abundant baroclinic instabilities develop during summer due to the widening of the river plume and the relaxation in the wind (Hetland, 2017). Given the shelf dynamism, the variability observed in the surface is expected to propagate to the bottom through the occasional mixing of the water column by tropical storms, and the interaction of baroclinic eddies with the shelf bottom (DiMarco et al., 2010; Qu and Hetland, 2020; Zhang and Hetland, 2018). This variability, which can be of the same order of magnitude as the seasonal variability, will impact the descriptive capability of time constricted mapping efforts.

In an idealized study simulating the general conditions of the TX-LA shelf Zhang and Hetland (2018) demonstrated that instabilities induce bottom convergence through buoyancy transport. Through observations, DiMarco et al. (2010) related the scales of variability of hypoxic water pockets to those of surface freshwater meanders.

This work presents two alternative metrics to categorize the severity of hypoxia for retrospective studies that should consider time and spatial structure: time-averaged area and local exposure to hypoxia. By analyzing 23 years of a hindcast model of the region, we attempt to draw gen-

eral patterns from the structure and variability of the bottom oxygen concentration and relate it to the interaction between topography and low oxygen intrusions due to convergence induced by baroclinic instabilities.

We argue that because hypoxia is an ecosystem problem, metrics that take into account variability in space and time would be more beneficial for understanding and evaluating organismal response to the seasonal event.

3.2 Methods

3.2.1 Realistic model

The TXLA model discussed in Chapter 2 is used again here. The entire domain of the model and the region of interest (ROI) for this study is shown in Fig.3.1. Simulations in the ROI from 1993 to 2017 are used to investigate exposure to hypoxia.

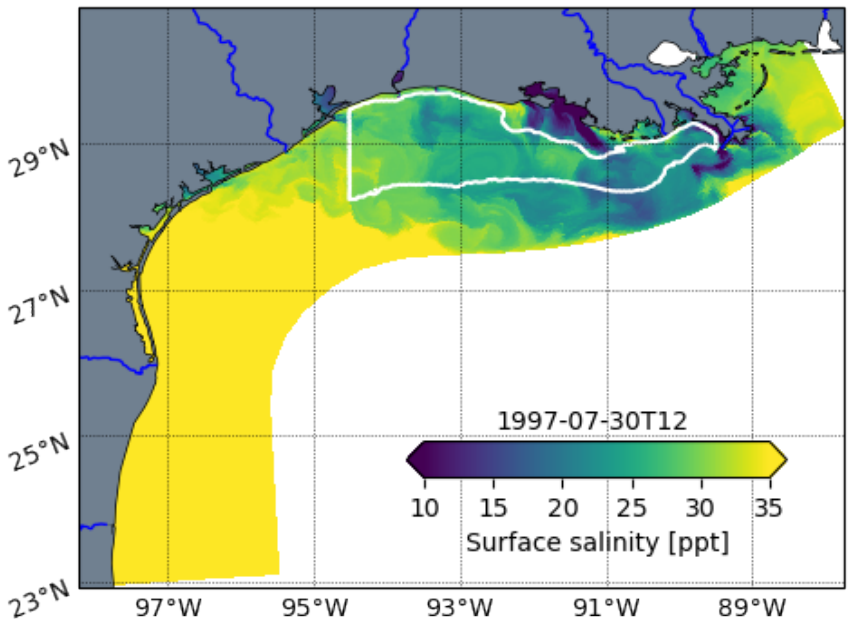

Figure 3.1: TXLA model domain displaying a surface salinity snapshot during in summer 1997, the year of the most severe simulated hypoxia. White line delineates the region of interest (ROI) covering the area typically sampled by the LUMCON mid-summer annual survey.

To calculate hypoxic extent, the model domain was limited to the region that is typically sampled by the LUMCON cruise (between 94.5°W and 89.5°W zonally, and the 10 and 50 m isobaths), and hypoxia is defined when bottom DO concentration is equal or below 60 μM. The time-weighted average of the hypoxic extent is calculated over an entire year as a measure of severity.

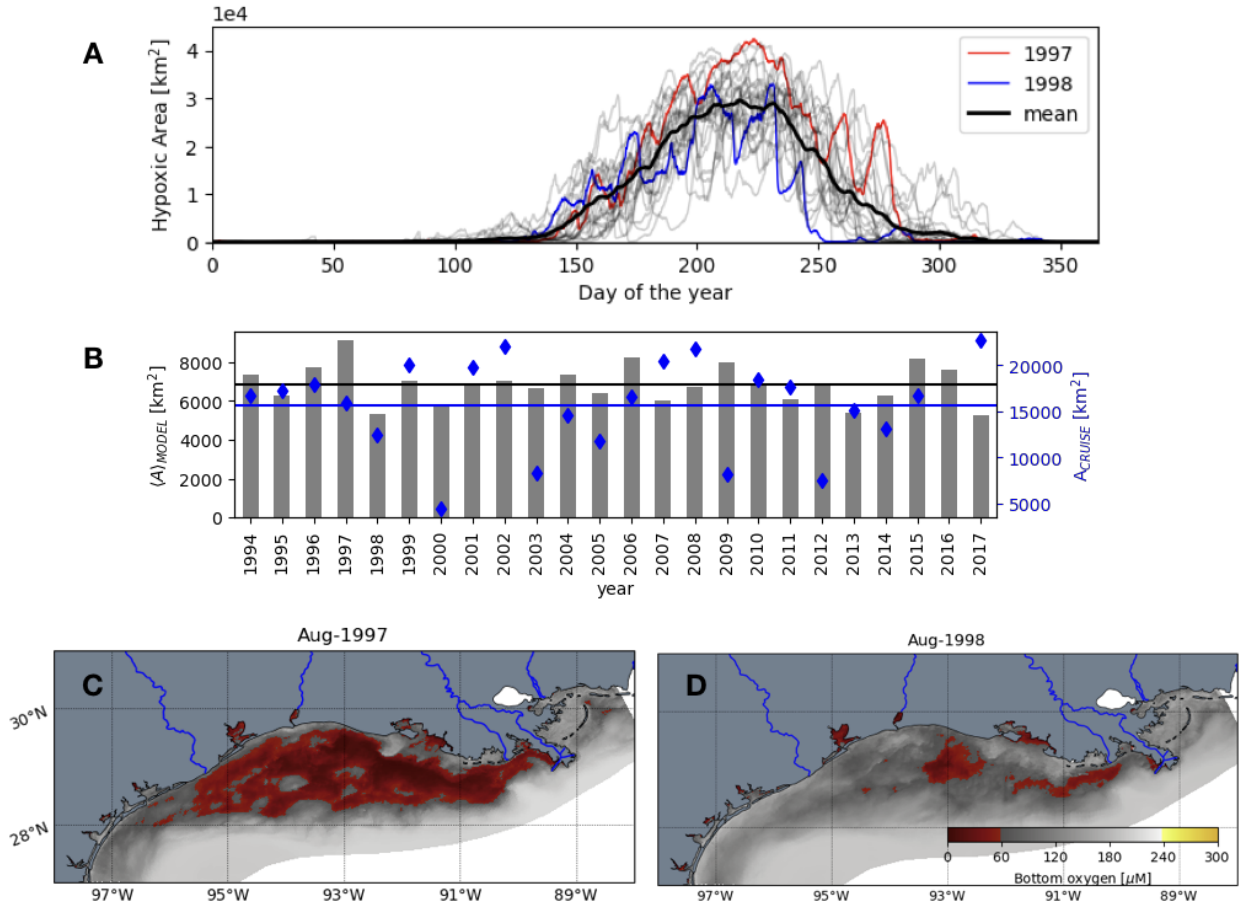

Figure 3.2: TXLA model bottom oxygen simulations. A). Time series of hypoxic extent simulated for years 1994 to 2017. The most severe (1997) and the weakest (1998) year in terms of areal extent of hypoxia are highlighted in red and blue respectively. The black line is the daily climatology mean. B). Time weighted average of simulated hypoxic extent for each year $\left(\langle A \rangle = \int A_t \, dt \,/\, \int dt\right)$, with the inter-annual mean indicated by the black line. For contrast, LUMCON areal estimates are shown as blue diamonds, and the inter-annual mean as the blue line (scales are different). C). and D). are bottom DO monthly average in August for the strongest and weakest year respectively.

3.2.2 Quantifying occurrence

To quantify the occurrence of several events we define a time count function as:

$$\mathcal{E}\left[\mathcal{C}\right] = \frac{\sum_{t=0}^{n} e_t \, dt}{\sum_{dt}}, \tag{3.1}$$

where $e_t = 1$ if the the condition $\mathcal{C}$ is True and zero otherwise, and dt is the model time-step (1 hour).

To estimate local severity we calculate time of exposure to hypoxia or $H_{\mathcal{E}} = \mathcal{E}\left[\mathcal{C}\right]$, when $\mathcal{C} : DO_t \leq 60.0\,\mu M$.

As evidence in Chapter 2 strengthens the hypothesis that vertical processes are dominant in the rate of change of bottom DO, we attempt to relate exposure to hypoxia, $H_{\mathcal{E}}$, to uplifting of low DO water into the mid-water column. Thus, we quantify the occurrence of low DO intrusions in a similar manner, as $I_{\mathcal{E}} = \mathcal{E}\left[\mathcal{C}\right]$, when low DO intrusions occur, or $\mathcal{C} : \frac{d}{dz}DO(z) \leq -3 \times 10^{-3}$ [μ M $\cdot$ m^{-1}] for any depth z above the bottom boundary layer. This threshold value is chosen somewhat arbitrarily from exploring point DO profiles, such that the vertical gradient of DO is negative (i.e., low oxygen water sitting on top of more oxygenated water), and the magnitude is large enough to be a significant change in the profile. An example of an intrusion and a sample profile is shown in Fig. 3.3.

3.3 Results

The large inter-annual variability in the hypoxic extent and the region of exposure is exemplified in Fig.3.2. The extent of the region affected by hypoxia changes rapidly and can have different responses, as seen in Fig.3.2.A. The hypoxic area maximum is often simulated later than mid-summer (i.e., climatology maximum is around the second half of August, ~220 DOY). Some years exhibit several hypoxic breakage and regrowth episodes (i.e., 2003, 2010, 2012. See Chapter 2, Fig.2.4 for detail on 2010).

A time-weighted average of the hypoxic area over a year is used as a measure of year-long severity to include both temporal and spatial impact (Fig.3.2.B). Although not comparable in

scale, contrasting time-weighted averages to mid-summer estimates shows how the estimate's inter-annual trend can be misleading due to an episodically timed cruise. For instance, the largest cruise estimated area in the registry by now is 2017, but this year ranks well below the average in the time-weighted estimate. Most cruise estimates that fall high above the inter-annual mean, are either below or close to the mean in the time-weighted estimate.

In space, the distribution of mean bottom DO (i.e., August mean) can change drastically from year to year (Fig.3.2.C), but even when the hypoxic region is extensive covering the entire shelf, some structure can be observed in the presence of strongly ventilated pockets.

Local exposure to hypoxia allows usto evaluate severity in time and space. Fig.3.4 shows exposure time for the most severe (1997) and the weakest (1998) year affected by hypoxia, in contrast to the 24-year climatology (see Fig.2.5 for August 2010 as an additional example). Although the difference between years is significant, some common patterns emerge, which can be related to bathymetric features hinted in Chapter 2 and the general shape of the shelf. These observations show that hypoxia occurs every year on the upper shelf east of about 93°W (where the shelf is narrow), but also in localized regions to the west, where bathymetric gradients shape it (see climatology and weak year).

On the narrow end of the shelf (East of 93°W) exposure is high, but variability is small in the shallower portion, and large offshore (where the slope is steeper). On the west side, there is a shallow bank that exhibits relatively high variability. This bank is separated by a filament corresponding to a strong gradient in the climatology, with high exposure, and low variability. At least one pocket of low exposure and low variability can be observed between the shallow eastern region and the bank on the west. The eastern side of the pocket is collocated with another ridge, deeper than the ridge separating the bank on the west. We hypothesize that this collocating effect is a response to bathymetric trapping of bottom water between ridges, which would result in stiller waters exposed longer to bottom respiration.

An example of a high horizontal gradient in exposure associated with bathymetric features is shown in Fig.3.5. While it is challenging to relate exposure time quantitatively to bathymetry, the

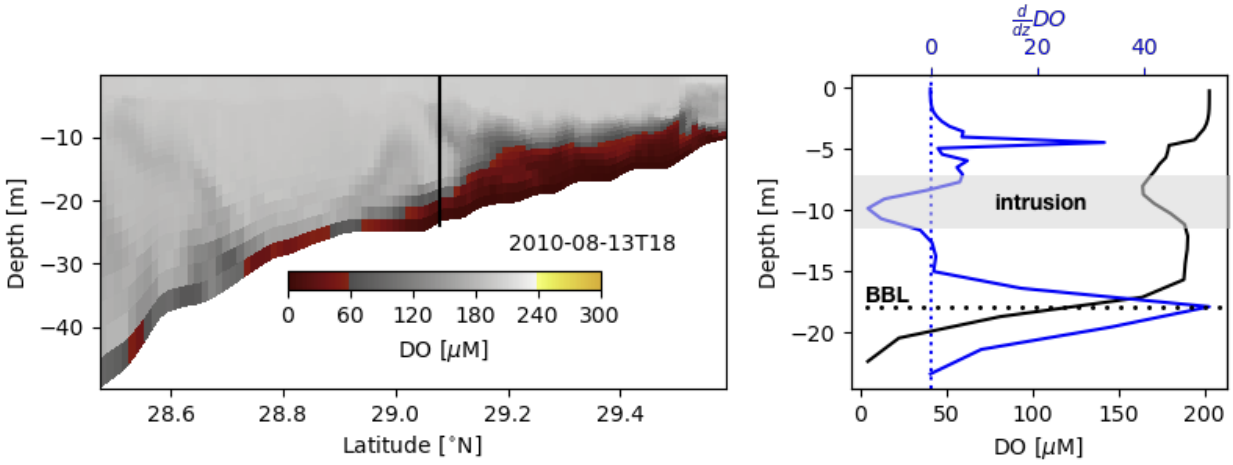

Figure 3.3: Model snapshot displaying DO concentration. Several low DO intrusion can be seen in this cross-section (left). The black line indicates the location of the oxygen profile (right). Operationally, intrusion events are quantified when $\frac{d}{dz}DO(z) \leq -3 \times 10^{-3}$.

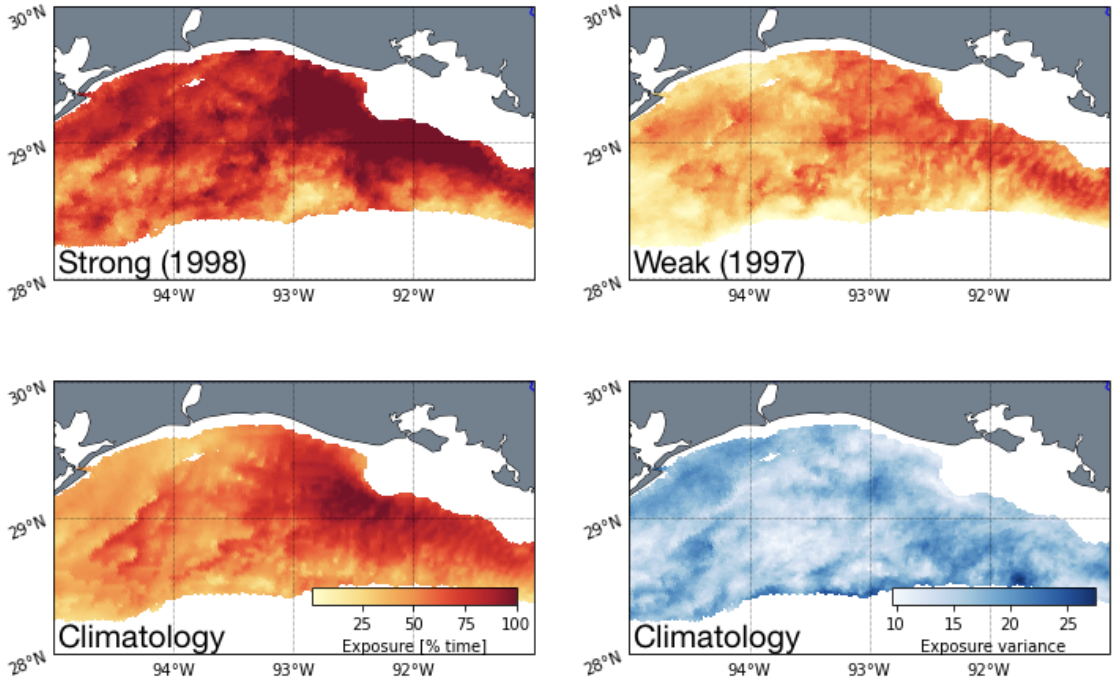

Figure 3.4: Exposure to hypoxia as defined in Eq. 3.1 normalized to summer time (i.e. 92 days is 100%). Top: most severe (1997) and the weakest (1998) simulated hypoxia. Bottom: Climatology mean and standard deviation for the 1994-2017 period.

large gradient in time of exposure demonstrates a certain trapping effect. A correlation is found between the amplitude of the horizontal gradients in both bathymetry and exposure.

Fig.3.6 displays cross-sections of exposure. This view allows us to localize where hypoxic water is uplifted frequently and how it is related to bathymetry. Uplifting is ubiquitous on the shelf, but it is episodic. Contrasting the two transects (cs 1 and cs 2), it is evident that uplifting intensifies around quirks in the bathymetry, and that exposure is intense in channels indicating the trapping effect (i.e., cs 1).

Furthermore, we can relate exposure time to vertical ventilation through the presence of low oxygen intrusions. The occurrence of intrusions expressed in time percentage ($I_{\mathcal{E}}$) was quantified for each year and were found to appear primarily deeper than the 20 m isobath. Fig.3.7 shows the occurrence of intrusions for the same instances as in Fig.3.4, where intrusions are calculated as hypoxic (top) or total (bottom). For the most severe year, intrusions are suppressed on the shallower shelf and are strong on the outer shelf, past the 20 m isobath. More frequent intrusions are also collocated with pockets of low exposure. For the weakest year, a quiet region in the mid-shelf is surrounded by continuous intrusions in the inner and outer shelf. In the climatology, intrusions are a common occurrence where the shelf is narrow and they extend in the steeper outer side of the wider part of the shelf (West of 93°W).

We could not find a direct point to point correlations between surface properties (e.g., salinity, vorticity, horizontal stratification) and bottom oxygen, exposure, or occurrence of intrusions. However, we found evidence that more uplifting and intrusions occur when the shelf is rich in instabilities, and therefore bottom waters are more oxygenated. Fig.3.8 shows time-series of area-weighted histograms of bottom DO, surface vorticity and surface salinity for August of the two years used as reference (1997 and 1998). In the plots, darker colors indicate larger areas exposed to the corresponding value of the property. For most of the period in 1997, the bottom layer of the shelf had DO concentrations below the hypoxic threshold, and large portions are anoxic (see the dark layer of near-zero values). For 1998, DO concentrations are more widely distributed, with areas of similar extent for concentrations below 150 μM. When examining vorticity, the simulations

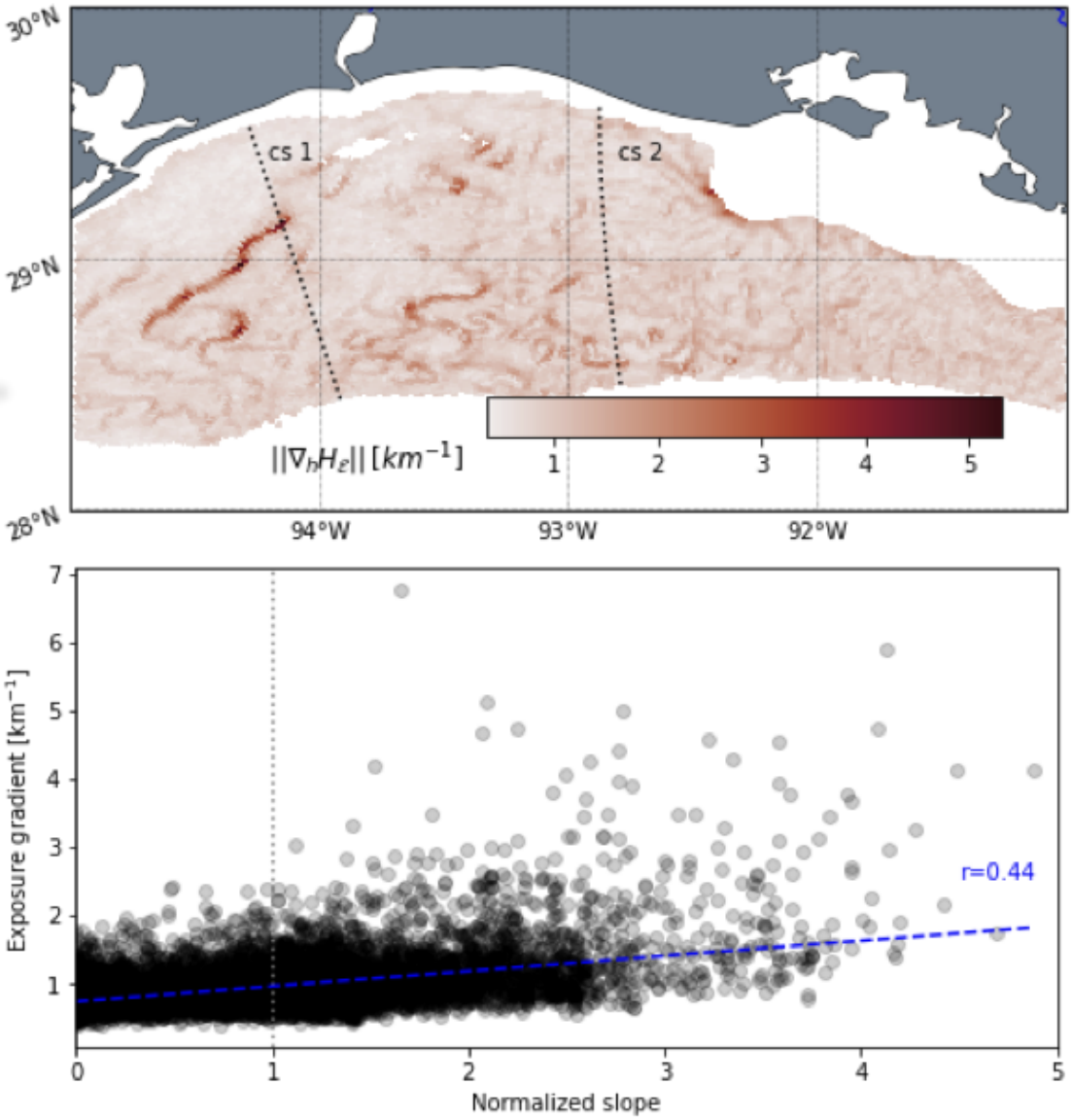

Figure 3.5: Top: Distribution of the amplitude of the horizontal gradient of the climatological mean of exposure ($H_\mathcal{E}$), when time is expressed in percentage. Two transects are shown for the cross-sections in Fig.3.6 Bottom: Amplitude of the horizontal gradient of climatological mean in exposure vs. normalized slope in bathymetry. The normalization is done by the mean slope of the shelf.

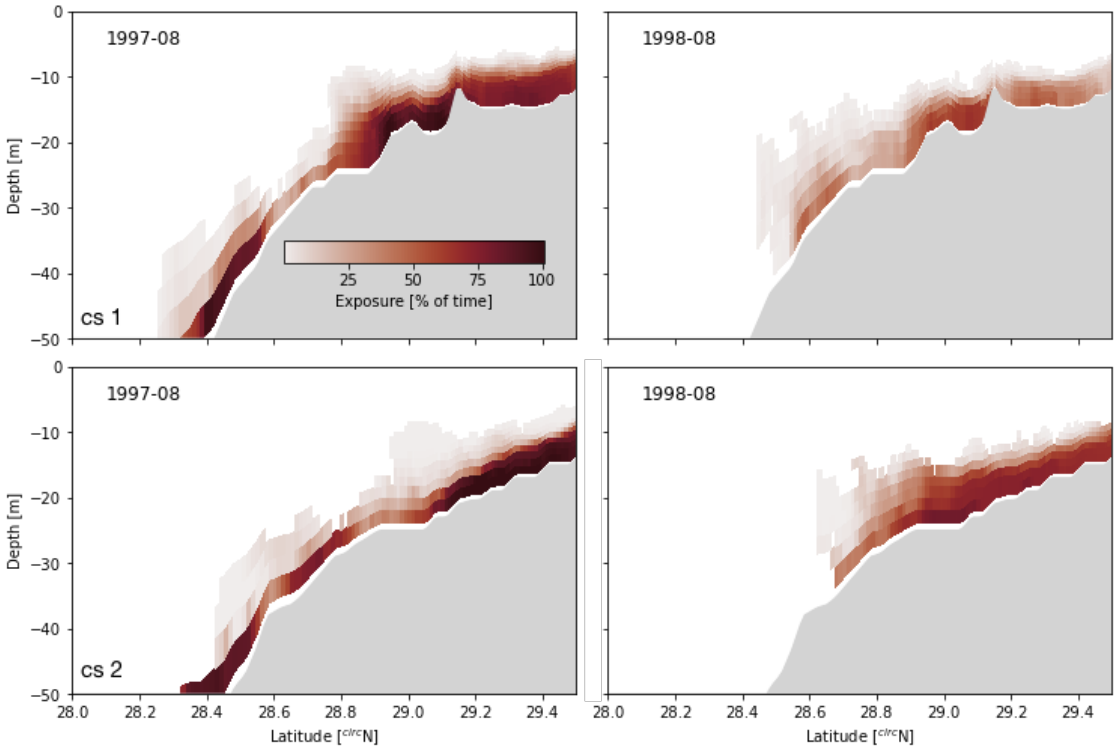

Figure 3.6: Cross sections of exposure for the transects indicated in the top panel of Fig.3.5 (top and bottom), for 1998 and 1997 (left and right).

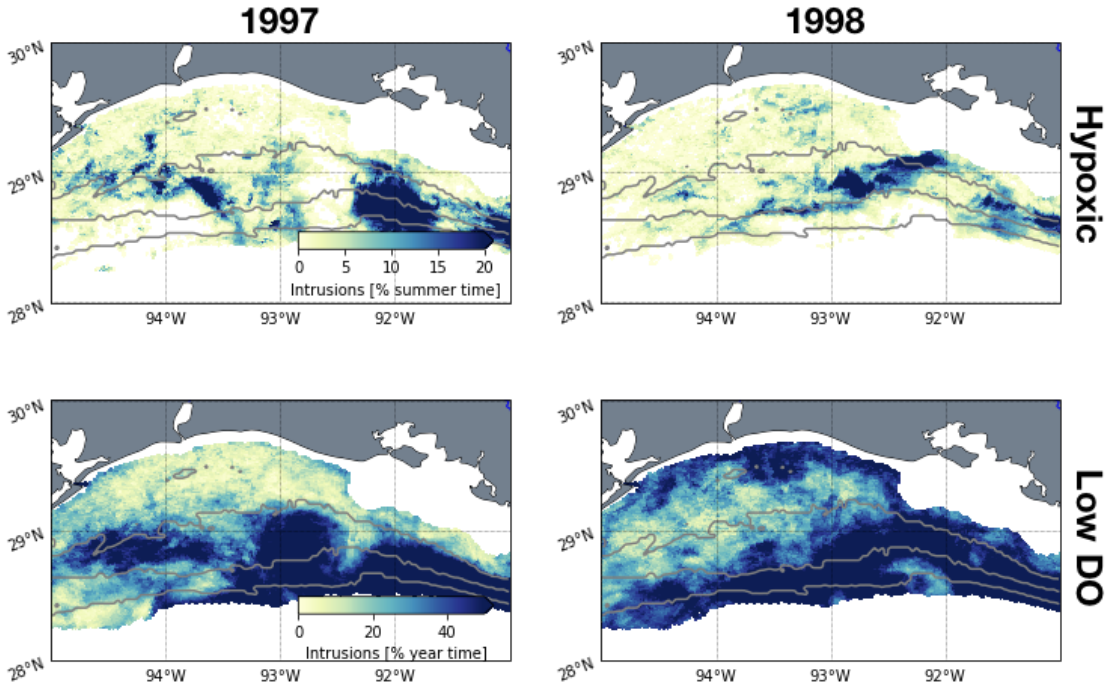

Figure 3.7: Ocurrence of intrusion event in the shelf for the strongest (1997) and weakest (1998) years simulated. The top panels show intrusions of hypoxic water only, and the time is normalized to summer time (i.e. 92 days). The bottom panels show general low DO intrusions which occur all year through and are normalized to year time (i.e. 365 days).

show suppression of baroclinic eddies in the shelf in 1997, indicated by the extensive areas with vorticity values near zero. For 1998, the area with near-zero vorticity is significantly reduced.

It is important to point here that near-zero vorticity, namely, the suppression of eddies, is a response to a reduction in the horizontal density gradients. Two types of reduction of density gradient are seen in the plot. In the first case, for 1997, it is a continuous phenomenon resulting from the large freshwater envelope covering the shelf. In the second case, covering a short period of about three days in 1998, an intense mixing event is caused by a storm. This intense stirring results in the immediate ventilation of the bottom shelf, observed in the sharp increase in the extent of highly oxygenated bottom water.

3.4 Discussion and Conclusions

Hindcast model output from the TXLA implementation for years 1994 till 2017 was used to explore the spatial structure of exposure to hypoxia and its relationship to bottom water uplifting or intrusions.

The most widely used metric to estimate annual hypoxia severity in the northern Gulf of Mexico is the hypoxic extent (Dale et al., 2008). These metrics are obtained by shipboard observations usually performed during summer: either the Louisiana Universities Marine Consortium (LUMCON, https://gulfhypoxia.net/) or the Southeast Area Monitoring and Assessment Program (SEAMAP, https://www.gsmfc.org/seamap.php). Hypoxic area estimates from the model simulations challenge the cruise based annual estimates, by revealing a dynamic extent that can change in an order of magnitude of about $\mathcal{O}(\text{km}^2)$ in a matter of days as a response to weather events (Fig.3.2.A). Furthermore, there is no current metric attempting to estimate the duration of hypoxia over the TX-LA shelf. By integrating the hypoxic extent over time, we can utilize a hindcast metric to better understand the severity of hypoxia for the past years in both the spatial and temporal dimensions. A metric such as the time-averaged area is especially relevant for studies attempting to correlate hypoxic severity to annual fisheries landings such as the one attempted by O'Connor and Whitall (2007) for brown shrimp landings between 1985 and 2004. Similarly, complex economic studies attempting to relate seafood prices to hypoxic severity could improve their analysis (e.g.,

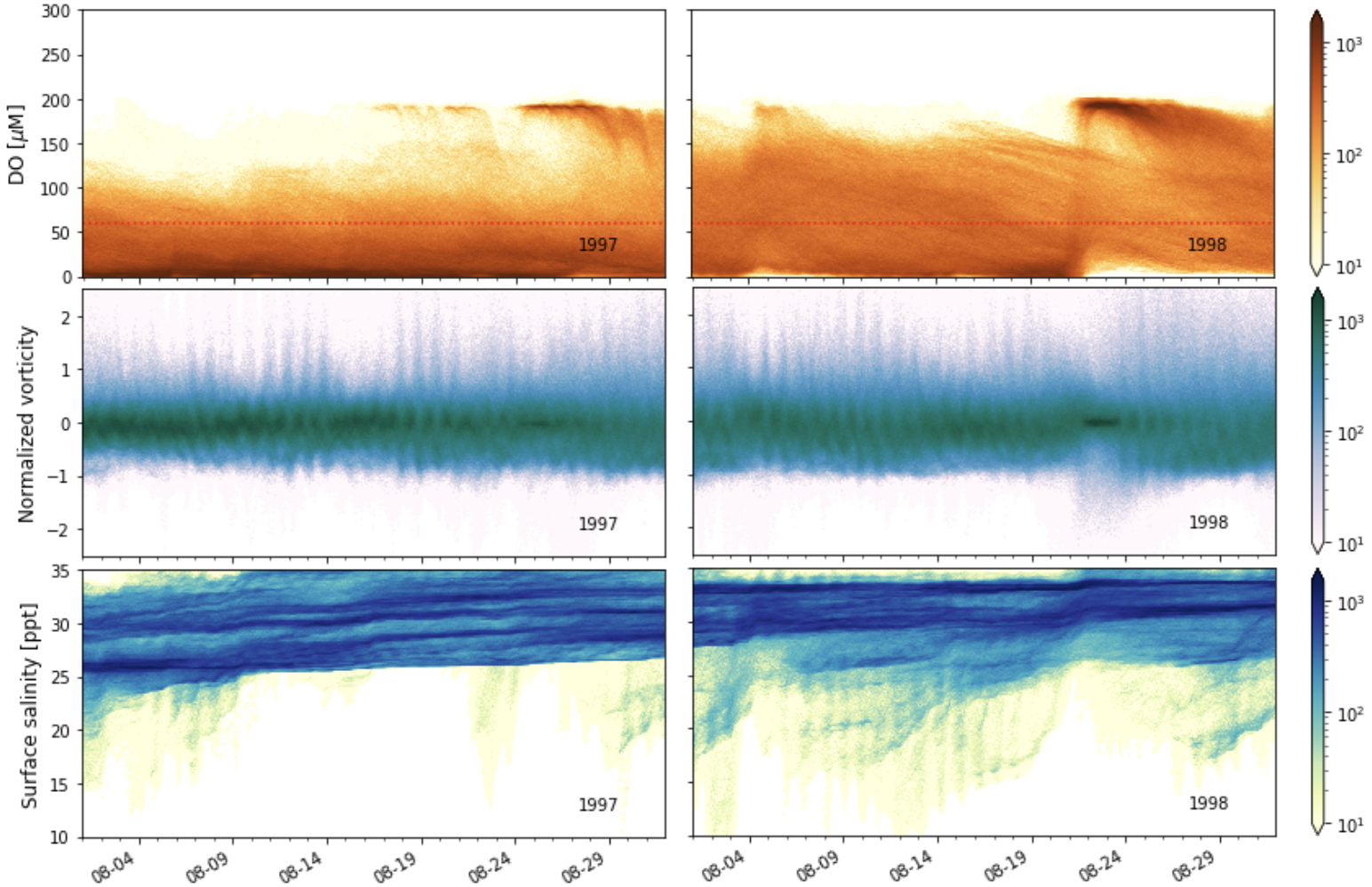

Figure 3.8: Property histograms weighted by area (color in km^2) for the distribution of bottom oxygen (top), normalized surface vorticity (middle) and surface salinity (bottom) during the month of August in 1997 and 1998. The red dashed line in the DO plots indicate the hypoxic threshold. Large areas with vorticity values close to zero indicate the suppression of eddies.

see Smith et al. (2017)) by utilizing hindcasts products in time.

We calculated exposure to hypoxia as a metric to investigate the structure of severity in space over the 23 years of hindcast. The most and least severe years are presented for comparison, along with an inter-annual mean and variance. By exploring general trends in the spatial structure, and the variability, we can draw some generalizations for different sections of the TX-LA shelf. For instance, there is an evident difference between the narrow portion of the shelf (East of 93.5° W) and the wider portion (Fig.3.4). While the narrow portion appears to be highly impacted every year, it appears to be a somewhat continuous region. The western section presents a complex small scale structure, and some of it appears to be related to features in the bathymetry like channels and ridges. Climatology exposure, compared to the frequency of hypoxia maps from LUMCON (e.g. see Dale et al. (2008) and https://gulfhypoxia.net/research/shelfwide-cruises/frequency-of-hypoxia/), shows a morphology dependent on topography while the latter is strongly shaped by interpolation artifacts.

The relationship between the fine spatial structure in exposure and bathymetry is substantiated by the strong horizontal gradients found in the field and a correlation with changes in slope (Fig.3.5), and cross-sections of exposure (Fig.3.6). This model results agree with the high-resolution observations in the region: the vertical sections collected in DiMarco and Zimmerle (2017) display a complex morphology in the distribution of dissolved oxygen at the bottom. There are multiple instances in which hypoxic water contained by the pycnocline is uplifted by some bathymetric quirk (e.g., see profiles in Fig.2.3).

DiMarco et al. (2010) discussed the importance of bathymetric trapping in the formation of hypoxic pockets; however, the transect analyzed in their study followed the 20 m isobath relatively close to the coast. Their study suggests that hypoxic pockets with a length-scale smaller than 50 km observed along-shelf out of the coast of Louisiana are a mechanistic response to dynamic instabilities. No further exploration of this kind of structure has been done on the shelf interior, but our model simulations hint towards them as common features.

Dynamic instabilities are very energetic in the TX-LA shelf during summer due to strong hor-

izontal density gradients (Hetland, 2017; Qu and Hetland, 2020). Using an idealized numerical model Zhang and Hetland (2018) found that baroclinic eddies generate buoyancy transport in response to bottom convergence due to interaction with a sloping bottom. This convergence creates uplifting of bottom waters. The idealized simulations generated multiple localized convergent zones with a transient nature. In our realistic model, intrusions, or the uplifting of low oxygen waters from the bottom, are ubiquitous and transient features in the interior of the shelf (see Figs. 3.6 and 3.3). Some of these intrusion regions appear to be related to the general bottom slope, while small-scale localized features involve interactions with more complicated bathymetry.

Because vertical flux of oxygenated surface water is the primary mechanism of bottom water ventilation, the presence of intrusions affects considerably the oxygen budget at the bottom. Consistently, years with a large river discharge resulting in an extended freshwater envelope, but with suppressed eddy activity develop severe hypoxia (e.g., 1997), while years with energetic eddies populating the surface develop a much smaller hypoxic region (Fig.3.8).

An additional consideration to the uplifting of low DO waters through eddy induced bottom convergence is that this effect should affect the distribution and uplifting of other tracers (e.g., nutrients, tracer metals, etc.) as well as sediment resuspension. Sediment resuspension and nutrient uplifting will also alter the biogeochemistry of the water column, and will most likely increase water column respiration (for a review of this effect in the mesoscale see Mahadevan (2014)). These factors are not considered in our study and should be recognized.

In the same manner that an area metric that considers time would be a better tool to evaluate the impact of severity to the biota in the long term, we should consider that the three-dimensional structure of hypoxia, and the variance, are what is of ecological relevance to the organisms in the shelf (Zhang et al., 2009, e.g., see). Exposure to hypoxia can be one such metric, but more observational studies are required to contrast the patterns simulated by the TXLA implementation.

3.5 Acknowledgments

This chapter is based on a manuscript in preparation, co-authored by Professor Robert Hetland. The support of Dr. Lixin Qu for all code debugging is also gratefully acknowledged. A NOAA

grant supported this study through the Coastal Ocean Modeling Testbed (COMT) project, a grant from The Gulf of Mexico Research Initiative, and a scholarship from the Oceanography Department at Texas A&M University. Model data are publicly available through the Gulf of Mexico Research Initiative Information & Data Cooperative (GRIIDC) at https://data.gulfresearchinitiative.org (doi: [10.7266/N7VH5KSK, 10.7266/N70000JK]), and animations of the simulations can be found at the Texas Automated Buy System website (http://pong.tamu.edu/tabswebsite/subpages/gallery.php?gallery=oxygen).

4. DISSOLVED OXYGEN MODULATION BY BAROCLINIC INSTABILITIES: AN IDEALIZED STUDY ON WIND AND TOPOGRAPHY EFFECTS.

4.1 Introduction

Coastal zones dominated by river plumes are particularly dynamic ecosystems subject to fluctuations in freshwater, sediments, nutrients, and pollutants imported from the continents to the ocean (Horner-Devine et al., 2015). Under the right conditions, coastally trapped river plumes might evolve to form baroclinic instabilities. That is, if the plume is wide enough relative to the local deformation radius, instabilities will grow (Hetland, 2017). This scenario is not a common occurrence but is particularly the case for the Mississippi-Atchafalaya plume along the Texas-Louisiana (TX-LA) shelf. It this environment, the wind relaxation in summer into a weak forcing allows for the freshwater to reach far enough offshore, but with reduced surface mixing (Hetland, 2017; Qu and Hetland, 2020).

Submesoscale eddies in the Mississipi-Atchafalaya system are typically observed during summertime in surface chlorophyll satellite observations and the suspended sediment seen in the true-color band (DiMarco et al., 2010; Hetland, 2017; Vastano et al., 1995). Instabilities play an essential role in the transport and redistribution of buoyancy, tracers (such as nutrients), and floating particles (such as plankton), and therefore in the local biogeochemistry (Mahadevan, 2014). Furthermore, the TX-LA shelf is relatively broad and shallow, allowing the instabilities to interact with the bottom enhancing dissipation (Qu and Hetland, 2020), and inducing buoyancy-driven bottom convergence (Zhang and Hetland, 2018).

Submesoscale instabilities are also thought to affect the redistribution of bottom oxygen during the seasonal coastal hypoxia in the TX-LA shelf, either through the redistribution of buoyancy and thus stratification (DiMarco et al., 2010) , or through ventilation (Qu and Hetland, 2020). Bottom oxygen concentrations simulated by a realistic implementation of a hydrodynamic model for the TX-LA shelf, utilizing a simple oxygen parameterization, strongly point towards the eddy induced

vertical turbulent flux as the primary mechanism of hypoxia ventilation in the shelf (see Chapter 2). The complex morphology observed on multiple vertical sections of high resolution dissolved oxygen concentration (see DiMarco and Zimmerle (2017)), also points to a strong interaction between hypoxic patches and buoyancy induced fronts.

This chapter will discuss idealized river plume simulations that evolve in buoyancy-driven instabilities. The same oxygen parameterization used in the realistic TXLA model is applied for these simulations with the aim of establishing a relationship between the formation and growth of eddies and the ventilation of highly respired bottom water. Particularly, wind forcing and the effect of the addition of ridges to a sloping bathymetry are used to evaluate changes in the bottom oxygen concentration shelf-wide and locally.

4.2 Methods

4.2.1 Idealized model

An idealized shelf model was set up following closely the base case implementation of Hetland (2017) . The ROMS/TOMS Framework from the COAWST Modeling System is used as the hydrodynamic model (Warner et al., 2010). ROMS solves free-surface, hydrostatic, primitive equations using orthogonal curvilinear coordinates in the horizontal direction and a terrain following S-coordinate in the vertical direction (Shchepetkin and McWilliams, 2005). For the idealized setup, the parameters used to define the s-coordinate follow the Shchepetkin (2010) UCLA-ROMS function with $V_{transform} = 2,\ V_{stretching} = 4$, and the surface and bottom control parameters ($\theta_S = 5.0,\ \theta_B = 0.4$) are set for increased surface resolution and no bottom amplification. The critical depth is set as $T_{cline} = 5.0$.

The idealized domain is 260 km in the along-shore direction, and 128 km in the across-shore direction. The horizontal resolution is 1 km $\times$ 1 km, and there are 30 terrain following layers in the vertical dimension. The base case has a uniform bottom slope ($\alpha = 10^{-3}$) and added bottom noise such that $h = h_0 + \alpha y + \epsilon$, where h is the distance dependent depth, h_0 is the minimum depth (5 m), y is the cross-shore distance and ϵ is a 1% random noise. Four additional scenarios

where created adding a bump to the slope, using a quadratic formula dependent of the cross-shore direction:

$$bump(y) = \delta h \times \left[\left(\frac{y - D}{w/2} \right)^2 - 1 \right], \; for D - w/2 < y < D + w/2 \tag{4.1}$$

where δh is the height of the bump (5 or 10 m), D the distance from the coast to the middle of the bump (20 or 50 km), and w the width of the bump (10 km). The mean cross-shore bathymetry for the base case and the four bump iterations are shown in Fig.4.1., with a schematic of a bump.

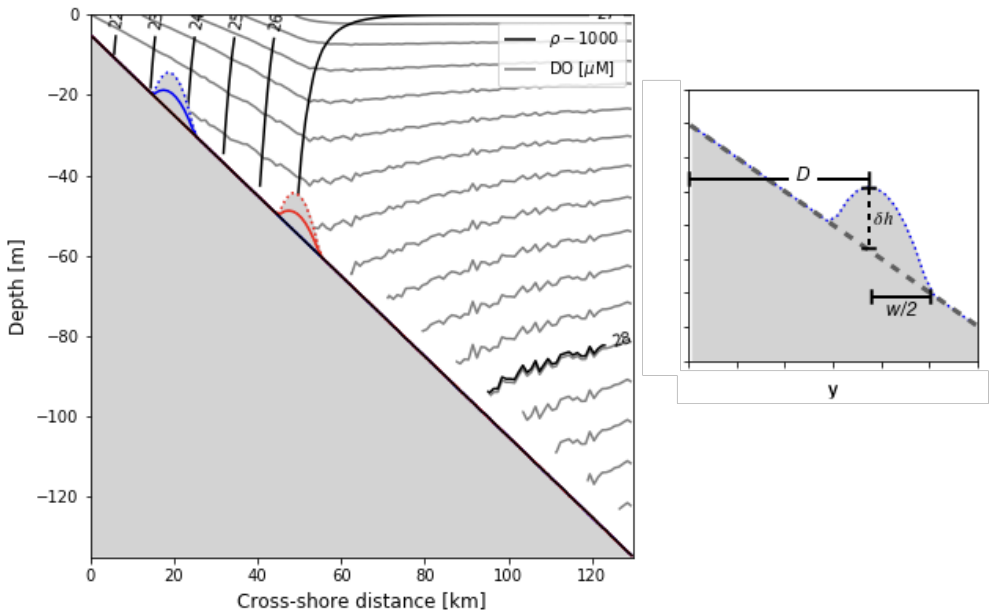

Figure 4.1: Cross-shore bathymetry, and countours of initial conditions for density and DO. The bathymetry base case with a slope $\alpha = 1. \times 10^{-3}$ is in black, and 4 additional scenarios with bumps implemented according to Eq.4.1. A schematic of the parameters used to construct the bumps is shown in the right panel.

Other bathymetric configurations were tested (i.e., a "step" instead of a bump), but the effects were much reduced in contrast to the bump configuration and are not discussed.

Boundary conditions are periodic along-shore, closed at the coast, and open at the offshore side. In the open boundary, all three-dimensional variables have a no-gradient condition, while

barotropic velocities are set to Flather, and sea surface height to Chapman (Flather, 1976; Chapman, 1985) conditions.

Initial conditions in temperature and salinity satisfy $N^2 = 1.0 \times 10^{-4}$, $M^2 = 1.0 \times 10^{-6}$, where N^2 and M^2 are the vertical and horizontal stratification respectively, and the coriolis parameter f was set uniformly to 1.0×10^{-4}. DO was initialized in saturation state everywhere following the empirical formulation of Garcia and Gordon (1992) as a function of salinity and temperature:

$$\begin{aligned} \ln Ox_{sat} = {} & 2.00907 + 3.22014 T_s + 4.0501 T_s^2 + 4.94457 T_s^2 + 4.94457 T_s^3 \\ & - 0.256847 T_s^4 + 3.88767 T_s^5 + S(-0.00624523 - 0.00737614 T_s \\ & - 0.010341 T_s^2 - 0.00817083 T_s^3) - 4.88682 \times 10^{-7} S^2, \end{aligned} \tag{4.2}$$

The saturation state is further imposed at the surface layer at every time-step, in the same manner as for the TXLA model.

For base comparison, all bathymetry setups have a run without external forcing. Additional runs were performed in two settings. An upwelling-favorable momentum forcing (uw) was set with an along-shore and spatially uniform wind (-5 m·s^{-1}), with an initial ramp of 5 days. A realistic forcing record from the NBDC Buoy 42035 for August 2010 was obtained through the Texas Automated Buoy System (TABS) website (see Fig.4.2). All performed runs with bathymetry and wind combinations are summarized in Table 4.1.

4.2.2 Apparent oxygen utilization, intrusions and energetics

In this idealized setup, values of oxygen concentration are anecdotal, or rather not comparable to realistic values, due to aspects like the periodic boundary condition, the model initialization with a constant cross-shore horizontal density gradient determined by salinity, and no additional freshwater input over time. Under these conditions, the idealized runs do not reach the hypoxic threshold. Hence, concentrations are expressed in terms of apparent oxygen utilization (AOU), obtained by:

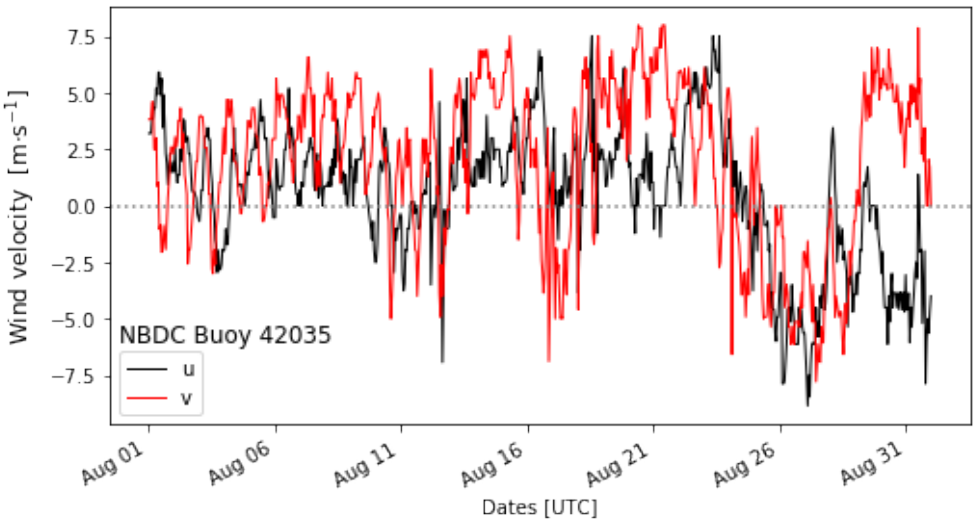

Figure 4.2: Wind velocity components time forcing used for the realistic wind (rw) scenarios

Table 4.1: List of model simulation cases by bathymetry (bump distance and height) and forcing. Frocing options included no external forcing, upweling favorable winds (constant wind of -5 m·s^{-1}) or realistic winds from the TABS buoy for August 2010 (rw).

Run	δh [m]	D [km]	u wind [m·s^{-1}]
1	0	0	0
2	5	20	0
3	5	50	0
4	10	20	0
5	10	50	0
6	0	0	-5
7	5	20	-5
8	5	50	-5
9	10	20	-5
10	10	50	-5
11	0	0	rw
12	5	20	rw
13	5	50	rw
14	10	20	rw
15	10	50	rw

$$AOU = Ox - Ox_{sat} \tag{4.3}$$

which measures the difference between the local DO concentration and the saturation concentration in water with the same temperature and salinity conditions. In the idealized context, AOU measures the sum of sediment oxygen demand a water parcel has experienced since either the initialization or its contact with the surface, given that there is no water column respiration term.

To evaluate vertical ventilation of dissolved oxygen in the water column induced by the passing of baroclinic instabilities, we define the DO vertical turbulent flux across a horizontal plane at depth z as

$$\left\langle w' Ox' \right\rangle_z = \left. \frac{\iint w'\, Ox'\, dx\, , dy}{\iint dx\, , dy} \right|_z , \tag{4.4}$$

Eq.4.4 expresses the product of the vertical velocity anomaly w' and the DO anomaly Ox', where anomalies are defined as

$$\begin{aligned} w' &= w - \langle w \rangle \\ Ox' &= Ox - \langle Ox \rangle \end{aligned} \tag{4.5}$$

where $\langle \cdot \rangle$ denotes a spatial Reynolds average over the plane z and $\langle w \rangle = 0$ in the idealized domain. For practical reasons, due to the bathymetry configuration (i.e., the height of the largest bump), we chose $z = -10$ m depth. Here, we utilize the local dissolved oxygen value in contrast to AOU, due to the need to establish a true anomaly value.

Fig.4.3 illustrates how intrusions are related to the negative vertical turbulent flux. A negative value of the DO vertical turbulent flux would indicate net oxygenation of the water column below z. Bottom intrusions are categorized as negative DO anomalies moving upwards. By volume conservation, these motions are compensated by downward motion of positive DO anomalies, which are here defined as ventilation.

Baroclinic instabilities can be measured by the change in the eddy kinetic energy from the

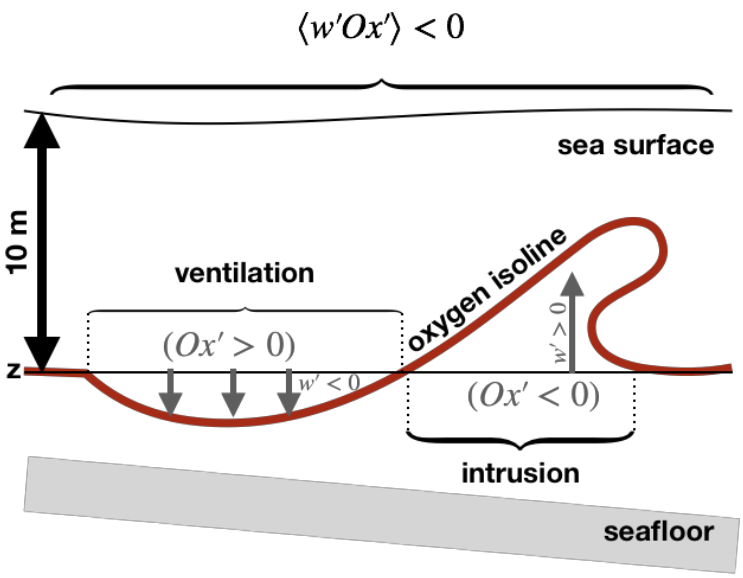

Figure 4.3: Schematic of the negative vertical oxygen turbulent flux $w'Ox'$, with indication of the uplifting portion (intrusion) and the downward ventilation portion (ventilation). Anomalies, w' and Ox', are defined as deviations from the spatial mean at the surface $z = -10$ per Eq.4.5. The resulting mean turbulent flux, $\langle w'Ox' \rangle$ oxygenates the bottom waters.

initial mean state over time (see Hetland (2017) for a detailed discussion). Hence, following Hetland (2017), time dependent eddy kinetic energy (EKE) is normalized by the initial mean kinetic energy ($MKE_{Initial}$) to quantify the average energetics in the simulation domain:

$$EKE_{NORM} = \frac{EKE(t)}{MKE_{Initial}} = \frac{\iiint \frac{1}{2}(u-U)^2 \, dV}{\iiint \frac{1}{2}U^2\big|_{t=0} \, dV}, \tag{4.6}$$

were u is the alongshore flow, and U the alogshore mean flow as defined by:

$$U = \frac{1}{L}\int_0^L u \, dx, \tag{4.7}$$

4.3 Results

The set of idealized simulations was run for 30 days for all cases. Time series of the base case (Fig.4.4), and the base case with realistic forcing (Fig.4.5) show the formation and evolution of instabilities in the surface salinity field, and the modulation effect at the bottom in the AOU field.

While the AOU does not match the surface salinity, it takes the form of eddy-like features with higher utilization at the edges and stronger ventilation in the center of the features. The freshwater envelope populated with instabilities extends from the initial 50 km cross-shore reach to about 75 km by the end of the simulation in the no-forcing scenario and about 100 km with the realistic forcing. The change in cross-shore reach of the eddy-like features in the bottom AOU is not as strong by the end. Oxygen utilization is significantly reduced at all stages of the simulation of the realistic forcing scenario compared to the no forcing scenario.

A time series of the normalized EKE summarizes the evolution of instabilities in the domain (Fig.4.6). All simulations excepting iterations with the 5 m bump are shown. All effects on simulations over 5 m bump bathymetry were significantly reduced compared to the 10 m bump simulations, which will not going to be discussed further. For all cases, there is an initial increase in the eddy kinetic energy following the isopycnal relaxation from the initial conditions. The forcing gives the most significant effect in the evolution of the eddy-field. A continuous upwelling forcing suppresses the eddies development in contrast to no forcing and realistic forcing (after the ramp starts at day 5). The increasing trend continues until about day 12 when the EKE evens out. Strong oscillations in the EKE develop as a response to the land-sea breeze pattern in the realistic wind forcing. The effect of bathymetry becomes negligible when comparing shelf-wide integrated EKE.

The mean cross-shore eddy density is shown in Fig.4.7 . Here, the normalized EKE is averaged in time and the cross-shore direction, from day 12 until the end of the simulation. For the no wind and realistic wind simulations, peak eddy activity is localized around 40 km from shore. For the upwelling wind simulation, eddies are greatly suppressed.

A spatial power spectral density (PSD) applied in the cross-shore dimension is used to compare the energy distribution per space unit of salinity (as a tracer of instabilities) at the surface and bottom, and bottom dissolved oxygen. For the analysis, all properties are scaled to 1 against the spatial maximum, so the signals in the along-shore direction, rather than the property value, are compared. Fig.4.8 shows the mean PSD over 7 days (from day 12 to 19), at 40 km distance from shore (where eddies are more energetic according to Fig.4.7). In the subset of simulations

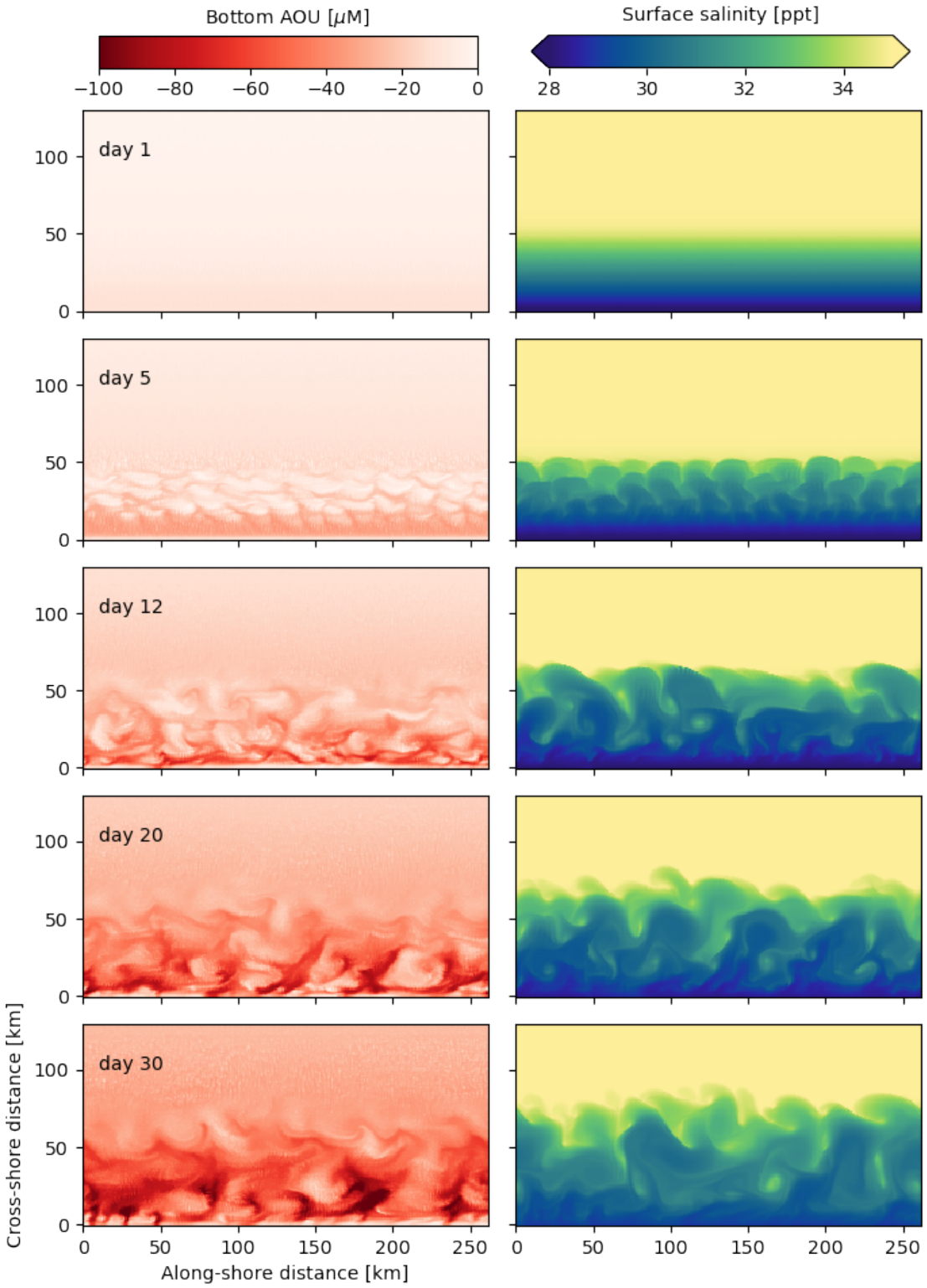

Figure 4.4: Time evolution of the bottom AOU (left) and the surface salinity field (right) for the base case. As expected from the simulations in Hetland (2017), instabilities at day 5 are mature. The modulation effect on the bottom oxygen distribution starts to be seen.

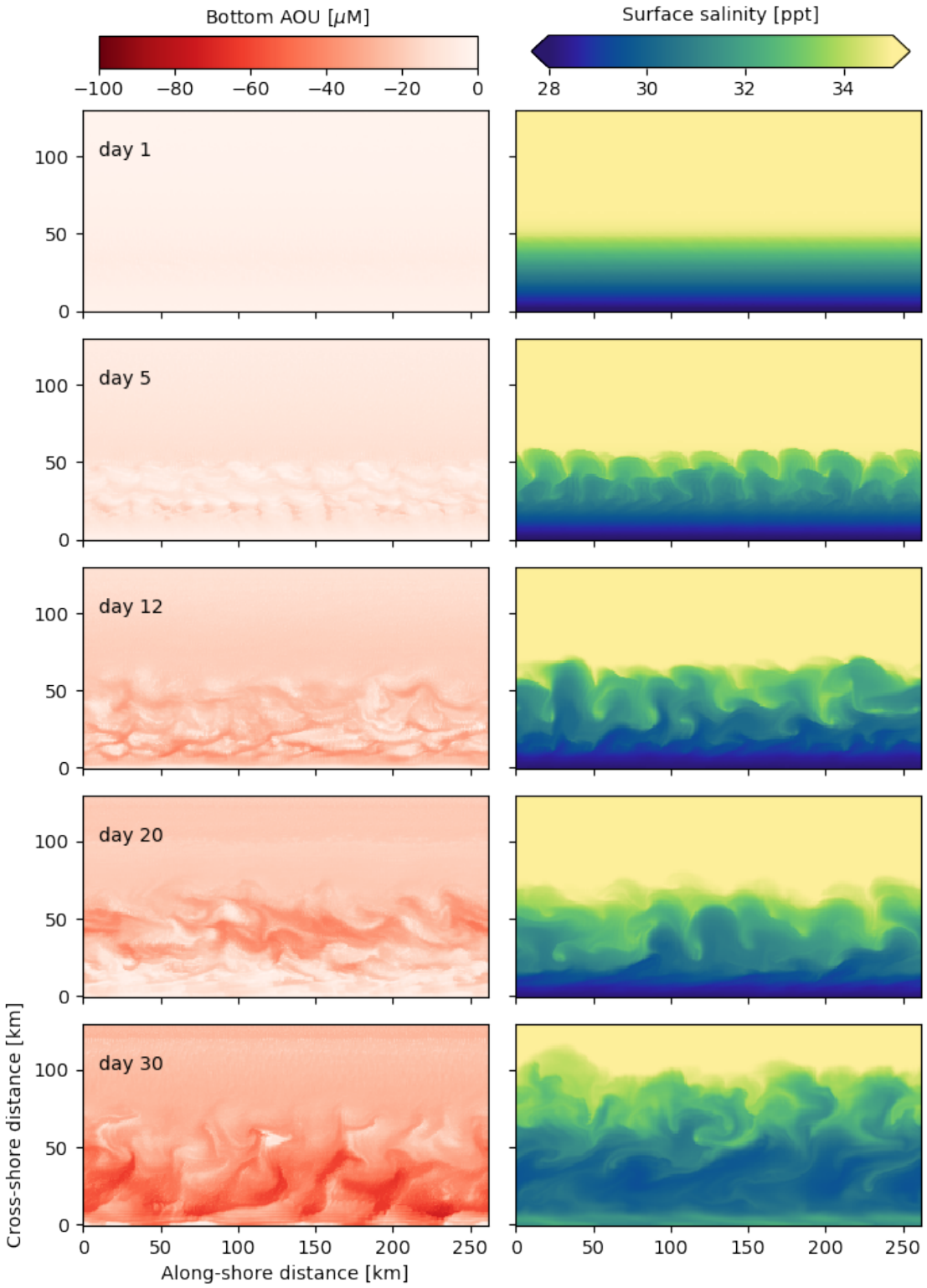

Figure 4.5: Same as Fig.4.4, but the base case with realistic forcing. The stirring effect of the wind is seen in the extension of the eddy field at the surface, and the relative increase of ventilation at the bottom.

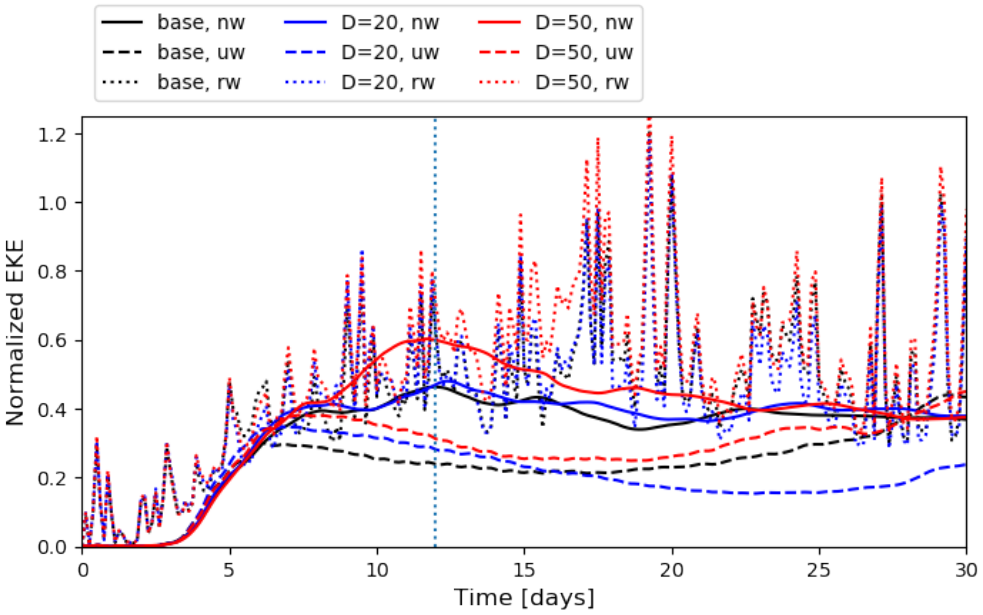

Figure 4.6: Time evolution of the normalized EKE as defined in Eq.4.6, for all iterations of wind forcing over the base case, and the simulations with a 10 m bump (nw: no wind, rw: realistic wind, uw: upwelling wind).

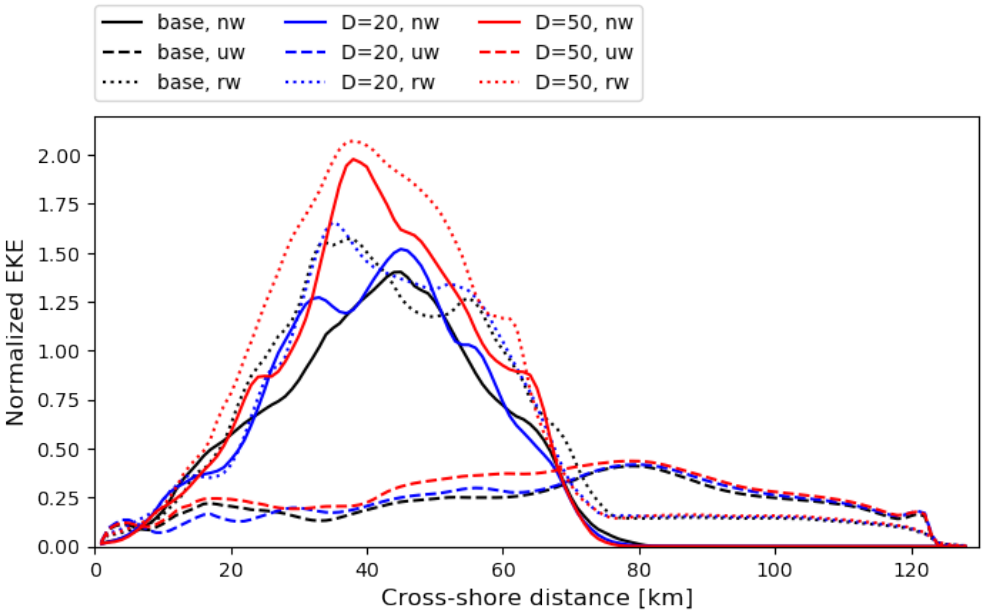

Figure 4.7: Normalized EKE as in Fig.4.6 but along-shore and time averaged (from day 12 to end of simulation). Eddies are contained between 20 and 70 km distance from shore, except for the simulations with upwelling forcing where the eddy-field is suppressed.

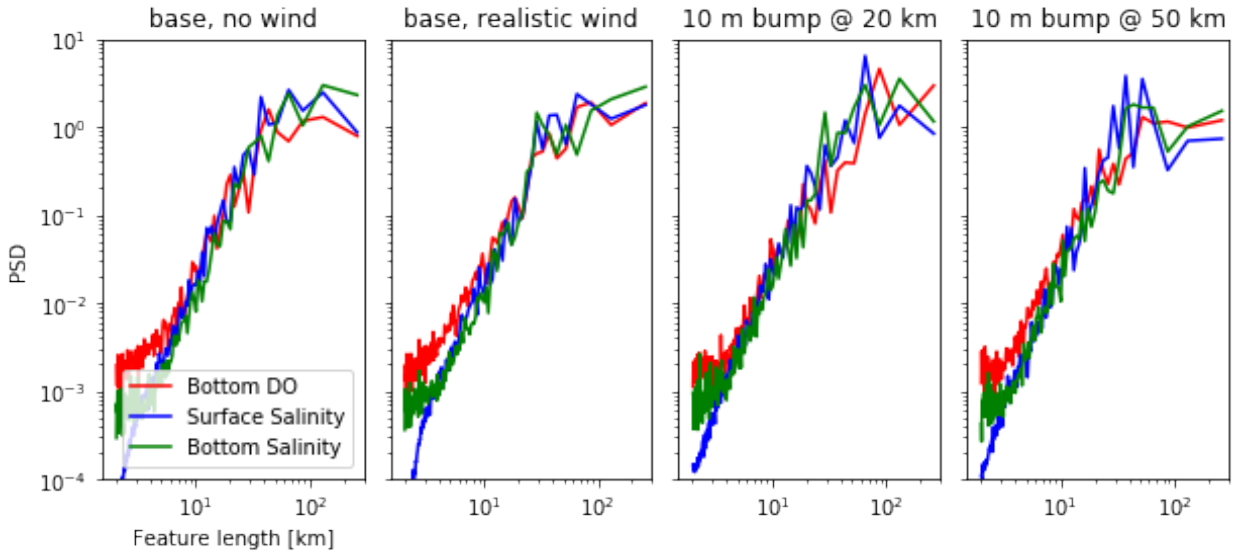

Figure 4.8: Power spectral density of surface and bottom salinity, and bottom DO. The signal frequency is taken in the along shore direction, at a 40 km distance from the shore, where eddies are most energetic. All properties are scaled to 1 for comparison.

presented, the slope of the PSD, namely the decrease of the spectral amplitudes from large to small scale features, is similar for oxygen and salinity for features sized 10 to 100 km, indicating a clear modulating effect of instabilities over the bottom oxygen distribution.

The effect of combined bathymetry and wind forcing on the modulation of the bottom DO can be seen qualitatively in Fig.4.9. The effect of the bump can be seen in the disruptions of the features where the bump crest is located, more strongly in the close-bump scenario (D=20km) than in the far-bump scenario (D=50km). The effect of the wind is seen in the ventilation. Eddy-like features are suppressed in the upwelling simulations, leaving only remnant filaments in the cross-shore direction.

To quantify the net modulation effect on the bottom oxygen, we calculate the volume mean AOU. Fig.4.10 shows a time series of the volume-averaged AOU. Forcing has a much stronger effect on AOU than bathymetric perturbations when considering the entire shelf. However, for the no wind and realistic wind scenarios, there is a slight but consistent increased ventilation for the 20 km bump simulation, and a slight but consistent decrease in ventilation for the external bump

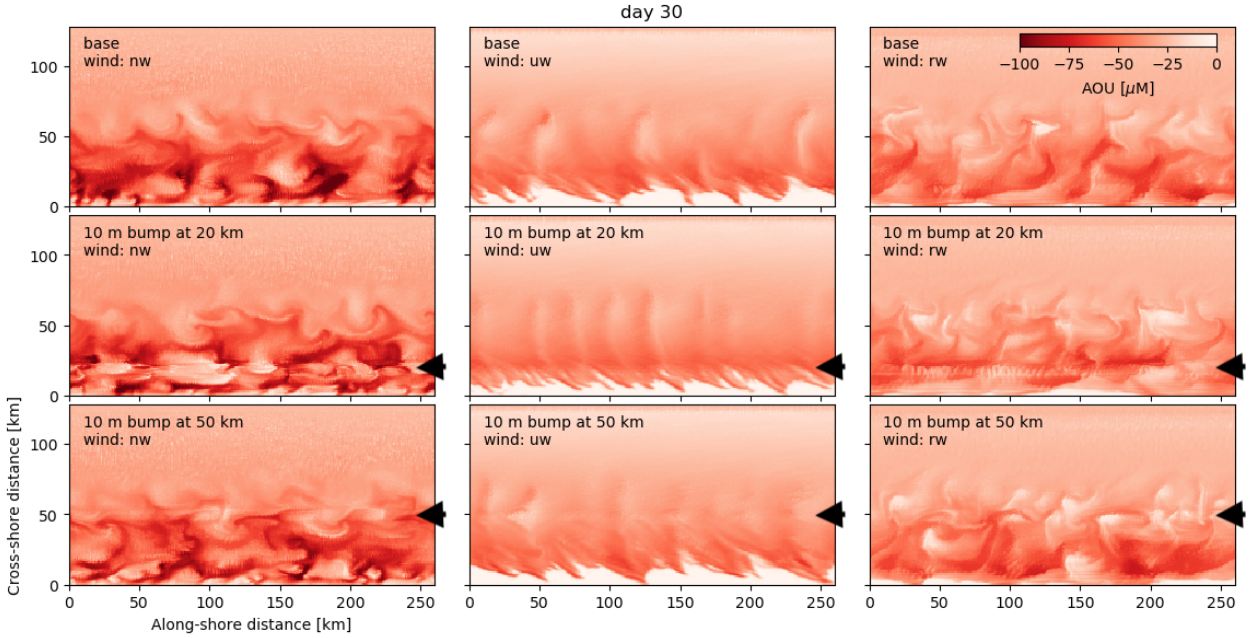

Figure 4.9: Apparent oxygen utilization at the end of the simulation for all scenarios in base case and the 10 m bump. Arrows point to the location of the bump

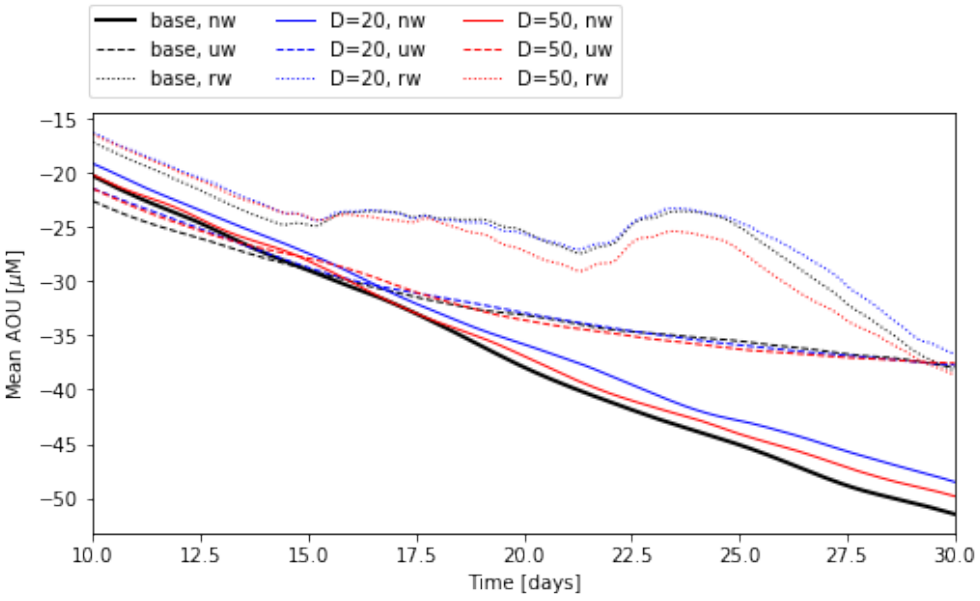

Figure 4.10: Evolution of volume averaged AOU for the entire domain.

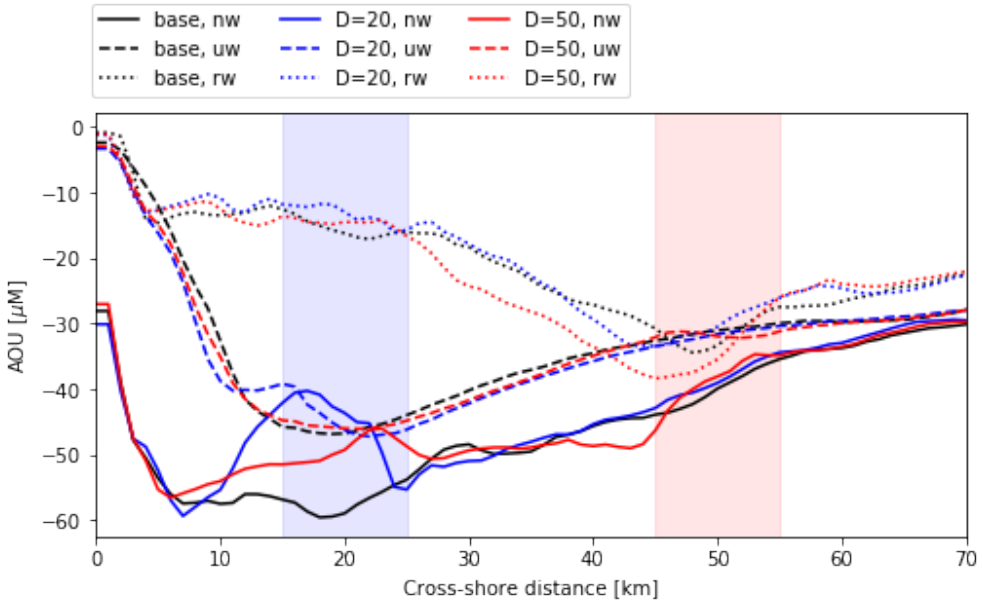

Figure 4.11: Along-shore AOU mean by the end of the simulation. Shaded regions indicate locations of bumps only for the corresponding simulations.

scenario, compared to the single sloping bathymetry. Furthermore, observing a cross-section of the along-shore average, local redistribution due to topography occurs more strongly for the near-shore bump (bump crest a 20 km from shore), particularly at no-wind conditions (Fig.4.11). The relative reduction of the AOU magnitude occurs around the bump. Ventilation is reduced (stronger AOU) for the outer bump (bump crest a 50 km from shore) scenario, from the coast-ward side of the bump and into the mid-shelf on the no forcing and realistic forcing scenarios.

A relationship between the DO vertical turbulent flux is shown in Fig.4.12. As baroclinic instabilities form vertical oxygen flux $w'o'$ increases. On the coast-ward side of the instability, the flux is more energetic due to closer interaction with the bottom. Several intrusions of highly respired water form, as well as several areas of downward ventilation. The wave-like form of the intrusions (right panel) can be observed in the change from upward to downward flux (left panel). The effect of topography is slight but recognizable.

Time series of $w'o'$ for the base case and the 10 m bump at 20 km distance are shown in Fig.4.13 for scenarios without forcing, and with realistic wind forcing. The flux is separated in the upward

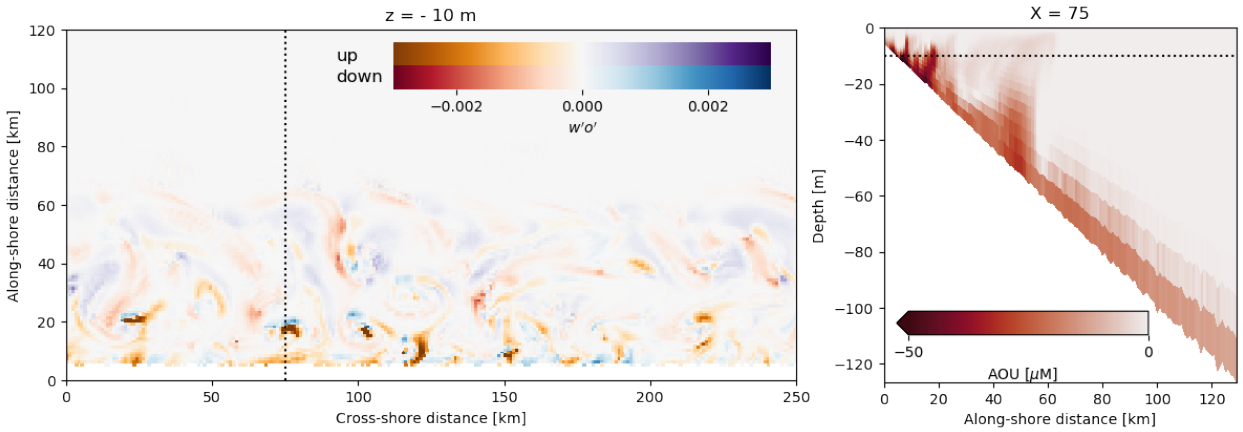

Figure 4.12: Left: Snapshot of the DO vertical turbulent flux at $z = -10m$ depth for day 12 of the base case simulation. A negative flux indicates oxygenation of the bottom (see Fig.4.3). A different colorbar is used for upward flow and downward flow to differentiate downward ventilation and upward intrusion of DO. Right: Vertical section of AOU along the dotted line indicated in the left panel, displaying the formation of intrusions.

and downward component to differentiate downwards ventilation and upwards intrusions. Examination of the time-series shows the transient nature of the vertical flux, and therefore the formation of intrusions. For the no forcing simulations, vertical fluxes are stronger when instabilities start to develop and generally weakens as the instabilities mature. Ventilation (downwards, $w'o' < 0$) occurs mostly further than 20 km offshore, while intrusions are stronger inshore. This is expected because of the closeness of the bottom inshore. For the realistic forcing scenarios, $w'o'$ is dominated by the land-sea breeze pattern of the wind, and downward ventilation is stronger and more prevalent. Long shaped strong intrusions also develop episodically under realistic wind conditions outwards of the bump when the bump is present (after day 15 in the simulation).

4.4 Discussion and Conclusions

The realistic TXLA model, with a simple oxygen parameterization described in previous chapters, simulates eddy-like features in the distribution of the bottom oxygen concentration, where lower concentration borders enclose more oxygenated cores. Qualitative comparisons among the bottom DO, and surface properties that could characterize the presence of instabilities, allows us to reasonably hypothesize that baroclinic instabilities modulate bottom oxygen. However, a direct

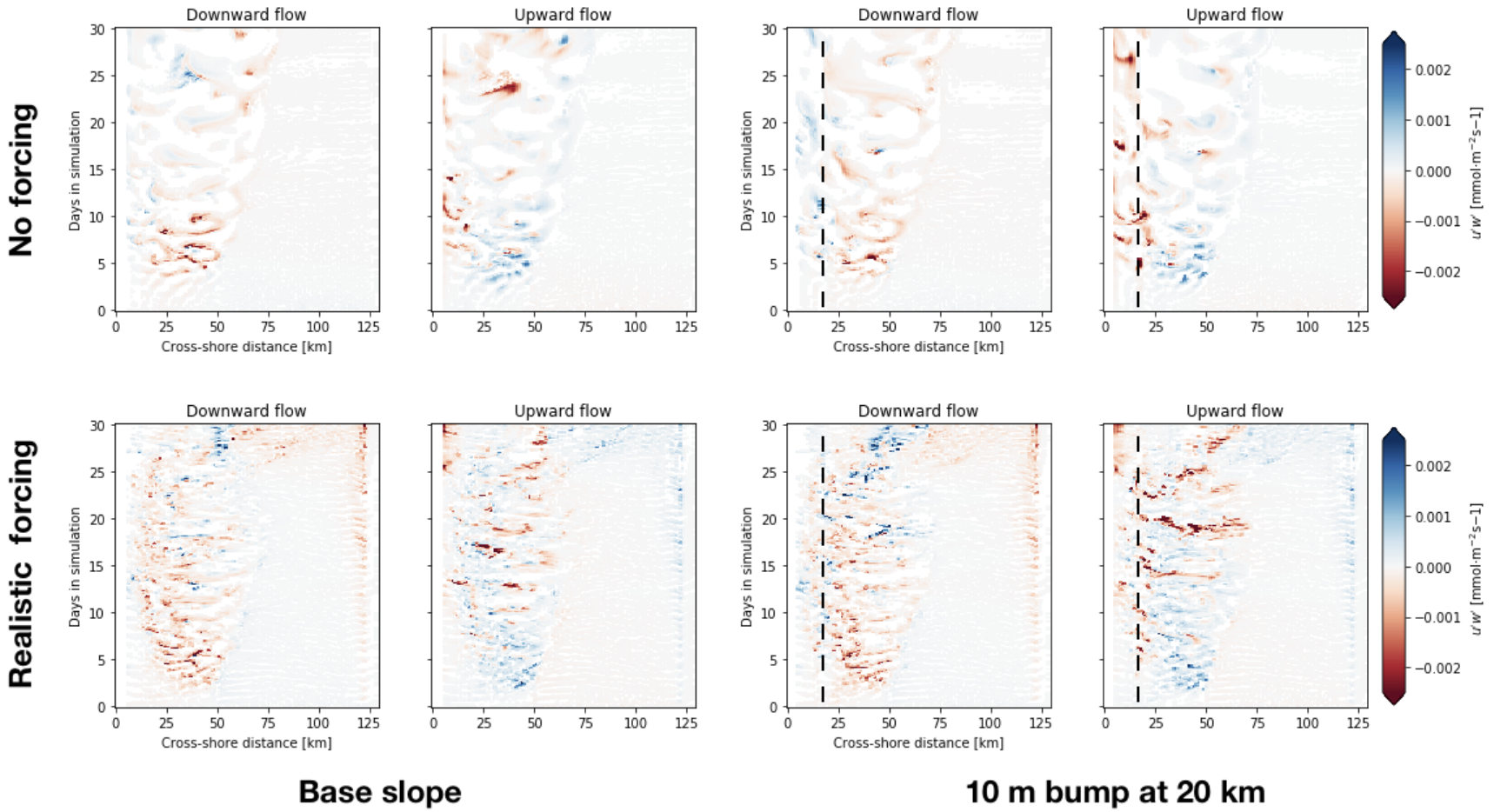

Figure 4.13: Time series of cross-shore $w'o'$ flux trough the $z = -10$ surface for the base slope and near shore bump scenarios. Simlations with no forcing and realistic forcing are shown. The DO vertical turbulent flux is separated into the upward and downward component to differentiate downward ventilation and intrusions.

point to point correlation between surface and bottom has not been found in modeling studies or observations, and no formal proof has been established to relate the spatial scales of surface and bottom features.

The set of idealized simulations presented here reproduce features in the bottom apparent oxygen utilization similar to those observed in realistic simulations of dissolved oxygen. The idealized model is set up to allow buoyancy-driven instabilities to grow in the coastally trapped river plume, following the base parameter space in Hetland (2017). Furthermore, wind effects, and small scale changes in the bathymetry (i.e., a 10 km wide ridge), are tested to evaluate changes in the instability field and the modulation of the bottom oxygen.

The addition of wind forcing drastically impacts the development of the eddy field (Fig.4.6), while the addition of ridges to the initial slope generates a weaker response. The presence of ridges, however, redistributes the cross-shore trend of the eddy kinetic energy.

A similar distribution of feature length between surface salinity and bottom oxygen gives evidence of the modulation effect of the eddies in the distribution of the bottom oxygen (Fig.4.8), and it can be observed in the formation of eddy-like features in the apparent oxygen utilization at the bottom (Fig.4.9. Similar to the EKE, wind forcing has a more substantial effect on the oxygen content at the bottom than topographic disruptions (Fig.4.10). However, locally ridges in the slope create sharp changes in the bottom AOU, especially under no forcing scenarios (weaker under forcing scenarios).

In an idealized study similar to this setup, Zhang and Hetland (2018),used water age to demonstrate that baroclinic instabilities generate transient bottom convergent flow that results in the formation of bottom water intrusions. Here, the scenarios simulated generate intrusions of high AOU into the mid-water column, consistent with those simulated for water age. These intrusions share similarities with observations of uplifted hypoxic waters in vertical sections of high-resolution observations reported by DiMarco and Zimmerle (2017).

The DO vertical turbulent flux $w'o'$ is a way to quantify the ventilation effect of eddies on the bottom. This flow is similar to the vertical buoyancy flux, $w'b'$, as defined by Hetland (2017). In

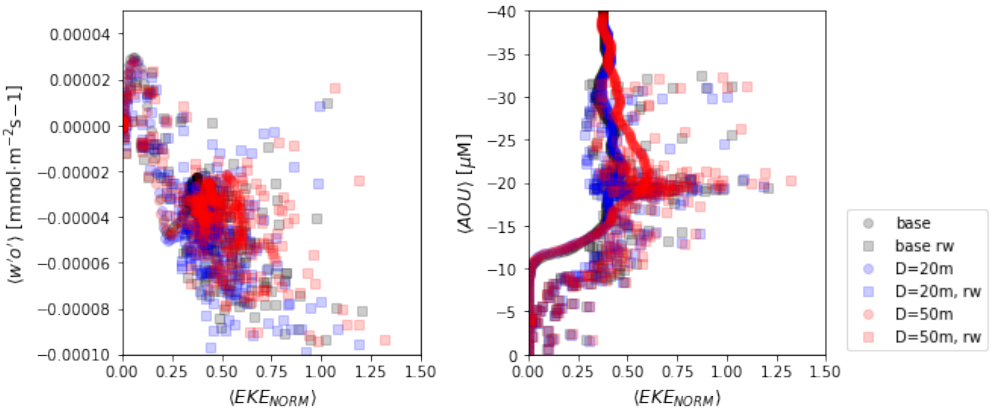

Figure 4.14: Scatter plot of mean normalized eddy kinetic energy vs mean DO vertical turbulent flux and detrended mean AOU. Means are spatial averages, and values are plotted for simulations with no wind and realistic wind, for all times form day 5 onward.

his study, it was demonstrated that the eddy kinetic energy budget is dominated by $\langle w'b' \rangle$, which is an indication that instabilities are primarily driven by baroclinicity and not shear. Here, we found that when eddies are more energetic bottom ventilation is stronger. More energetic eddies generate a stronger DO vertical turbulent flux, resulting in enhanced oxygenation of the bottom (Fig.4.14).

4.5 Acknowledgments

This work is a pure numerical study, and no original data were used. All model runs and computational analyses were performed in the Texas A&M High-Performance Research Computing (HPRC) group cluster Ada. A NOAA grant supported this study through the Coastal Ocean Modeling Testbed (COMT) project, as well as a scholarship from the Texas A&M College of Geosciences.

5. CONCLUSIONS

Bottom hypoxia development in the Northern Gulf of Mexico has been thoroughly studied under different observational and modeling approaches. Observational studies have pointed to different spatial and temporal scales of variability in the hypoxic region. While the areal extent of the hypoxic regions is quantified in the order of 10^4 km, high resolution observations have revealed the presence of patchiness of length scales under 50 km. Temporal observations range from inter-annual variations of the hypoxic extent to high frequency fluctuations of hypoxia in point observations. However, methodological limitations of observational platforms do not allow us to monitor all reported temporal and spatial scales because an increase in resolution requires a reduction of the observation domain, and vice versa. Modeling studies have focused on understanding mechanistic processes that drive temporal and spatial variability in hypoxia. Often, however, modeled features do not match well in space and time with single point observations, although they represent the observed variability statistically in terms of mean and variance. This points to the relevance of understanding the scales of variability in the modeled and observed features, and the mechanistic drivers of the formation of those features, more than on the significance of individual scales of variability. The available information on the different scales of variability reveals a lack of understanding of the variability and driving mechanisms of patchiness inside the hypoxic region.

In this work, we explore the internal variability and short-term shifts in the evolution of seasonal bottom hypoxia, or the dead zone, over the Texas-Louisiana shelf, west of the Mississippi River delta. First, we use a realistic hydrodynamic model with a simple oxygen parameterization to demonstrate that hypoxia development in the far-field of the Mississippi plume is subject to physical processes with spatial scales ranging from $\mathcal{O}$(10km) to $\mathcal{O}$(100km), and temporal scales from the near-inertial period to seasonality. We utilize a budget decomposition of the oxygen equation to explore changes in the budget balance. The mean spatial structure of the local rate of change reveals features shaped as oxygen loss rings enclosing oxygenation cores. This structure is mainly

a balance between net advection, horizontal and vertical, and sediment oxygen demand. In terms of temporal variability, we found a large near-inertial signal in advection, following a convergence divergence pattern, at all spatial scales, and a strong sub-inertial signal at smaller scales only. Variability in advection increases with decreasing temporal and spatial scales, consistently with a field rich in instabilities introducing small-scale, strong anomalies in horizontal oxygen advection. Through a Reynolds decomposition of the budget, we separate anomalies from the main flow and identify the vertical turbulent flux $\langle w'o' \rangle_T$ as the primary counterbalance to sediment oxygen demand during periods when the hypoxic extent is maintained or destroyed. Vertical flux anomalies manifest as bottom water intrusions into the mid-water column, which have been captured by high-resolution observations.

Next, 24 years of model output from the same realistic implementation are used to investigate general trends in the structure of hypoxia. The objective of this study is to challenge the common use of mid-summer cruise estimated extent as a measure of severity and to evaluate interanual trends. Areal extent metrics used for managerial purposes are obtained by shipboard observations usually performed during summer: either the Louisiana Universities Marine Consortium (LUMCON) or the Southeast Area Monitoring and Assessment Program (SEAMAP). Their products are space-time composites and are subject to interpolation artifacts. Hypoxic area estimates from the model simulations reveal how extent can change in an order of magnitude of about $\mathcal{O}(10^3 \text{km}^2)$ in a matter of days as a response to weather events (Fig.3.2.A). By integrating the hypoxic extent over time, we identify the largest and smallest time averaged hypoxic extent between 1994 and 2017, and compare trends in exposure utilizing those years and the interannual climatology. It is shown that most of the spatial structure of hypoxia can be related to the formation of low oxygen intrusions into the interior which is controlled partially by the topography of the shelf, and partially by the growth of instabilities at the surface. Because the vertical flux of oxygenated surface water is the primary mechanism of bottom water ventilation, the presence of intrusions affects considerably the oxygen budget near the bottom. Years with a large river discharge resulting in an extended freshwater envelope, but with suppressed eddy activity, develop severe hypoxia. Years

with a smaller river plume, with more abundant density gradients and energetic eddies populating the surface, develop a much smaller hypoxic region.

Finally a set of idealized model runs, designed to to allow buoyancy-driven instabilities to grow in a coastally trapped river plume, are used to explore the modulation effect of instabilities over the bottom dissolved oxygen distribution. Forcing and the introduction of small ridges in the bathymetry are tested to evaluate changes in the instability field and the modulation. Wind forcing drastically impacts the development of the eddy field at the surface as well as the apparent oxygen utilization at the bottom. Little response is seen in either field with the introduction of ridges when looking at the entire shelf, but the bathymetry does have an effect in redistributing the cross-shore trend of the eddy kinetic energy, and therefore in the bottom oxygen concentration. The length scales associated with surface salinity are found to have the same power density spectra as bottom salinity and bottom oxygen, establishing a direct relationship among them. The scenarios simulated generate intrusions of high AOU into the mid-water column, consistent with other idealized studies, and sharing similarities with observations of uplifted hypoxic waters in vertical sections of high-resolution observations.

5.1 Some final considerations

Small-scale variability, developing and moving in the larger scale hypoxic extent has ecological implications. Distinct functional groups of organisms (e.g. species and life stages), have been found to have different horizontal and vertical avoidance strategies towards hypoxic waters (Hazen et al., 2009), and benthic and especially sessile organisms have to develop resistance strategies adaptable to different temporal scales (Villnäs et al., 2012). Pelagic fish and mesozooplankton adjust their behavior and distribution around hypoxic patches using different patterns of avoidance and spatial overlap depending on the severity of hypoxia (Zhang et al., 2009). Hence, it is important to develop metrics of severity that capture variability realistically in time and space, in contrast of using a simple metric of extent.

Submesoscale variability also has implications for the redistribution and small scale patterns in primary productivity, carbon export and biogeochemistry (Mahadevan, 2014; Middelburg and

Levin, 2009). The interaction of eddies with the bottom indicates that intrusions generated by convergence at the bottom will not only uplift low oxygen concentration waters, but also other types of tracers found in higher concentration in proximity to the sediment. It is also worth considering that bottom water uplifting can be tied with sediment resuspension. Sediment resuspension in the bottom boundary layer can also increase respiration across the entire mixed layer, and this effect is not considered in the TXLA model. Currently, there are several groups working in the coupling of models with sediment resuspension capabilities which could improve our understanding in the complex interaction of instabilities with the shelf bottom.

While there are not enough observations available to validate the claims obtained from the realistic model, some generalizations can be drawn from long term hidcast output, which should be used to design future high resolution observation surveys. High resolution vertical sections have been shown to be useful to observe the complex morphology in properties like dissolved oxygen, salinity and turbidity. A series of similar surveys, designed to capture some temporal shifts could validate the relevance of horizontal motions at small spatial and temporal scales. Areal estimates from hindcasts can also be used to reevaluate correlations with fisheries and fish landings (e.g., O'Connor and Whitall, 2007; Smith et al., 2017).

REFERENCES

Arakawa, A. and Lamb, V. R. (1977). Computational design of the basic dynamical processes of the UCLA General Circulation Model. In Chang, J., editor, *General Circulation Models of the Atmosphere*, volume 17 of *Methods in Computational Physics: Advances in Research and Applications*, pages 173–265. Elsevier.

Bell, G. W. and Eggleston, D. B. (2005). Species-specific avoidance responses by blue crabs and fish to chronic and episodic hypoxia. *Marine Biology*, 146(4):761–770.

Bianchi, T. S., Allison, M. A., Chapman, P., Cowan, J. H., Dagg, M. J., Day, J. W., DiMarco, S. F., and Powell, R. (2010a). New approaches to the Gulf hypoxia problem. *Eos, Transactions American Geophysical Union*, 91(19):173–173.

Bianchi, T. S., DiMarco, S. F., Allison, M. A., Chapman, P., Cowan, J. H., Hetland, R. D., Morse, J. W., and Rowe, G. (2008). Controlling hypoxia on the U.S. Louisiana shelf: Beyond the nutrient-centric view. *Eos, Transactions American Geophysical Union*, 89(26):236.

Bianchi, T. S., DiMarco, S. F., Cowan, J. H., Hetland, R. D., Chapman, P., Day, J., and Allison, M. A. (2010b). The science of hypoxia in the northern Gulf of Mexico: A review. *Science of the Total Environment*, 408(7):1471–1484.

Burchard, H. and Rennau, H. (2008). Comparative quantification of physically and numerically induced mixing in ocean models. *Ocean Modelling*, 20(3):293–311.

Chapman, D. C. (1985). Numerical treatment of cross-shelf open boundaries in a barotropic coastal ocean model. *Journal of Physical Oceanography*, 15(8):1060–1075.

Chen, C., Reid, R. O., and Nowlin, W. D. (1996). Near-inertial oscillations over the Texas-Louisiana shelf. *Journal of Geophysical Research: Oceans*, 101:3509–3524.

Chen, C. and Xie, L. (1997). A numerical study of wind-induced, near-inertial oscillations over the Texas-Louisiana shelf. *Journal of Geophysical Research C: Oceans*, 102:15583–15593.

Cochrane, J. D. and Kelly, F. J. (1986). Low-frequency circulation on the Texas-Louisiana continental shelf. *Journal of Geophysical Research*, 91(C9):10645.

Dale, V. H., Bianchi, T. S., Blumberg, A., Boynton, W., Conley, D. J., Crumpton, W., David, M., Gilbert, D., Howarth, R. W., Kling, C. L., Lowrance, R., Mankin, K., Meyer, J. L., Opaluch, J., Paerl, H. W., Reckhow, K., Simpson, T. W., Snyder, C. S., and Wright, D. (2008). Hypoxia in the northern Gulf of Mexico: An update by the EPA Science Advisory Board. Technical report, EPA Science Advisory Board.

Dee, D. P., Uppala, S. M., Simmons, A. J., Berrisford, P., Poli, P., Kobayashi, S., Andrae, U., Balmaseda, M. A., Balsamo, G., Bauer, P., Bechtold, P., Beljaars, A. C. M., van de Berg, L., Bidlot, J., Bormann, N., Delsol, C., Dragani, R., Fuentes, M., Geer, A. J., Haimberger, L., Healy, S. B., Hersbach, H., Hólm, E. V., Isaksen, L., Kållberg, P., Köhler, M., Matricardi, M., McNally, A. P., Monge-Sanz, B. M., Morcrette, J.-J., Park, B.-K., Peubey, C., de Rosnay, P., Tavolato, C., Thépaut, J.-N., and Vitart, F. (2011). The ERA-Interim reanalysis: configuration and performance of the data assimilation system. *Quarterly Journal of the Royal Meteorological Society*, 137(656):553–597.

Diaz, R. J. and Rosenberg, R. (2008). Spreading dead zones and consequences for marine ecosystems. *Science*, 321(5891):926–929.

DiMarco, S. and Zimmerle, H. (2017). *MCH Atlas: Oceanographic Observations of the Mechanisms Controlling Hypoxia Project*. Texas A&M University, Texas Sea Grant Publication TAMU-SG-17-601.

DiMarco, S. F., Chapman, P., Walker, N., and Hetland, R. D. (2010). Does local topography control hypoxia on the eastern Texas-Louisiana shelf? *Journal of Marine Systems*, 80(1):25–35.

DiMarco, S. F., Howard, M. K., and Reid, R. O. (2000). Seasonal variation of wind-driven diurnal current cycling on the Texas-Louisiana continental shelf. *Geophysical Research Letters*, 27(7):1017–1020.

DiMarco, S. F. and Reid, R. O. (1998). Characterization of the principal tidal current constituents on the Texas-Louisiana shelf. *Journal of Geophysical Research: Oceans*, 103(C2):3093–3109.

Eldridge, P. M. and Morse, J. W. (2008). Origins and temporal scales of hypoxia on the Louisiana shelf: Importance of benthic and sub-pycnocline water metabolism. *Marine Chemistry*, 108(3-

4):159–171.

Fairall, C., Bradley, E. F., and Rogers, D. P. (1996). The TOGA COARE bulk flux algorithm. *J. Geophys. Res*, 101:3747–3764.

Feng, Y., DiMarco, S. F., and Jackson, G. A. (2012). Relative role of wind forcing and riverine nutrient input on the extent of hypoxia in the northern Gulf of Mexico. *Geophysical Research Letters*, 39(9):L09601–L09601.

Feng, Y., Fennel, K., Jackson, G. A., DiMarco, S. F., and Hetland, R. D. (2014). A model study of the response of hypoxia to upwelling-favorable wind on the northern Gulf of Mexico shelf. *Journal of Marine Systems*, 131:63–73.

Fennel, K., Hetland, R. D., Feng, Y., and DiMarco, S. F. (2011). A coupled physical-biological model of the Northern Gulf of Mexico shelf: model description, validation and analysis of phytoplankton variability. *Biogeosciences*, 8(7):1881–1899.

Fennel, K., Hu, J., Laurent, A., Marta-Almeida, M., and Hetland, R. D. (2013). Sensitivity of hypoxia predictions for the northern Gulf of Mexico to sediment oxygen consumption and model nesting. *Journal of Geophysical Research: Oceans*, 118(2):990–1002.

Fennel, K. and Laurent, A. (2018). N and P as ultimate and proximate limiting nutrients in the northern Gulf of Mexico: implications for hypoxia reduction strategies. *Biogeosciences*, 15(10):3121–3131.

Fennel, K., Laurent, A., Hetland, R., Justic, D., Ko, D. S., Lehrter, J., Murrell, M., Wang, L., Yu, L., and Zhang, W. (2016). Effects of model physics on hypoxia simulations for the northern Gulf of Mexico: A model intercomparison. *Journal of Geophysical Research: Oceans*, 121(8):5731–5750.

Flather, R. (1976). A tidal model of the northwest European continental shelf. *Mem. Soc. R. Sci.*, 10(6):141–164.

Forrest, D. R., Hetland, R. D., and DiMarco, S. F. (2011). Multivariable statistical regression models of the areal extent of hypoxia over the Texas-Louisiana continental shelf. *Environmental Research Letters*, 6(4):045002.

Friedrich, J., Janssen, F., Aleynik, D., Bange, H. W., Boltacheva, N., Çagatay, M. N., Dale, A. W., Etiope, G., Erdem, Z., Geraga, M., Gilli, A., Gomoiu, M. T., Hall, P. O. J., Hansson, D., He, Y., Holtappels, M., Kirf, M. K., Kononets, M., Konovalov, S., Lichtschlag, A., Livingstone, D. M., Marinaro, G., Mazlumyan, S., Naeher, S., North, R. P., Papatheodorou, G., Pfannkuche, O., Prien, R., Rehder, G., Schubert, C. J., Soltwedel, T., Sommer, S., Stahl, H., Stanev, E. V., Teaca, A., Tengberg, A., Waldmann, C., Wehrli, B., and Wenzhöfer, F. (2014). Investigating hypoxia in aquatic environments: Diverse approaches to addressing a complex phenomenon. *Biogeosciences*, 11(4):1215–1259.

Garcia, H. E. and Gordon, L. I. (1992). Oxygen solubility in seawater: Better fitting equations. *Limnology and Oceanography*, 37(6):1307–1312.

Greene, R. M., Lehrter, J. C., and Hagy III, J. D. (2009). Multiple regression models for hindcasting and forecasting midsummer hypoxia in the Gulf of Mexico. *Ecological Applications*, 19(5):1161–1175.

Haidvogel, D., Arango, H., Budgell, W., Cornuelle, B., Curchitser, E., Di Lorenzo, E., Fennel, K., Geyer, W., Hermann, A., Lanerolle, L., Levin, J., McWilliams, J., Miller, A., Moore, A., Powell, T., Shchepetkin, A., Sherwood, C., Signell, R., Warner, J., and Wilkin, J. (2008). Ocean forecasting in terrain-following coordinates: Formulation and skill assessment of the Regional Ocean Modeling System. *Journal of Computational Physics*, 227(7):3595–3624.

Harper, D. E., Mckinney, L. D., Salzer, R. R., and Case, R. J. (1981). The ocurrence of hypoxic bottom water off the upper Texas coast and its effects on the benthic biota. *Contribution in Marine Science*, 24:53–79.

Hazen, E., Craig, J., Good, C., and Crowder, L. (2009). Vertical distribution of fish biomass in hypoxic waters on the Gulf of Mexico shelf. *Marine Ecology Progress Series*, 375:195–207.

Hetland, R. D. (2017). Suppression of baroclinic instabilities in buoyancy-driven flow over sloping bathymetry. *Journal of Physical Oceanography*, 47(1):49–68.

Hetland, R. D. and DiMarco, S. F. (2008). How does the character of oxygen demand control the structure of hypoxia on the Texas-Louisiana continental shelf? *Journal of Marine Systems*,

70(1):49–62.

Hetland, R. D. and DiMarco, S. F. (2012). Skill assessment of a hydrodynamic model of circulation over the Texas-Louisiana continental shelf. *Ocean Modelling*, 43-44:64–76.

Hofmann, A. F., Peltzer, E. T., Walz, P. M., and Brewer, P. G. (2011). Hypoxia by degrees: Establishing definitions for a changing ocean. *Deep-Sea Research Part I: Oceanographic Research Papers*, 58(12):1212–1226.

Horner-Devine, A. R., Hetland, R. D., and MacDonald, D. G. (2015). Mixing and transport in coastal river plumes. *Annual Review of Fluid Mechanics*, 47(1):569–594.

Justić, D., Rabalais, N. N., and Turner, R. E. (1996). Effects of climate change on hypoxia in coastal waters: a doubled CO_2 scenario for the northern Gulf of Mexico. *Limnology and Oceanography*, 41(5):992–1003.

Justić, D. and Wang, L. (2014). Assessing temporal and spatial variability of hypoxia over the inner Louisiana-upper Texas shelf: Application of an unstructured-grid three-dimensional coupled hydrodynamic-water quality model. *Continental Shelf Research*, 72:163–179.

Kemp, W. M., Testa, J. M., Conley, D. J., Gilbert, D., and Hagy, J. D. (2009). Temporal responses of coastal hypoxia to nutrient loading and physical controls. *Biogeosciences*, 6(12):2985–3008.

Ko, D., Gould, R., Penta, B., and Lehrter, J. (2016). Impact of satellite remote sensing data on simulations of coastal circulation and hypoxia on the Louisiana continental shelf. *Remote Sensing*, 8(5):435–435.

Laurent, A. and Fennel, K. (2013). Simulated reduction of hypoxia in the northern Gulf of Mexico due to phosphorus limitation. *Elementa: Science of the Anthropocene*, 2:000022–000022.

Laurent, A., Fennel, K., Hu, J., and Hetland, R. D. (2012). Simulating the effects of phosphorus limitation in the Mississippi and Atchafalaya river plumes. *Biogeosciences*, 9(11):4707–4723.

Laurent, A., Fennel, K., Ko, D. S., and Lehrter, J. (2018). Climate change projected to exacerbate impacts of coastal eutrophication in the Northern Gulf of Mexico.

Levin, L. A., Ekau, W., Gooday, A. J., Jorissen, F., Middelburg, J. J., Naqvi, S. W., Neira, C., Rabalais, N. N., and Zhang, J. (2009). Effects of natural and human-induced hypoxia on coastal

benthos. *Biogeosciences*, 6(10):2063–2098.

Li, M., Lee, Y. J., Testa, J. M., Li, Y., Ni, W., Kemp, W. M., and Di Toro, D. M. (2016). What drives interannual variability of hypoxia in Chesapeake Bay: Climate forcing versus nutrient loading? *Geophysical Research Letters*, 43(5):2127–2134.

Li, Y., Li, M., and Kemp, W. M. (2015). A budget analysis of bottom-water dissolved oxygen in Chesapeake Bay. *Estuaries and Coasts*, 38(6):2132–2148.

Li, Y., Nowlin, W. D., and Reid, R. O. (1996). Spatial-scale analysis of hydrographic data over the Texas-Louisiana continental shelf. *Journal of Geophysical Research: Oceans*, 101(C9):20595–20605.

Mahadevan, A. (2014). Eddy effects on biogeochemistry. *Nature*, 506(7487):168–169.

May, E. B. (1973). Extensive oxygen depletion in Mobile Bay, Alabama. *Limnology and Oceanography*, 18(3):353–366.

Meire, L., Soetaert, K. E. R., and Meysman, F. J. R. (2013). Impact of global change on coastal oxygen dynamics and risk of hypoxia. *Biogeosciences*, 10(4):2633–2653.

Middelburg, J. J. and Levin, L. A. (2009). Coastal hypoxia and sediment biogeochemistry. *Biogeosciences*, 6(7):1273–1293.

Nowlin, W. D., Jochens, A. E., DiMarco, S. F., Reid, R. O., and Howard, M. K. (2005). Low-frequency circulation over the Texas-Louisiana continental shelf. In *GEOPHYSICAL MONOGRAPH*, volume 161, pages 219–240. American Geophysical Union (AGU).

Obenour, D. R., Michalak, A. M., and Scavia, D. (2015). Assessing biophysical controls on Gulf of Mexico hypoxia through probabilistic modeling. *Ecological Applications*, 25(2):492–505.

Obenour, D. R., Scavia, D., Rabalais, N. N., Turner, R. E., and Michalak, A. M. (2013). Retrospective analysis of midsummer hypoxic area and volume in the northern Gulf of Mexico, 1985-2011. *Environmental Science and Technology*, 47(17):9808–9815.

O'Connor, T. and Whitall, D. (2007). Linking hypoxia to shrimp catch in the northern Gulf of Mexico. *Marine Pollution Bulletin*, 54(4):460–463.

Qu, L. and Hetland, R. (2020). Non-geostrophic baroclinic instability over sloping bathymetry:

buoyant flow regime. *Journal of Physical Oceanography*, pages JPO–D–19–0145.1.

Quiñones Rivera, Z., Wissel, B., Justić, D., and Fry, B. (2007). Partitioning oxygen sources and sinks in a stratified, eutrophic coastal ecosystem using stable oxygen isotopes. *Marine Ecology Progress Series*, 342:69–83.

Rabalais, N. N., Díaz, R. J., Levin, L. A., Turner, R. E., Gilbert, D., and Zhang, J. (2010). Dynamics and distribution of natural and human-caused hypoxia. *Biogeosciences*, 7(2):585–619.

Rabalais, N. N., Smith, L. E., Harper, D. E., and Justic, D. (2001a). Effects of seasonal hypoxia on continental shelf benthos. In Rabalais, N. N. and Turner, R. E., editors, *Coastal hypoxia: consequences for living resources and ecosystems*, volume 58 of *Coastal and Estuarine Studies*, pages 211–240. American Geophysical Union.

Rabalais, N. N. and Turner, R. E. (2001). Hypoxia in the northern Gulf of Mexico: Description, causes and change. In Rabalais, N. N. and Turner, R. E., editors, *Coastal Hypoxia: Consequences for Living Resources and Ecosystems.*, Coastal and Estuarine Studies, pages 1–36. American Geophysical Union.

Rabalais, N. N. and Turner, R. E. (2006). Oxygen depletion in the Gulf of Mexico adjacent to the Mississippi River. In *Past and Present Water Column Anoxia*, pages 225–245. Kluwer Academic Publishers.

Rabalais, N. N., Turner, R. E., Sen Gupta, B. K., Boesch, D. F., Chapman, P., and Murrell, M. C. (2007). Hypoxia in the northern Gulf of Mexico: Does the science support the Plan to Reduce, Mitigate, and Control Hypoxia? *Estuaries and Coasts*, 30(5):753–772.

Rabalais, N. N., Turner, R. E., and Wiseman, W. J. (2001b). Hypoxia in the Gulf of Mexico. *Journal of Environment Quality*, 30(2):320–320.

Rabalais, N. N., Turner, R. E., and Wiseman, W. J. (2001c). Hypoxia in the Gulf of Mexico. *Journal of Environment Quality*, 30(2):320.

Rabalais, N. N., Wiseman, W. J., and Turner, R. E. (1994). Comparison of continuous records of near-bottom dissolved oxygen from the hypoxia zone along the Louisiana coast. *Estuaries*, 17(4):850–850.

Reissmann, J. H., Burchard, H., Feistel, R., Hagen, E., Lass, H. U., Mohrholz, V., Nausch, G., Umlauf, L., and Wieczorek, G. (2009). Vertical mixing in the Baltic Sea and consequences for eutrophication - a review. *Progress in Oceanography*, 82(1):47–80.

Renaud, M. L. (1986). Hypoxia in Louisiana coastal waters during 1983: Implications for fisheries. *Fishery Bulletin*, 84(1):19–26.

Rowe, G. T. and Chapman, P. (2002). Continental shelf hypoxia: some nagging questions. *Gulf of Mexico Science*, 20(2):155–160.

Scavia, D., Evans, M. A., and Obenour, D. R. (2013). A scenario and forecast model for Gulf of Mexico hypoxic area and volume. *Environmental Science & Technology*, 47(18):10423–10428.

Scavia, D., Rabalais, N. N., Turner, R. E., Justić, D., and Wiseman, W. J. (2003). Predicting the response of Gulf of Mexico hypoxia to variations in Mississippi River nitrogen load. *Limnology and Oceanography*, 48(3):951–956.

Scully, M. E. (2016). The contribution of physical processes to inter-annual variations of hypoxia in Chesapeake Bay: A 30-yr modeling study. *Limnology and Oceanography*, 61(6):2243–2260.

Shchepetkin, A. F. and McWilliams, J. C. (2005). The regional oceanic modeling system (ROMS): a split-explicit, free-surface, topography-following-coordinate oceanic model. *Ocean Modelling*, 9(4):347–404.

Sinokrot, B. A. and Stefan, H. G. (1993). Stream temperature dynamics: Measurements and modeling. *Water Resources Research*, 29(7):2299–2312.

Smith, M. D., Oglend, A., Kirkpatrick, A. J., Asche, F., Bennear, L. S., Craig, J. K., and Nance, J. M. (2017). Seafood prices reveal impacts of a major ecological disturbance. *Proceedings of the National Academy of Sciences*, 114(7):1512–1517.

Smolarkiewicz, P. K. and Margolin, L. G. (1998). MPDATA: A Finite-Difference Solver for Geophysical Flows. *Journal of Computational Physics*, 140(2):459–480.

Soetaert, K. and Middelburg, J. J. (2009). Modeling eutrophication and oligotrophication of shallow-water marine systems: The importance of sediments under stratified and well-mixed conditions. *Hydrobiologia*, 629(1):239–254.

Steckbauer, A., Duarte, C. M., Carstensen, J., Vaquer-Sunyer, R., and Conley, D. J. (2011). Ecosystem impacts of hypoxia: thresholds of hypoxia and pathways to recovery. *Environmental Research Letters*, 6(2):025003–025003.

Testa, J. M., Clark, J. B., Dennison, W. C., Donovan, E. C., Fisher, A. W., Ni, W., Parker, M., Scavia, D., Spitzer, S. E., Waldrop, A. M., Vargas, V. M., and Ziegler, G. (2017). Ecological forecasting and the science of hypoxia in Chesapeake Bay. *BioScience*, 67(7):614–626.

Turner, R., Rabalais, N., and Justic, D. (2006). Predicting summer hypoxia in the northern Gulf of Mexico: Riverine N, P, and Si loading. *Marine Pollution Bulletin*, 52(2):139–148.

Turner, R. E. and Rabalais, N. N. (2019). The Gulf of Mexico. *World Seas: an Environmental Evaluation*, pages 445–464.

Turner, R. E., Rabalais, N. N., and Justic, D. (2008). Gulf of Mexico Hypoxia: Alternate States and a Legacy. *Environmental Science & Technology*, 42(7):2323–2327.

Vastano, A. C., Barron, C. N., and Shaar, E. W. (1995). Satellite observations of the Texas Current. *Continental Shelf Research*, 15(6):729–754.

Villnäs, A., Norkko, J., Lukkari, K., Hewitt, J., and Norkko, A. (2012). Consequences of increasing hypoxic disturbance on benthic communities and ecosystem functioning. *PLoS ONE*, 7(10):e44920–e44920.

Wang, L. and Justić, D. (2009). A modeling study of the physical processes affecting the development of seasonal hypoxia over the inner Louisiana-Texas shelf: Circulation and stratification. *Continental Shelf Research*, 29(11):1464–1476.

Warner, J. C., Armstrong, B., He, R., and Zambon, J. B. (2010). Development of a Coupled Ocean-Atmosphere-Wave-Sediment Transport (COAWST) Modeling System. *Ocean Modelling*, 35(3):230–244.

Warner, J. C., Sherwood, C. R., Arango, H. G., and Signell, R. P. (2005). Performance of four turbulence closure models implemented using a generic length scale method. *Ocean Modelling*, 8(1-2):81–113.

Weiss, R. F. (1970). The solubility of nitrogen, oxygen and argon in water and seawater. In *Deep*

Sea Research and Oceanographic Abstracts, volume 17, pages 721–735. Elsevier.

Wiseman, W., Rabalais, N., Turner, R., Dinnel, S., and MacNaughton, A. (1997). Seasonal and interannual variability within the Louisiana coastal current: stratification and hypoxia. *Journal of Marine Systems*, 12(1):237–248.

Yu, L., Fennel, K., and Laurent, A. (2015a). A modeling study of physical controls on hypoxia generation in the northern Gulf of Mexico. *Journal of Geophysical Research: Oceans*, 120(7):5019–5039.

Yu, L., Fennel, K., Laurent, A., Murrell, M. C., and Lehrter, J. C. (2015b). Numerical analysis of the primary processes controlling oxygen dynamics on the Louisiana shelf. *Biogeosciences*, 12(7):2063–2076.

Zhang, H., Ludsin, S. A., Adamack, A. T., Brandt, S. B., Zhang, X., Kimmel, D. G., Roman, M. R., and Boicourt, W. C. (2009). Hypoxia-driven changes in the behavior and spatial distribution of pelagic fish and mesozooplankton in the northern Gulf of Mexico. *Journal of Experimental Marine Biology and Ecology*, 381:S80–S91.

Zhang, J., Gilbert, D., Gooday, A. J., Levin, L. A., Naqvi, S. W., Middelburg, J. J., Scranton, M., Ekau, W., Peña, A., Dewitte, B., Oguz, T., Monteiro, P. M. S., Urban, E., Rabalais, N. N., Ittekkot, V., Kemp, W. M., Ulloa, O., Elmgren, R., Escobar-Briones, E., and Van Der Plas, A. K. (2010). Natural and human-induced hypoxia and consequences for coastal areas: Synthesis and future development. *Biogeosciences*, 7(5):1443–1467.

Zhang, W. and Hetland, R. D. (2018). A study of baroclinic instability induced convergence near the bottom using water age simulations. *Journal of Geophysical Research: Oceans*, 123(3):1962–1977.

Zhang, W., Hetland, R. D., DiMarco, S. F., and Fennel, K. (2015). Processes controlling mid-water column oxygen minima over the Texas-Louisiana shelf. *Journal of Geophysical Research: Oceans*, 120(4):2800–2812.

Zhang, Z., Hetland, R., and Zhang, X. (2014). Wind-modulated buoyancy circulation over the Texas-Louisiana shelf. *Journal of Geophysical Research: Oceans*, 119(9):5705–5723.

Zhang, Z. and Hetland, R. D. (2012). A numerical study on convergence of alongshore flows over the Texas-Louisiana shelf. *Journal of Geophysical Research*, 117(C11):C11010.